Light-guided actin polymerization drives directed motility in protocells

Hideaki T. Matsubayashi[1,2,3†], Shiva Razavi[1,2,4,5], T. Willow Rock[1,2], Daichi Nakajima[6], Hideki Nakamura[1,2,7,8], Daniel A. Kramer[9], Tomoaki Matsuura[10], Baoyu Chen[9], Satoshi Murata[6], Shin-ichiro M. Nomura[6], Takanari Inoue[1,2†]

1 Department of Cell Biology, School of Medicine, Johns Hopkins University, 2 Center for Cell Dynamics, Institute of Basic Biomedical Sciences, Johns Hopkins University, 3 Frontier Research Institute for Interdisciplinary Sciences, Tohoku University, 4 Department of Biomedical Engineering, School of Medicine, Johns Hopkins University, 5 Department of Biological Engineering, School of Engineering, Massachusetts Institute of Technology, 6 Department of Robotics, Graduate School of Engineering, Tohoku University, 7 Hakubi Center for Advanced Research, Kyoto University, 8 Department of Synthetic Chemistry and Biological Chemistry, School of Engineering, Kyoto University, 9 Roy J. Carver Department of Biochemistry, Biophysics and Molecular Biology, Iowa State University, 10 Earth-Life Science Institute, Institute of Science Tokyo

†Corresponding authors. Email: hideaki.matsubayashi.e1@tohoku.ac.jp, jctinoue@jhmi.edu

Abstract

Motility is a hallmark of life's dynamic processes, enabling cells to actively chase prey, repair wounds, and shape organs. Recreating these intricate behaviors using well-defined molecules remains a major challenge at the intersection of biology, physics, and molecular engineering. Although the polymerization force of the actin cytoskeleton is characterized as a primary driver of cell motility, recapitulating this process in protocellular systems has proven elusive. The difficulty lies in the daunting task of distilling key components from motile cells and integrating them into model membranes in a physiologically relevant manner. To address this, we developed a method to optically control actin polymerization with high spatiotemporal precision within cell-mimetic lipid vesicles known as giant unilamellar vesicles (GUVs). Within these active protocells, the reorganization of actin networks triggered outward membrane extensions as well as the unidirectional movement of GUVs at speeds of up to 0.43 µm/min, comparable to typical adherent mammalian cells. Notably, our findings reveal a synergistic interplay between branched and linear actin forms in promoting membrane protrusions, highlighting the cooperative nature of these cytoskeletal elements. This approach offers a powerful platform for unraveling the intricacies of cell migration, designing synthetic cells with active morphodynamics, and advancing bioengineering applications, such as self-propelled delivery systems and autonomous tissue-like materials.

Introduction

Motility is a fundamental property of cells across biological systems, from bacteria to large animals (*1–6*). By transcending the randomness and viscosity of the microscopic world, cells move toward their destination by extending membrane protrusions and by clutching onto the extracellular environment. These processes are universally galvanized by actin polymerization (*7–12*). While hundreds of biomolecules are identified to be required for cell motility (*4*, *6*, *13*), a minimal list of biomolecular components sufficient for cell motility remains elusive. This is primarily due to the self-evident challenge of eliminating all biomolecules but those minimal ones in the context of living cells.

Cell migration is driven by the coordination of forward movement, rear contraction, and adhesion/deadhesion of the cell edges (*4*, *6*, *14–16*). Among these processes, actin polymerization at the leading edge is a strong candidate for driving overall forward displacement. For instance, *Dictyostelium*, fish keratocyte, and human neutrophil retain their motility even after myosin contractility is compromised genetically (*17*, *18*) or pharmacologically (*19*, *20*). Cells also manage to migrate even without strong adhesions especially in confined conditions (*21*, *22*). Conversely, we and others have shown that synthetic activation of the Rho family GTPase Rac1, an upstream activator of the actin cytoskeleton, induces directional cell movements toward the site of stimulation (*23*, *24*). However, it is still unclear if Rac1-mediated actin polymerization alone is sufficient for cell motility in cellular settings, as Rac1 crosstalks to other Rho small GTPases such as RhoA and triggers other cytoskeletal activities including acto-myosin contraction (*25*).

In a different context, molecules necessary for force generation by actin polymerization have been identified based on the motility reconstitution assay (*26–35*). These reports demonstrated that a mixture of purified cytoskeletal proteins, such as actin, Arp2/3, profilin, cofilin, and capping protein, can reconstitute the motility of *Listeria monocytogenes* bacteria using microspheres coated with actin nucleation-promoting factors (NPFs). Furthermore, a number of studies were conducted to reconstitute actin (*36*, *37*) and other cytoskeletons (*38–40*) inside cell-sized membrane-bound liposomes. These studies demonstrated that the polymerization force of actin induces membrane deformations (*41–44*), reveals the roles of actin-binding proteins (*45–51*), and explores the regulation of internal reactions by light and external environmental factors (*51–54*). However, unidirectional motion by the cytoskeletal polymerization force has not been achieved. Moreover, non-invasive and non-constitutive—hence physiological—induction of actin polymerization has yet to be achieved, particularly within cell-sized compartments with proper membrane configuration. Collectively, we decided to develop a minimal membrane-bound system where actin molecules can be locally polymerized and to test if such an artificial cytoskeletal activity could induce cell-like motility.

Results

Reversible and asymmetric light control of protein localization inside GUVs

To achieve *in vitro* reconstitution of cell motility, we previously developed active protocells where chemically inducible dimerization (CID) tools were used to polymerize actin based on a bacterial NPF inside giant unilamellar vesicles (GUVs) (*55*). While the previous system efficiently produced actin polymerization, outward membrane extension necessary for driving movement was not observed. We reasoned that this was due to a lack of fast turnover of NPF recruitment to the membranes. To aim for a physiologically relevant generation of protrusive force exerted against membranes, we adopted a light-inducible protein dimerization tool for controlling the localization of proteins of interest. Among optogenetic dimerization tools (*56*–*58*), we chose iLID-SspB (*59*) due to its favorable characteristics, including molecular size, binding kinetics, and optical requirement, which are well-suited for experimental operations without compromising physiological relevance. More specifically, the second-timescale iLID photo-reaction is ideal for recapitulating the dynamic nature of migratory cells and their front-to-back polarization (Supplementary Text).

We first set out to test light-induced dimerization of purified iLID and SspB in GUVs. In our construct, iLID was membrane-tethered, and blue light exposure triggered the Jα helix to extend, revealing the binding site for SspB. In the dark, iLID returned to its closed state, releasing SspB (Fig. 1A). We monitored SspB localization changes and visualized the light response by fusing iLID with YFP and SspB with mCherry (Fig. S1A). To anchor iLID to the GUV membrane, we tested four different protein-lipid interaction strategies to mediate light-induced translocation, including coordination bonding, electrostatic, strong non-covalent, and covalent interactions (Fig. 1A) (*60*, *61*). These strategies were implemented using 6×His-tag/Ni-NTA-conjugated lipids, myristoylated alanine-rich C-kinase substrate-effector domain (MARCKS-ED)/phosphatidylserine (PS), 2×Strep-tag/StrepTactin/biotin-conjugated lipids, and SNAP-tag/benzylguanine (BG)-conjugated lipid, respectively (Fig. S2). While all four strategies successfully localized iLID-YFP to the membrane, MARCKS-ED/PS was less efficient in membrane-anchoring, and the His-tag/Ni-NTA and Strep-tag/StrepTactin/biotin systems showed some non-specific membrane binding of SspB before light illumination (Fig. S2). Thus, we primarily used SNAP/BG for most of the following experiments.

When GUVs were made with 2% BG-conjugated lipid in the inner leaflet, iLID localized on the membrane, while SspB remained in the lumen in the dark (Fig. 1B). Upon blue light illumination of the entire GUV, SspB translocated to the membrane within 4 seconds (Fig. 1B, C). After

112 switching back to the dark, SspB gradually dissociated from the membrane with a half-time of
113 61.2 ± 13.7 seconds. The time scale is consistent with AsLOV2 based-optogenetic tools
114 measured in cells (*57*). These data confirmed that iLID-SspB enables reversible control of
115 protein localization in GUVs.
116
117 Next, we tested the potential for spatially asymmetric control of iLID-SspB interactions. When
118 light was applied locally to one side of the GUV, SspB accumulated at the illuminated site (Fig.
119 1D, E). In the dark, dissociation proceeded with a half-time of 41.8 ± 7.1 seconds (Fig S3A).
120 Despite faster diffusion on artificial lipid membranes compared to cell membranes (*62–64*),
121 localized light stimulus created an asymmetric pattern of SspB in cell-sized vesicles (Fig. 1E, F,
122 see supplementary text). Furthermore, SspB precisely and repeatedly responded to the
123 directional change of blue light illumination (Figs. 1G, S3B, C, and Movie S1). Collectively, these
124 results demonstrated that the iLID-SspB system can direct polarized protein distribution at
125 regions of interest on the GUV membranes.
126
127 **Light-guided control of ActA**
128 Next, we sought to manipulate the actin cytoskeleton with the iLID-SspB system. Previous
129 studies have established that the rate of actin polymerization depends on the surface density of
130 NPFs (*26*, *30*, *35*) and that clustering of NPFs accelerates actin polymerization (*65*, *66*). We have
131 recently shown that chemically-induced membrane recruitment of ActA, an N-WASP homolog
132 NPF derived from *L. monocytogenes*, induces actin polymerization on the membrane of GUVs,
133 leading to symmetry breaking (*55*). Thus, we first tested ActA with the iLID-SspB system. By
134 testing two SspB variants with different affinities (SspB micro and SspB nano) and two fusion
135 orders (resulting in four ActA-SspB variants in total), we found that ActA-SspB$_{nano}$-mCherry
136 activates Arp2/3-dependent actin polymerization in bulk pyrene actin assays (Fig. S1, S4A, B)
137 and exhibits the best light-dependent membrane translocation without non-specific membrane
138 binding in the dark (Fig. S4C, D). When supplemented with actin and Arp2/3, light-induced
139 global membrane recruitment of ActA-SspB led to the emergence of actin patches on the
140 membrane, consistent with our previous findings with a chemical input (*55*) (Fig. S5). With local
141 light, ActA distribution became asymmetric, yet the directionality of actin polymerization could
142 not be maintained. In most cases, polymerized actin was randomly diffused out from the
143 illuminated region and the GUV lost actin directionality over time (Fig. S6 and Movie S2).
144
145 **Reversible control of pVCA and light-guided actin polymerization**
146 For robust maintenance of actin asymmetry, we set out to rapidly depolymerize actin filaments
147 in the non-illuminated area, providing precursor G-actin for new polymerization events. We
148 thus incorporated factors that facilitate the actin turnover process, namely profilin, cofilin, and
149 capping protein. Moreover, ActA could not induce membrane actin polymerization in GUVs in

150 the presence of cofilin and capping proteins (Fig. S7). We evaluated common NPFs to identify a
151 more potent alternative to ActA. Among those tested, GST-tagged N-WASP pVCA (proline-rich
152 region + VCA domain) showed the fastest actin polymerization in a bulk pyrene assay, which
153 monitors actin polymerization through the florescence increase of pyrene-labeled actin.
154 Notably, GST-pVCA maintained its activity when fused to SspB-mCherry fusion (Fig. 2A, S1, S8).
155
156 We then encapsulated this light-inducible pVCA-SspB-mCherry with actin (10% Alexa-647
157 labeled), Arp2/3, profilin, cofilin, and capping protein in GUVs (Fig. 2B). Upon illumination,
158 pVCA-SspB-mCherry rapidly translocated to the membrane, followed by the increase of
159 membrane actin signal, suggesting light-induced actin polymerization (Fig. 2C–E, Movie S3). In
160 contrast, in the absence of either pVCA or light stimuli, no significant change in membrane actin
161 intensity was observed (Fig. 2D, E, Fig. S9). When Arp2/3 was omitted, the membrane actin
162 signal showed a slight increase over time. This suggested that the G-actin binding property of
163 pVCA (*67*, *68*) increased local concentration of the G-actin at the periphery of membrane and
164 facilitated spontaneous polymerization, which was not as intense as Arp2/3-dependent actin
165 polymerization (Fig. 2D, E, Fig. S9). Taken together, these data suggested that light-dependent
166 membrane accumulation of pVCA induces Arp2/3-dependent actin polymerization on the GUV
167 membrane.
168
169 Next, we tested the reversibility of the actin polymerization. As shown in Fig. 2F and G, both
170 pVCA-SspB-mCherry and actin reversibly and repetitively changed their intensity on the
171 membrane depending on blue light switching (Movie S4). Notably, once switched to the dark,
172 pVCA-SspB-mCherry quickly dissociated from the membrane, whereas actin decreased its
173 membrane intensity at a relatively slower rate (Fig. S10). This delay in actin response suggested
174 that actin was not simply sequestered by pVCA dissociation, but was rather gradually
175 depolymerizing. Furthermore, when the system responded to the next round of blue light
176 illumination, actin signal increased slightly slower than pVCA-SspB, supporting that a substantial
177 fraction of actin filaments disassembled in the dark and re-polymerized upon new stimulus (Fig.
178 S10). Together, these results suggested that the polymerization state is reversible in our system
179 and that the balance between polymerization and depolymerization can be controlled by light.
180
181 **Asymmetric and spatially controlled actin polymerization**
182 The polarity of NPFs and actin polymerization are fundamental features of directed cell
183 migration (*9*, *69*, *70*). Thus, we next tested whether locally targeted pVCA could establish
184 asymmetric actin polymerization (Fig. 3A). As shown in Fig. 3B, C, and Fig. S11A, pVCA showed
185 asymmetric patterning toward the localized light stimulus (Movie S5). About 5 minutes after
186 pVCA translocation, the actin signal also increased from the illuminated region and created an
187 asymmetric pattern. Furthermore, with continuously applied local light, both pVCA and actin

188 maintained their polarity for more than 100 minutes (Fig. 3B, C, S11A, Movie S5). We note that
189 the actin signal appeared as two lines in the latter time points in the kymograph. This is possibly
190 because actin filaments are less diffusive on the membrane, and so Alexa-647 labeled on actin
191 molecules was gradually photo-bleached by blue light excitation. Next, we tested if the system
192 reversibly changed the direction of actin polymerization. After establishing an asymmetric actin
193 pattern with a local light on the right side of the vesicle, we reversed it back to the dark mode
194 and subsequently shed new light on the left. pVCA and actin responded accordingly to re-
195 polarize toward the new signal site (Fig. 3D, E, and Movie S6). These data demonstrated that
196 the light-inducible pVCA system can establish polarized actin patterns in a reversible manner.
197
198
199 Importantly, when locally illuminated, the front membrane of some GUVs moved toward the
200 light direction (Fig. S11B), albeit occasionally (2 out of 7 instances). We speculate that
201 characteristics inherent to the GUV system such as surface-to-volume ratio of individual GUVs,
202 surface density of pVCA, and the ratio between Arp2/3 and capping protein (*33*, *71*), as well as
203 any combination of these factors might be critical in determining a functional output.
204
205 **mDia1-driven actin polymerization drives efficient membrane protrusions in cells**
206 To enhance forward membrane protrusion, we next sought to reinforce actin polymerization.
207 At the leading edge of migrating cells, two major actin nucleators, namely Arp2/3 and formin,
208 coordinate the forward extension of the plasma membrane (*72*–*74*). While Arp2/3 stays at the
209 branch points of the actin filaments and does not engage in the incorporation of monomeric
210 actin into the growing ends, formin continuously binds to the growing ends and actively recruits
211 profilin-actin complexes to the elongating tips. Consequently, one subtype of formin, mDia1,
212 accelerates actin polymerization 4–5 times faster (*75*, *76*) and drives motility 6–23 times faster
213 than Arp2/3 in *in vitro* motility assays using functionalized beads (*30*, *28*, *31*). Furthermore, a
214 theoretical study suggests that actin polymerization perpendicular to the membrane,
215 characteristic of formin-driven filopodia formation, more efficiently transduces the
216 polymerization force to advance the membrane (*77*). Therefore, we reasoned that the
217 integration of mDia1 could enhance protrusive activity.
218
219 In line with our previous actin-actuation tool development (*78*), first, we used living cells to test
220 if membrane recruitment of mDia1 could induce actin polymerization and membrane
221 protrusions in a three-dimensional lipid bounded context (Fig. S12A) (*79*–*81*). More specifically,
222 we took FH1-FH2-DAD domains from mDia1 as a constitutively active form (*82*) and recruited it
223 to the plasma membrane by the CID system. As shown in Fig. S12B–H, rapamycin-dependent
224 plasma membrane translocation of YF-mDia1 induced filopodia-like protrusions (Fig. S12B–H).
225 These protrusions were positive for Lifeact signal and showed coiling motions with their

226 elongating tips labeled with YF-mDia1 (Fig. S12D), replicating the previously reported
227 phenotypes of formin-dependent filopodia elongation (*83–86*). These data supported that
228 membrane translocation of mDia1 generates an actin-dependent protrusive force on the
229 membrane.
230
231 **mDia1-driven actin polymerization drives forward movement of GUVs**
232 We then constructed the light-inducible version of mDia1 (mCherry-SspB-mDia1) (Fig. S1, S8)
233 and encapsulated it with iLID-YFP-SNAP, actin (10% Alexa-647 labeled), profilin, and cofilin in
234 GUVs. Upon local recruitment of mDia1, some vesicles showed gradual drift toward the
235 stimulated direction, suggesting that mDia1 exerted protrusive forces also in the reconstituted
236 lipid vesicles (Fig. S13A, B). However, the response was minimal and difficult to detect.
237 Therefore, aiming to better mimic the actin network of migrating cells, we added pVCA-SspB,
238 Arp2/3, and capping protein (Fig. 4A). Remarkably, this full component system (pVCA + mDia1)
239 showed robust movements toward light stimulation, as observed in 18 out of 22 GUVs (Fig. 4B–
240 D, Fig. S13C–E, Movie S7, S9, S10). Polarized actin signal toward the illuminated direction
241 suggested that actin polymerization provided the force to push the membrane forward (Fig. 4B,
242 Movie S7). The vesicle continued to move steadily for an hour until the light was turned off (Fig.
243 4B, D, Movie S7). Furthermore, when we shifted the position of the blue light, the signals for
244 mDia1, pVCA, and actin reoriented, causing the vesicle to move in the new direction, akin to
245 how a migrating neutrophil responds to a new chemoattractant (Fig. 4B, D, Movie S7). The
246 speed of pVCA/mDia1 dual system was roughly 3 times larger than that of mDia1 GUVs (Fig. 4F,
247 S13B–D). The distance the front side membrane moved in 30 minutes was also significantly
248 longer in pVCA + mDia1 GUVs (Fig. S13E). Furthermore, membrane recruitment of mDia1 and
249 pVCA occasionally showed local protrusions, suggesting the generation of protrusive force (Fig.
250 S14, Movie S8). Together, the data indicated that mDia1-driven actin polymerization exhibits a
251 protrusive force that is substantially enhanced by pVCA and Arp2/3.
252
253 When mDia1 and pVCA were replaced with the same amount of mCherry-SspB, vesicles did not
254 move even with the local blue light illumination (Fig. S15). In addition, the kymographs of the
255 protrusions of the vesicle perimeter and the membrane actin intensity indicated the timing and
256 direction of membrane protrusions correlate to the actin intensity and its polarity, supporting
257 that membrane protrusion is driven by actin cytoskeleton (Fig. 4D, E). Corroborating this, the
258 actin sequestering compound Latrunculin A and the formin inhibitor SMIFH2 substantially
259 compromised motility (Fig. 4H). Furthermore, deletion of the DAD domain from mDia1, which is
260 responsible for efficient actin nucleation by mDia1 (*87*), abolished the motility (Fig. 4H). These
261 results indicate that membrane protrusion and motion of the vesicles are driven by actin
262 polymerization.
263

264 **Deformation and adhesion of GUVs**

265 Although the vesicles initially moved at an average velocity of 0.43 μm/min, their speed
266 gradually decreased over time (Fig. 4F, G, Fig. S13C, D). Concomitant with this deceleration, the
267 contact area of the bottom side of the vesicles constantly increased during the movement,
268 stabilizing the vesicles in a dome-like shape (Fig. 4C, I). This increase in the contact area was not
269 seen in the GUVs when pVCA and mDia1 were replaced with mCherry-SspB (Fig. S15). Thus, we
270 speculate that the contact to the bottom substrate was induced by the protrusive reaction and
271 that the adhesion and the concomitant deformation led to cumulative tension increase (*88*)
272 which in turn counteracted the protrusive force. The force exerted by actin polymerization may
273 not be enough to detach the GUV from the BSA-coated glass substrate. This is consistent with
274 the observation where an initial contact site remained adherent even in a GUV that traveled
275 farthest (Fig. 4I, Fig. S16A, B, Movie S9, S10). Additionally, actin recycling in the system may be
276 insufficient and force gradually diminishes over time (*89*). Despite these potential resisting
277 factors, the combination of mDia1 and pVCA induced movement consistently (Fig. 4, Fig. S13C,
278 S16). Thus, we concluded that the asymmetric actin polymerization mediated by pVCA-mDia1 is
279 sufficient to propel the vesicles forward from within.

280

281 # Discussion

282 In the present study, we developed a fully reconstituted protocellular system to achieve light-
283 directed motility in a protocell. We leveraged mDia1-mediated actin polymerization to establish
284 the forces that drive movement. Our findings not only corroborate recent cell biological
285 findings on formin's significant roles in cell migration (*83*, *90*–*95*) but also uniquely demonstrate
286 that the mDia1-mediated actin polymerization system is sufficient to propel lipid vesicles,
287 overcoming challenges thus far posed by genetic redundancy and cellular complexity. Formin-
288 mediated actin polymerization exhibits several unique features compared to free barbed end
289 elongation in Arp2/3-dependent polymerization, including processive elongation (*31*, *75*),
290 accelerated polymerization rate (*75*, *76*), rotation, and coiling motion (*85*, *86*, *96*). These
291 characteristics could contribute to the effective propulsion of the vesicle. Remarkably, our
292 minimal system further revealed a significant synergy between pVCA and mDia1. Although
293 further investigation is required, this synergistic effect may be explained by a positive feedback
294 loop: mDia1 functions both as an actin elongator and a supplier of mother filaments for Arp2/3-
295 mediated actin polymerization (*91*, *93*). In return, branch formation by the Arp2/3 complex
296 likely generates more growing filaments for mDia1 to bind and elongate. To further elucidate
297 the mechanisms of force generation and membrane protrusion, unveiling the nanoscopic
298 architecture of the actin network in the migrating protocell will be crucial. Our protocell
299 approach, which bridges the gap between cellular and biochemical domains, opens new
300 avenues for comprehensively interrogating modules of cellular motility.

301
302 We achieved a GUV displacement speed in the range of 0.1–1.0 µm/min, which is comparable
303 to the migration rates of typical fibroblasts (*97*) and other adherent cells including those that
304 competed in the World Cell Race (*98*). How could we make the movement even faster? *L.*
305 *monogytogenes* and NPF-coated beads in purified cytoskeletal protein solution typically move
306 in the range of 1–15 µm/min (*27*, *28*, *30–33*). Some adherent cells can migrate at 5 µm/min
307 even when actomyosin contractility is inhibited (*19*). We propose three possible ways to make
308 artificial cell migration faster. First, increasing actin concentration (*76*, *99*) and integrating
309 additional factors, such as VASP (*100*), Fascin (*101*), and NPFs (*66*, *102*), could accelerate the
310 rate of actin polymerization. Secondly, optimizing membrane tension could enhance the
311 deformability of the lipid membrane, akin to the malleable structures observed in motile cells,
312 thereby potentially promoting more efficient protrusion and motility (*49*, *103*). Finally, fine-
313 tuning adhesion could enhance migration efficiency as many cells exhibit a preference for an
314 optimal adhesion range, where both insufficient and excessive adhesion can hinder motility
315 (*104*, *105*).
316
317 Interestingly, the phenotypes of mDia1 membrane recruitment differed between cells and
318 GUVs. In cells, mDia1 produced filopodia-like thin protrusions (Fig. S12), whereas in GUVs, it
319 pushed the lipid membrane as a continuous plane at a much broader scale than filopodia (Fig. 4,
320 S13–16). Since living cells tend to have higher membrane tension than liposomes (*106*), it may
321 appear counterintuitive that the cell membrane was more susceptible to mDia1-induced local
322 deformation. One possible explanation is that, in cells, endogenous proteins might work in
323 concert with mDia1 to amplify local membrane deformation and form long filopodia-like
324 protrusion. For Instance, SH3-containing proteins including IRSp53 (*107*) and Abi1 (*91*) could
325 interact with the proline-rich FH1 domain of mDia1. Alternatively, localized defects in
326 membrane tension could predispose certain areas to form thin protrusions (*108*). Additionally,
327 cytoskeleton-bound transmembrane proteins impede tension propagation in cells (*109*).
328 Furthermore, the nuclear accumulation of mDia1 in cells (Fig. S12) could reduce its effective
329 concentration and cause a heterogeneous distribution on the cell membrane, resulting in
330 focused protrusive force in regions with high mDia1 concentration, similar to how pVCA-driven
331 finger-like protrusions are formed in liposomes, as demonstrated by Gat *et al.* (*110*). Seamlessly
332 bridging native and artificial cells would be critical for a comprehensive understanding of the
333 regulatory mechanism of cellular morphodynamics.
334
335 We have recently shown that chemically-induced membrane recruitment of ActA, an NPF
336 derived from *L. monocytogenes*, and subsequent global actin polymerization lead to
337 eccentricity in the shape of GUVs (*55*). We noted a difference in membrane deformation
338 between the CID and LID systems, as the CID too could induce a clear membrane deformation

339 given a global, non-directional input. This difference could be attributed to the variations in
340 cytoskeletal proteins and input signals between the two systems. In the present study, we have
341 incorporated cofilin and capping proteins. Since cofilin and capping protein accelerate actin
342 depolymerization, these factors may make the actin network more plastic rather than exert
343 force to deform the membrane. Moreover, the binding kinetics of iLID-SspB (k_{on} =1.2 × 10^3 $M^{-1}s^{-}$
344 ^{1}, k_{off} =1.1 × 10^{-3} s^{-1}, K_d = 0.8 μM) substantially differs from that of FKBP-FRB (k_{on} =1.9 × 10^6 $M^{-1}s^{-}$
345 ^{1}, k_{off} =2.2 × 10^{-2} s^{-1}, K_d = 12 nM) (*59*, *111*, *112*). This may result in different reaction dynamics
346 between actin cytoskeleton and the lipid membrane.
347
348 Our finding that internal cytoskeletal force can drive the unidirectional motion of lipid vesicles
349 would offer avenues to reverse-engineer cell motility. Although we used light as an input,
350 asymmetric actin polymerization may be achievable with chemical inputs with consideration of
351 binding affinity (*79*, *113*), transmembrane signal transduction mechanisms (*114*), and self-
352 organized pattern formation (*115*–*119*). Furthermore, combining this approach with other
353 migratory forces (*111*, *120*, *121*) and applying synthetically engineered cytoskeletal molecules
354 (*76*, *122*) could enhance the motility even beyond the limit of natural systems. Achieving
355 synthetic motility in GUVs could be a step toward future developments in active therapeutic
356 agents, self-organizing artificial tissues, and synthetic neural circuits.

Materials and Methods

Reagents

ATP was purchased from Gold Biology (A-081) or Nacalai Tesque (01072-82), prepared as 100 mM solution in 100 mM Tris-HCl (pH 7.4 at RT), and stored at -20°C. Creatin phosphate was purchased from Gold Biotechnology (C-323-5) or Oriental Yeast (45180000), prepared as 1 M solution in PBS (Gibco 10010-023), stored at -20°C. Creatin kinase was purchased from Sigma-Aldrich (10127566001) or Oriental Yeast (46430003), prepared as 40 µM solution in buffer V (50 mM HEPES-NaOH (pH 7.5), 150 mM NaCl, 7 mM β-mercaptoethanol, 10% glycerol), snap frozen, and stored at -20°C. Flavin mononucleotide (FMN) was purchased from TCI (R0023) and Wako (06500171), freshly prepared as 600 µM solution in MilliQ water before iLID expression. Alexa Fluor 647 C2 Maleimide (A20347) and Pierce™ Glutathione Agarose (16100) were purchased from Thermo Fisher Scientific. Hexadecane (H6703), Silicone oil (378348), and SMIFH2 (S4826) were purchased from Sigma-Aldrich. Latrunculin A was purchased form Wako (125-04363). Benzylguanine-PEG2000-DSPE was prepared and purified as previously described (*60*). POPC (1-palmitoyl-2-oleoyl-glycero-3-phosphocholine, 850457), POPS (1-palmitoyl-2-oleoyl-sn-glycero-3-phospho-L-serine, 840034), 18:1 DGS-NTA-Ni (1,2-dioleoyl-sn-glycero-3-[(N-(5-amino-1-carboxypentyl)iminodiacetic acid)succinyl] (nickel salt), 790404), 18:1 PE-PEG2000-benzylguanine (1,2-dioleoyl-sn-glycero-3-phosphoethanolamine-N-[benzylguanine(polyethylene glycol)-2000], 880137), and 18:1 Biotinyl Cap PE (1,2-dioleoyl-sn-glycero-3-phosphoethanolamine-N-(cap biotinyl) (sodium salt), 870273C) were purchased from Avanti Polar Lipids as chloroform solution. Actin (AKL99), pyrene labeled actin (AP05), Arp2/3 (RP01P), Profilin (PR02), Cofilin (CF01), were purchased from Cytoskeleton. Strep-Tactin XT (2-4010-010, discontinued) resin, Strep-Tactin XT 4Flow (2-5010-010) resin, and purified Strep-Tactin protein were purchased from IBA. Ni-NTA agarose (30210) was purchased from Qiagen. Amylose resin (E8021S) was purchased from New England BioLabs.

Plasmid construction

pQE80L-6×His-MBP-TEVprorease(S219V)

Ser219Val mutation (*123*) was introduced by PCR with the template plasmid gifted from Dr. Yubin Zhou and the primer set of fwd: 5’-TGGTGAAACCTGAAGAACCTTTT-3’ and rev: 5’-TTCACCATGAAAACTTTATGGCC-3’. TEV prorease (S219V) was then PCR amplified with the primer set of fwd: 5’-AATTGAGCTCGATGAGCGGCCTGGTGC-3’ and rev: 5’-AATTGGATCCTTATTGCGAGTACACCAATTCATTCATG-3’ and inserted between SalI and BamHI sites of pQE-80L MBP-SspB Nano plasmid (Addgene #60409) by using restriction digestion and T4 ligase ligation process.

394 pQE80L-6×His-MBP-TEVsite-mCherry-SspB(micro)
395 EYFP-2×SAGG linker was PCR amplified from the template plasmid YFP-FKBP (*124*)with the
396 primer set fwd: 5'- GTATTTTCAGGGATCGCCGCTAGCGCTACCGG-3' and rev: 5'-
397 TCGGGGAGCTGGATCCTCCGCCAGCGCTGC-3' and inserted into BamHI site of pQE-80L MBP-SspB
398 Nano plasmid (Addgene #60409) by using Gibson assembly. EYFP part was then replaced with
399 mCherry from pmCherry-C1 (Clontech) by restriction digestion and T4 ligase ligation process
400 with AgeI and BsrGI. Arg73 of SspB was mutated to Gln by PCR with the primer set fwd: 5'-
401 AACGCCCagTTTAAGGGCGTGTCTCGT-3' and rev: 5'- CTTAAActGGGCGTTGAACTGGATAA-3'.
402
403 pGEX-2T-GST-3Csite-TEVsite-6×His
404 Two sets of oligo DNA pairs were designed to introduce 3C protease cleavage site, TEV protease
405 cleavage site, and 6×His tag (1st set, fwd: 5'-
406 GGTTCCGCGTGGATCTGGTCTTGAGGTGCTCTTTCAGGGACCCGGCAGTCTCGAGGGTCTGTACAAGCG
407 AATTCAG-3', rev: 5'-
408 CTGAATTCGCTTGTACAGACCCTCGAGACTGCCGGGTCCCTGAAAGAGCACCTCAAGACCAGATCCACG
409 CGGAACC-3'. 2nd set, fwd: 5'-
410 TACAAGCGAATTCAGGAGAACCTCTACTTTCAAAGCGATCATCATCATCATCATCACTAAAAATTCATCGT
411 GACTG-3' and rev: 5'-
412 CAGTCACGATGAATTTTTAGTGATGATGATGATGATGATCGCTTTGAAAGTAGAGGTTCTCCTGAATTCG
413 CTTGTA-3' (underlines indicate overhang sequences)). To anneal oligo DNAs individually, 0.5
414 µM each DNAs were mixed in 1× T4 Ligase buffer (NEB, B0202S) and heated at 85°C for 10 min
415 and cooled 5°C per 2 min down to 40°C. pGEX-2T, which was kindly gifted from Dr. Miho Iijima,
416 was digested by BamHI and EcoRI and assembled with the two annealed DNA fragments by
417 Gibson assembly.
418
419 pGEX2T-GST-pVCA-3Csite-SspB(micro)-mCherry-TEVsite-6×His
420 To first construct pGEX2T-GST-pVCA-3Csite-TEVsite-6×His, pVCA (proline rich region and VCA
421 domain) of human N-WASP was PCR amplified with the primer set fwd: 5'-
422 CAGTCTCGAGGGAGGTGTTGAAGCTGTTAAAAATGA-3' and rev: 5'-
423 TCCTGAATTCCGTCTTCCCACTCATCATCATCCTC-3' and inserted between XhoI and EcoRI site of
424 pGEX-2T-GST-3Csite-TEVsite-6×His by using restriction digestion and T4 ligase ligation. Then,
425 SspB(micro)-mCherry was PCR amplified with the primer set fwd: 5'-
426 TGAGTGGGAAGACGGAATTGGGCAGTCGACGGTACCGCG-3' and rev: 5'-
427 GTAGAGGTTCTCCTGAATTCCCTTGTACAGCTCGTCCATGCC-3' and inserted in the EcoRI site of
428 pGEX2T-GST-pVCA-3Csite-TEVsite-6×His by Gibson assembly.
429
430 pET28-2×Strep-iLID-EYFP-MARCKS

431 First, pET28-2×Strep-iLID-6×His was constructed as follows. iLID sequence was cut out from the
432 pLL7.0: Venus-iLID-Mito (Addgene #60413) by NheI and EcoRI and inserted between NheI and
433 EcoRI sites of pET28-2×Strep-tag gifted from Dr. Kanemaki by using restriction digestion and T4
434 ligase ligation. Then, to construct pET28-2×Strep-iLID-EYFP-6×His, EYFP was PCR amplified from
435 pEYFP-C1 (Clontech) with the primer set fwd: 5'-AATTGTCGACATGGTGAGCAAGGGCGAG-3' and
436 rev: 5'-AATTGCGGCCGCCTTGTACAGCTCGTCCATGC-3' and inserted between SalI and NotI sites
437 of pET28-2×Strep-iLID-6×His by restriction digestion and T4 ligation. MARCKS-ED fragment was
438 constructed by oligo annealing (1st set fwd: 5'-
439 GTACAAGGGAAGTGCTGGTGGTAAAAAGAAAAAGAAGCGCTTTTCCTTC-3' and rev: 5'-
440 TTCTTGAAGGAAAAGCGCTTCTTTTTCTTTTTACCACCAGCACTTCCCTT-3', 2nd set fwd: 5'-
441 AAGAAGTCTTTCAAGCTGAGCGGCTTCTCCTTCAAGAAGAACAAGAAGTA-3' and rev: 5'-
442 GTACTACTTCTTGTTCTTCTTGAAGGAGAAGCCGCTCAGCTTGAAAGAC-3') and inserted into BsrG1
443 site of pET28-2×Strep-iLID-EYFP-6×His.
444
445 pET28-2×Strep-iLID-EYFP-SNAP
446 SNAP tag sequence was PCR amplified from the template Phage-ubc-nls-ha-tdMCP-SNAP, a kind
447 gift from Dr. Bin Wu, with the primer set fwd: 5'-
448 AATTTGTACAAGTCTGCTGGCGGAAGCGCTGGAGGCAGCATGGACAAAGACTGCGAAATGAAGC-3'
449 and rev: 5'-AATTGCGGCCGCTTAACCCAGCCCAGGCTTG-3' and inserted between BsrGI and NotI
450 of pET28-2×Strep-iLID-EYFP-MARCKS by restriction digestion and T4 ligation.
451
452 iLID-EYFP-CAAX (Clontech C1) and iLID mutants
453 iLID-EYFP sequence was cut out from pET28-2×Strep-iLID-EYFP-6×His by NheI and BsrGI and
454 inserted between NheI and BsrGI sites of FRB-ECFP-CAAX (*125*) by using restriction digestion
455 and T4 ligation.
456
457 mCherry-SspB(micro) (Clontech C1)
458 SspB(micro) sequence was PCR amplified from pQE80L-6×His-MBP-TEVsite-mCherry-
459 SspB(micro)
460 with the primer set fwd: 5'-GAACAGTACGAACGCGCC-3' and rev: 5'-
461 AATTCTCGAGGACCACCAGCACTACCACCAGCACTACCACCAGCACTACCACCAGCACTACCACCAGCAC
462 TACCAATATTCAGCTCGTCATAGATT-3' and inserted between BsrGI and XhoI sites by restriction
463 digestion and T4 ligation. A silent mutation was introduced to BamHI site upstream of SspB by
464 inverse PCR with the primer set fwd: 5'-GAGGATCtAGCTCCCCGAAACGCCCT-3' and rev: 5'-
465 GGGAGCTaGATCCTCCGCCAGCGCTG-3'
466
467 pQE80L-MBP-TEVsite-mCherry-MCS

468 mCherry sequence was PCR amplified from pmCherry-C1 (clontech) with the primer set fwd: 5'-
469 GTATTTTCAGGGATCGCTAGCGCTACCGGTC-3' and rev: 5'-
470 TCAGCTAATTAAGCTATCAGTTATCTAGATCCGGTGGATC-3' and inserted between BamHI and
471 HindIII sites of pQE-80L MBP-SspB Nano by Gibson assembly.
472
473 2×Strep-mCherry-MCS
474 mCherry sequence was PCR amplified from pmCherry-C1 (clontech) by the primer set fwd: 5'-
475 AGCGGGTGCCGCTAGTCATATGGGTACGCTAGCGCTACCGGTCG-3' and rev: 5'-
476 GGTGGTGGTGCTCGATCAGTTATCTAGATCCGGTGGATCC-3' and inserted between NheI and XhoI
477 sites of pET28-2×Strep-tag by Gibson assembly.
478
479 2×Strep-MBP-TEVsite-mCherry-MCS
480 MBP-TEVsite-mCherry-MCS was PCR amplified from the template pQE80L-MBP-TEVsite-
481 mCherry-MCS with the primer set fwd 5'-CAAATGGGTCGGATCGACGGATCTAAAATCGAAGAAGG-
482 3' and rev: 5'-GGTGGTGGTGCTCGATCAGTTATCTAGATCCGGTGGA-3' and inserted between
483 BamHI and XhoI sites of pET28-2×Strep-tag by Gibson assembly.
484
485 pCold-6×His-2×Strep-MBP-TEVsite-mCherry-SspB(micro)-mDia1(FH1-FH2-DAD)
486 A DNA fragment 2×Strep-MBP-TEVsite-mCherry was PCR amplified from 2xStrep-MBP-mCherry-
487 MCS with the primer set fwd: 5'-TCGAAGGTAGGCATATGGGCTGGTCTCACCC-3' and rev: 5'-
488 ACAGCTCGTCCATGCCG-3'. The other DNA fragment SspB(micro) was PCR amplified from
489 mCherry-SspB(micro) (Clontech C1) with the primer sets fwd: 5'-GCATGGACGAGCTGTACAAG-3'
490 and rev: 5'-TCATTCTTGGCCATAGCTTGAGCTCGAGGACC-3'. pCold-mDia1, which was a kind gift
491 from Dr. Roberto Dominguez, was digested by NdeI and assembled with the two DNA
492 fragments by Gibson assembly.
493
494 pET28-2×Strep-mCherry-SspB(micro)-mDia1(FH1-FH2-DAD)
495 mCherry-SspB(micro)-mDia1(FH1-FH2-DAD) was cut out from pCold-6×His-2×Strep-MBP-
496 TEVsite-mCherry-SspB(micro)-mDia1(FH1-FH2-DAD) by AgeI and BamHI and inserted between
497 AgeI and BamHI sites of 2×Strep-mCherry-MCS by restriction digestion and T4 ligation.
498
499 EYFP-FKBP-mDia1(FH1-FH2-DAD)
500 mDia1(FH1-FH2-DAD) was cut out from pCold-6×His-2×Strep-MBP-TEVsite-mCherry-
501 SspB(micro)-mDia1(FH1-FH2-DAD) by XhoI and BamHI and inserted between XhoI and BamHI of
502 EYFP-FKBP by restriction digestion and T4 ligation.
503
504 pET28-6×His-2×Strep-TEVsite-Capβ2(mouse)-Capα1(mouse)

505 First, pET28-6×His-2×Strep was constructed as follows. 6×His sequence was synthesized by oligo
506 annealing of fwd: 5'-AGGAGATATACCATGGGCCATCACCATCACCATCACATGGGCTGGTCTCA-3'
507 and rev: 5'- TGAGACCAGCCCATGTGATGGTGATGGTGATGGCCCATGGTATATCTCCT-3' and
508 inserted into NcoI site of pET28-2×Strep-tag. Capβ2(mouse)-Capα1(mouse) was PCR amplified
509 from the template of pET3d-Capβ2(mouse)-Capα1(mouse), gifted from Dr. Julie Plastino and Dr.
510 Cecile Sykes, with the primer set fwd: 5'-
511 CTGGAGCGGGTGCCGCTAGCGAGAACCTCTACTTTCAAAGCGATATGAGCGATCAGCAGCTGG-3' and
512 rev: 5'- TGTCGACGGAGCTCGAATTCTTAAGCATTCTGCATTTCTTTGCCAATC-3' and inserted
513 between NheI and EcoRI of pET28-6×His-2×Strep by Gibson assembly. TEV cleavage site was
514 designed in the forward primer and introduced between 2×Strep tag and Capβ2 ORF.
515
516 **Actin preparation**
517 Actin for GUV experiments was reconstituted from lyophilized powder as described in
518 manufacturer's instructions, aliquoted, snap-frozen in liquid nitrogen, and stored at -80°C.
519 For actin polymerization assays, actin was dissolved in G-buffer [2 mM Tris-HCl (pH 7.5 at RT),
520 0.1 mM $CaCl_2$, 0.2 mM ATP, 0.5 mM DTT, 1 mM NaN_3] at concentration less than 65 µM and
521 dialyzed against G-buffer for 3 days with daily buffer exchange. Dialyzed actin was then purified
522 by a Superdex 200 increase 10/300 GL column (Cytiva) to separate monomer fraction from
523 occasional larger molecular size (smaller elution volume) fraction. The purified actin was stored
524 at 4°C with dialysis against G-buffer. The dialysis buffer for actin storage was exchanged twice a
525 week**.**
526 Alexa 647 labeling of actin was performed following the previously reported method (*126*). First,
527 rabbit skeletal muscle actin (Cytoskeleton Inc., #AKL99) was dissolved in G*-buffer [2 mM Tris-
528 HCl (pH 7.5 at RT), 0.1 mM $CaCl_2$, 0.2 mM ATP] at concentration less than 65 µM and dialyzed
529 against G*-buffer overnight and 3 hours. Dialyzed actin was collected and mixed with 4 molar
530 excess Alexa Fluor 647 C2 maleimide (ThermoFisher, A20347, solubilized to 10 mM in DMSO)
531 and incubated at 4°C overnight with rotation (10 min labeling as in the original protocol did not
532 yield efficient labeling in the case of Alexa Fluor 647). The reaction was quenched by adding
533 DTT to 10 mM. aggregated proteins and insoluble dyes were removed by ultracentrifugation at
534 350,000×g (90,000 rpm, TLA-100.1 rotor) for 12 min. The supernatant was collected and mixed
535 1/10 volume of 10×KMEI buffer (500 mM KCl, 10 mM $MgCl_2$, 10 mM EGTA, 100 mM Imidazole,
536 pH 7.0) and final 1 mM ATP to polymerize actin at RT for 2–3 hours. Labeled filamentous actin
537 was collected by ultracentrifugation at 195,000×g (67,000 rpm, TLA-100.1 rotor) for 30 min and
538 resuspended with G-buffer. The labeled actin was dialyzed against G-buffer for 3 days with daily
539 buffer exchange and purified through size exclusion chromatography with a Superdex 200
540 increase 10/300. The protein was snap-frozen in liquid nitrogen and stored at -80°C.
541
542 **Protein purification**

543 All protein expressions were carried out in BL21-CodonPlus (DE3)-RIL (Agilent Technologies).
544 Cell lysis was performed by microfluidizer (Microfluidics, Model M-110Y).
545
546 6×His-MBP-TEV protease (S219V)
547 The bacteria transformed with pQE80L-6×His-MBP-TEVprotease (S219V) were cultured
548 overnight in LB broth supplemented with 100 µg/mL Ampicillin and 25 µg/mL Chloramphenicol
549 (LB/Amp/Cam). Pre-culture was inoculated to LB/Amp/Cam and cultured at 37°C until OD_{600}
550 reached around 0.4. Protein expression was induced by adding 300 µM IPTG and allowed to
551 proceed for 17 hours at 18°C. The cells were re-suspended with 50 mM Tris-HCl (pH 7.5 at RT),
552 250 mM NaCl, 5 mM $MgCl_2$, 7 mM β-mercaptoethanol and lysed by microfluidizer. The lysate
553 was centrifuged at 20,000×g at 4°C for 30 min to remove cell debris. The protein was purified
554 by Ni-NTA, eluted around 60–100 mM imidazole, and then dialyzed against 25 mM Tris-HCl (pH
555 7.5 at RT), 200 mM NaCl, 7 mM β-mercaptoethanol. The elution was concentrated by Amicon
556 Ultra (10 kDa cutoff) and further dialyzed against 25 mM Tris-HCl (pH 7.5 at RT), 200 mM NaCl,
557 7 mM β-mercaptoethanol, 50% glycerol. The protein was stored at -20 °C.
558
559 mCherry-SspB
560 The bacteria transformed with pQE80L-6×His-MBP-TEVsite-mCherry-SspB were cultured
561 overnight in LB broth supplemented with 100 µg/mL Ampicillin and 25 µg/mL Chloramphenicol
562 (LB/Amp/Cam). Pre-culture was inoculated to LB/Amp/Cam and cultured at 37°C until OD_{600}
563 reached 0.4–0.6. Protein expression was induced by adding 300 µM IPTG and allowed to
564 proceed for 18 hours at 22°C. The cells were re-suspended with 50 mM Tris-HCl (pH 7.5 at RT),
565 250 mM NaCl, 7 mM β-mercaptoethanol, 20 mM Imidazole supplemented with cOmplete
566 EDTA-free protease Inhibitor Cocktail (MilliporeSigma) and lysed by microfluidizer. The lysate
567 was centrifuged at 20,000×g at 4°C for 30 min to remove cell debris. The protein was first
568 purified by Ni-NTA, eluted around 50 mM imidazole, and then dialyzed against 25 mM Tris-HCl
569 (pH 7.5 at RT), 250 mM NaCl, 7 mM β-mercaptoethanol. 6×His-MBP tag was cleaved by 6×His-
570 MBP-TEV protease (S219V) (purified in house) during the dialysis. The cleaved 6×His-MBP tag
571 and TEV protease were removed through the second round of Ni-NTA column. Flow through
572 and wash fractions were dialyzed against buffer S [25 mM Tris-HCl (pH 7.5 at RT), 250 mM NaCl,
573 7 mM β-mercaptoethanol] and concentrated by Amicon Ultra (10 kDa cutoff). The protein was
574 snap-frozen in liquid nitrogen in storage buffer [25 mM Tris-HCl (pH 7.5 at RT), 250 mM NaCl, 7
575 mM β-mercaptoethanol, 20% glycerol] and stored at -80 °C.
576
577 iLID-YFP-MARCKS
578 The bacteria transformed with pET28-2×Strep-iLID-EYFP-MARCKS were cultured overnight in LB
579 broth supplemented with 50 µg/mL Kanamycin and 25 µg/mL Chloramphenicol (LB/Kan/Cam).
580 Pre-culture was inoculated to LB/Kan/Cam and cultured at 37°C until OD600 reached around

581 0.6. Protein expression was induced by adding 300 μM IPTG and allowed to proceed for 17
582 hours at 23°C in the presence of 6 μM FMN. The cells were resuspended with buffer L1 [50 mM
583 Tris-HCl (pH 7.5 at RT), 200 mM NaCl, 1 mM EDTA, 7 mM β-mercaptoethanol] and lysed by
584 microfluidizer. The lysate was centrifuged at 20,000×g at 4°C for 30 min to remove cell debris.
585 The supernatant was applied to Strep-Tactin XT (IBA Lifesciences) equilibrated with buffer L1
586 and the protein was eluted with 50 mM biotin in buffer L1. The elution was dialyzed against
587 buffer L2 [25 mM Tris-HCl (pH 7.5 at RT), 200 mM NaCl, 7 mM β-mercaptoethanol] and
588 concentrated by Amicon Ultra (10 kDa cutoff). The protein was snap-frozen in liquid nitrogen in
589 storage buffer [25 mM Tris-HCl (pH 7.5 at RT), 200 mM NaCl, 7 mM β-mercaptoethanol, 30%
590 glycerol] and stored at -80 °C.
591
592 iLID-YFP-SNAP
593 The bacteria transformed with pET28-2×Strep-iLID-EYFP-SNAP were cultured overnight in LB
594 broth supplemented with 50 μg/mL Kanamycin and 25 μg/mL Chloramphenicol (LB/Kan/Cam).
595 Pre-culture was inoculated to LB/Kan/Cam and cultured at 37°C until OD_{600} reached around 0.5.
596 Protein expression was induced by adding 300 μM IPTG and allowed to proceed for 20 hours at
597 23°C in the presence of 6 μM FMN. The cells were resuspended with buffer L1 (50 mM Tris-HCl
598 (pH 7.5 at RT), 200 mM NaCl, 1 mM EDTA, 7 mM β-mercaptoethanol) and lysed by
599 microfluidizer. The lysate was centrifuged at 20,000×g at 4°C for 30 min to remove cell debris.
600 The supernatant was applied to Strep-Tactin XT (IBA Lifesciences) equilibrated with buffer L and
601 the protein was eluted with 50 mM biotin in buffer L1. The elution was further purified by
602 Superdex 200 increase 10/300 GL column in the buffer L2 [25 mM Tris-HCl (pH 7.5 at RT), 200
603 mM NaCl, 7 mM β-mercaptoethanol] and concentrated by Amicon Ultra (10 kDa cutoff). The
604 protein was snap-frozen in liquid nitrogen in storage buffer [25 mM Tris-HCl (pH 7.5 at RT), 200
605 mM NaCl, 7 mM β-mercaptoethanol, 30% glycerol] and stored at -80 °C.
606
607 GST-pVCA-SspB-mCherry
608 The bacteria transformed with pGEX2T-GST-pVCA-3Csite-SspB(micro)-mCherry-TEVsite-6×His
609 were cultured overnight in LB broth supplemented with 100 μg/mL Ampicillin and 25 μg/mL
610 Chloramphenicol (LB/Amp/Cam). Pre-culture was inoculated to LB/Amp/Cam and cultured at
611 37°C until OD_{600} reached around 0.5–0.6. After cooling the culture on ice, protein expression
612 was induced by adding 300 μM IPTG and allowed to proceed for 24–26 hours at 18°C. The cells
613 were resuspended with buffer V (50 mM HEPES-NaOH (pH 7.5), 150 mM NaCl, 10% glycerol, 14
614 mM b-mercaptoethanol, 1 mM EDTA, 1 mM PMSF, 100 μg/mL DNase, supplemented with
615 cOmplete EDTA-free protease inhibitor cocktail) and lysed by microfluidizer. The lysate was
616 centrifuged at 20,000×g at 4°C for 30 min to remove cell debris. To enhance resin binding, final
617 5 mM DTT was added to the lysate. The lysate was applied to glutathione sepharose
618 equilibrated with buffer V [50 mM HEPES-NaOH (pH 7.5) 150 mM NaCl, 10% glycerol, 7 mM b-

619 mercaptoethanol, and 1 mM PMSF], and the protein was eluted with 20 mM glutathione in
620 buffer V (pH was adjusted between 7.0–8.0 by NaOH). The elution was then purified by Ni-NTA
621 and eluted with 50–500 mM imidazole. After concentrated by Amicon Ultra (10 kDa cutoff), the
622 protein was further purified by Superdex 200 increase 10/300 GL column in buffer V and
623 concentrated again by Amicon Ultra (10 kDa cutoff). The protein was snap-frozen in liquid
624 nitrogen and stored at -80 °C.
625
626 mCherry-SspB-mDia1
627 The bacteria transformed with pET28-2×Strep-mCherry-SspB(micro)-mDia1(FH1-FH2-DAD)
628 were cultured overnight in LB broth supplemented with 50 µg/mL Kanamycin and 25 µg/mL
629 Chloramphenicol (LB/Kan/Cam). Pre-culture was inoculated to LB/Kan/Cam and cultured at
630 37°C until OD_{600} reached around 0.5–0.6. After cooling the culture on ice, protein expression
631 was induced by adding 300 µM IPTG and allowed to proceed for 24 hours at 16°C. The cells
632 were resuspended with buffer D [50 mM Tris-HCl (pH 7.5), 500 mM NaCl, 10% glycerol, 1 mM
633 DTT, 1 mM EDTA, 1 mM PMSF, 100 µg/mL DNase, supplemented with cOmplete EDTA-free
634 protease inhibitor cocktail] and lysed by microfluidizer. The lysate was centrifuged at 20,000×g
635 at 4°C for 30 min to remove cell debris. The supernatant was applied to Strep-Tactin XT (IBA
636 Lifesciences) equilibrated with buffer D1 (50 mM Tris-HCl (pH 7.5), 500 mM NaCl, 10% glycerol,
637 1 mM DTT, 1 mM EDTA, 1 mM PMSF) and the protein was eluted with 50 mM biotin in buffer
638 D1. The elution was concentrated by Amicon Ultra (10 kDa cutoff) and dialysed against buffer
639 D2 [25 mM HEPES-NaOH (pH 7.5), 150 mM NaCl, 7 mM b-mercaptoethanol, 10% glycerol]. The
640 protein was further purified by Superdex 200 increase 10/300 GL column in buffer D2 and
641 concentrated again by Amicon Ultra (10 kDa cutoff). The protein was snap-frozen in liquid
642 nitrogen and stored at -80 °C.
643
644 Capping protein
645 The bacteria transformed with pET28-6×His-2×Strep-TEVsite-Capβ2(mouse)-Capα1(mouse)
646 were cultured overnight in LB/Kan/Cam. Pre-culture was inoculated to LB/Kan/Cam and
647 cultured at 37°C until OD_{600} reached around 0.7. Protein expression was induced by adding 300
648 µM IPTG and allowed to proceed for 24 hours at 18°C. The cells were re-suspended with 50 mM
649 Tris-HCl (pH 7.5 at RT), 150 mM NaCl, 14 mM β-mercaptoethanol, 1 mM EDTA, 1 mM PMSF,
650 100 µg/mL DNase and lysed by microfluidizer. The lysate was centrifuged at 20,000×g at 4°C for
651 30 min to remove cell debris. The supernatant was applied to Strep-Tactin XT 4Flow (IBA
652 Lifesciences) equilibrated with buffer C1 [50 mM Tris-HCl (pH 7.5 at RT), 150 mM NaCl, 7 mM
653 β-mercaptoethanol] and the protein was eluted with 50 mM biotin in buffer C1. The elution
654 was dialyzed against buffer C2 [25 mM Tris-HCl (pH 7.5 at RT), 150 mM NaCl, 7 mM β-
655 mercaptoethanol]. 6×His-2×Strep tag was cleaved by 6×His-MBP-TEV protease (S219V) (purified
656 in house) during the dialysis. The cleaved 6×His-2×Strep tag and TEV protease were removed

657 through Ni-NTA column. Flow through and wash fractions were dialyzed against buffer and
658 concentrated by Amicon Ultra (10 kDa cutoff). The protein was snap-frozen in liquid nitrogen in
659 buffer C2 and stored at -80 °C.
660
661 **Pyrene-actin polymerization assay**
662 For pyrene actin assay, actin was purified by size exclusion column. One milligram of actin
663 (Cytoskeleton Inc. AKL99-B) was dissolved in 400 µL G-buffer [2 mM Tris-HCl (pH 7.5 at RT), 0.1
664 mM $CaCl_2$, 0.2 mM ATP, 0.5 mM DTT, 1 mM NaN_3] and dialyzed against the same buffer. After 3
665 days dialysis with daily buffer exchange, the actin was purified by Superdex 200 Increase
666 10/300 GL column (GE Healthcare) to separate monomer fraction from a fraction occasionally
667 appear at larger size molecular size (smaller elution volume). The purified actin was stored at
668 4°C in a dialyzed manner against G-Buffer with twice a week buffer exchange.
669 Pyrene-actin polymerization assay was performed with FluoroMax 3 and Datamax software.
670 Pyrene fluorescence and its kinetics were measured by 365 nm excitation (1 nm bandwidth)
671 and 407 nm emission (5 nm bandwidth). The reaction was prepared by following the previously
672 reported method (*127*), except that the reaction was 50 µL in quartz cuvettes (Hellma, 105-251-
673 15-40).
674
675 **GUV preparation by emulsion transfer**
676 Lipid-in-oil solution was prepared as follows. Chloroform solutions of lipids were mixed in 5 mL
677 glass vial, dried at 70°C with N_2 gas flow, and left in vacuum 3 hours to overnight. The amounts
678 of lipids were typically 6.5 µmol (1.3 mM, 1 mg/mL at final concentration in oil) for 40 mol%
679 POPS/60 mol% POPC mixture (MARCKS peptide anchoring) and 1.5 µmol (0.3 mM, 0.23 mg/mL
680 at final concentration in oil) for 2 mol% Bendylguanine-conjugated lipid/98 mol% POPC and
681 100% POPC (SNAP-tag anchoring). was dissolved in 5 mL of oil mixture (90 volume%
682 hexadecane, 10 volume% silicone oil) by heating at 80˚C for 1–2 hours, then brought to RT.
683 For iLID-SspB translocation experiments, inner solution contained 4 µM iLID-YFP-SNAP (or iLID-
684 EYFP-MARCKS) and 1 µM mCherry-SspB(micro) in buffer (22.5 mM Tris-HCl (pH 7.5 at RT), 122.5
685 mM NaCl, 2 mM $MgCl_2$, 240 mM sucrose, 0.7 mM β-mercaptoethanol, and 3% glycerol). Outer
686 solution was prepared by replacing protein fractions of inner solution with their buffers and
687 sucrose with glucose.
688 For actin polymerization experiments, inner solution was prepared by mixing 10 µL of actin
689 (10% Alexa 647 labelled) in G-buffer and 10 µL of other proteins solution similarly to pyrene
690 actin polymerization assay. At the final concentration, inner solution typically contained 11.75
691 µM iLID-EYFP-SNAP, 1 µM GST-pVCA-SspB(micro)-mCherry, 1 µM mCherry-SspB(micro)-mDia1,
692 7.5 µM actin, 150 nM Arp2/3, 50 nM capping protein, 3 µM profilin, 2 µM cofilin, 1 µM creatine
693 kinase in the buffer (5.9 mM Tris-HCl (pH 7.5 at RT), 1.3 mM HEPES-NaOH (pH 7.5 at RT), 7.7
694 mM Imidazole (pH 8.0 at RT), 27 µM KH_2PO_4, 74 µM Na_2HPO_4, 39 mM KCl, 33 mM NaCl, 0.8

695 mM $MgCl_2$, 43 µM $CaCl_2$, 1.1 mM EGTA, 1.2 mM β-mercaptoethanol, 0.21 mM DTT, 0.43 mM
696 NaN_3, 1 mM ATP, 25 mM creatine phosphate, 240 mM sucrose and 2.8% glycerol). Outer
697 solution was prepared by replacing protein fractions of inner solution with their buffers and
698 sucrose with glucose. Protein and buffer conditions are summarized in Supplementary table 1.
699 GUVs were prepared as previously reported (*55*, *128*). Briefly, oil-buffer interface was created
700 by layering 250 µL lipid-in-oil solution on top of 250 µL outer buffer in 1.5 mL tube. Water-in-oil
701 emulsion was made by vigorously pipetting 20 µL of inner solution in 250 µL of lipid-in-oil
702 solution and gently added to the top of the oil-buffer layers. The emulsions were transferred
703 through the oil-buffer interface by centrifugation at 2500×g for 2 min at RT. GUVs were
704 collected by pipetting.
705
706 **Image acquisition and analysis**
707 For imaging GUVs, 8-well glass chamber slides (ThermoFisher Scientific, 154534) were
708 pretreated with 10 mg/mL BSA in PBS for 10 minutes and washed with MilliQ water twice.
709 LSM780 confocal microscope (Zeiss) equipped with Plan-Aprochromat 63X/1.40na oil
710 immersion DIC objective lens (Zeiss 420782-9900) was used for imaging and light stimulation of
711 GUVs. YFP, mCherry, and Alexa Fluor 647 were imaged with 514, 561, and 633 nm excitation
712 lasers, respectively. Blue light illumination for iLID stimulation was performed by using
713 bleaching function with 458 nm laser at intensity 1.0–5.0%, scan speed 6 (pixel dwell time = 6.3
714 µsec). Main beam splitters MBS458/561, MBS 488/561/633, and MBS 458/514 were used for
715 458 and 561, 633, and 514 nm excitation, respectively. The imaging was performed at room
716 temperature. Data were analyzed by Fiji software (*129*).
717
718 **Live cell CID experiments**
719 DNA constructs: Four plasmids were used which encoded Lyn-CFP-FRB (*130*), YFP-FKBP (*130*),
720 YFP-FKBP-Tiam1 (*124*), YFP-FKBP-pVCA, and YFP-FKBP-mDia1.
721 Cell culture: HEK293T cells (ATCC) were cultured in DMEM (Corning, 10-013-CV) supplemented
722 with 10% fetal bovine serum (Corning, 35-010-CV) and 1% penicillin-streptomycin
723 (ThermoFisher, 15140163).
724 Transient transfection: HEK293T cells were seeded at a density of 9,000-12,000 cells in an 8-
725 well chamber slide. A solution of 0.3 µg of DNA, 1 µL of FuGENE HD, and 30 µL of Opti-MEM per
726 well was added for transfection. FRB:FKBP pairs were cotransfected in a 1:1 or 1:2 ratio. Cells
727 were incubated at 37°C with 5% CO_2 and 95% humidity for 24–48 h before imaging.
728 Microscopes and imaging: Live cell imaging of actin NPF recruitment to the cell membrane was
729 performed using an Eclipse Ti inverted fluorescence microscope (Nikon) with a 100x Oil
730 objective lens and Andor Zyla 4.2 plus sCMOS camera, or with a 60x Oil, TIRF 60x Oil, or TIRF
731 100x Oil objective lens and ORCA-Fusion Digital CMOS camera. Images were captured every 1
732 min for 30-120 min, where within 5 min of starting, 0.1 µM rapamycin was added. Nikon

microscopes were driven by NIS-Elements software (Nikon). All live cell imaging was performed at 37 °C with 5% CO_2 and humidity control by a stage top incubator. Image processing and analysis were performed by Fiji software.

Data analysis: Per transfection sample, each cell from the image set was counted between three categories. The categories were no change, lamellipodia, and filipodia. Cells with lamellipodia or filipodia pre-rapamycin were not counted unless new membrane protrusions formed after rapamycin addition. If the cell under observation did not produce any new lamellipodia or filipodia after addition of rapamycin, then it was counted as no change. Only healthy cells fully in the plane of view with clear expression of both FRB and FKBP constructs were counted. If there was any doubt in the phenotype of the cell, then it was not included in the count.

Statistics

1. The cell counts for each category were summed across all experiments, and this sum was divided by the total number of cells to get a percentage of cells belonging to each category when a certain actin NPF was recruited to the membrane.

2. For each image set collected from a transfection sample, the categorized cell counts were divided by the total cell count to get percentages. For each actin NPF, the percentages from all transfection samples were averaged. These averages were analyzed by two-tailed Student's t-test assuming equal variance (checked with F-test) in order to establish the significance of lamellipodia or filopodia detection between transfection samples.

Acknowledgement

We thank Yubin Zhou for TEV protease plasmid; Masato Kanemaki for pET28-2×Strep-tag plasmid; Miho Iijima for pGEX-2T plasmid; Bin Wu for Phage-ubc-nls-ha-tdMCP-SNAP plasmid; Roberto Dominguez for pCold-mDia1 plasmid, Saki Takayanagi for constructing GST-pVCA-FKBP-EYFP plasmid. We also thank Yusuke Sato, Taro Toyota, Pushpendra Singh, Tetsuya Kotani, Takeya Masubuchi for technical advice on the experiments. We appreciate Erin D. Goley for technical support of pyrene assay and insightful comments on actin preparation. We also appreciate Julie Plastino and Cecile Sykes for pET3d-Capβ2(mouse)-Capα1(mouse) plasmid and insightful advice on protein purification. Our appreciation extends to Pablo A. Iglesias for fruitful discussion. We thank our lab members, including Allen Kim, Abhijit Deb Roy, Helen D. Wu, Yuta Nihongaki for constructive discussion. We thank Kyoko Chiba for technical support on protein purification. We also thank Robert DeRose for proofreading the manuscript and experimental support. FRIS CoRE (a shared research environment in Tohoku University) is also acknowledged. This study was supported by the PRESTO program of the Japan Science and Technology Agency (JPMJPR12A5 to TI, JPMJPR20KA to HTM), National Institute of Health (5R01GM123130, R01GM136858, R35GM149329 to TI, and R35GM128786 to BC), and the

National Science Foundation (000819255 to TI, JL, BC). TI was also supported by Nitto Denko Corp. HTM was supported by Postdoctoral Fellowships from the Japan Society for the Promotion of Science. SR was supported by the National Science Foundation and the Japan Society for the Promotion of Science (JSPS) East Asia and Pacific Summer Institutes and Johns Hopkins Lucille Elizabeth Hay graduate fellowships.

Author contributions

HTM, SR, and TI conceived the project. HTM performed most of the experiments and analyzed the data with contributions from SR, HN, BC, SM, SMN and TI. SR established GUV preparation method. WR performed in-cell CID experiment and analyzed the data. DN, DAK, and BC provided cytoskeleton proteins. TM provided benzylguanine-conjugated lipid. HTM wrote the manuscript in consultation with TI. HTM, SR, and TI edited the manuscript. All the authors contributed to the final version of the manuscript.

Figure Legends

Fig. 1. Reversible and asymmetric control of protein localization with iLID-SspB within GUVs. (A) Schematic representation of iLID-SspB reaction with global light stimulation. iLID was tethered on the membrane via the interaction between SNAP-tag and bendylguanine-conjugated lipids. Upon blue light illumination, Jα helix of iLID extends to expose the binding site for SspB, whereas in the dark, iLID reverses to its closed state and releases SspB. (B) Representative images of iLID-YFP-SNAP and mCherry-SspB. Scale bar, 10 µm. Blue bar indicates the period of blue light illumination. (C) Time course of membrane/lumen ratio of mCherry-SspB signal (n=5). Error bars indicate standard deviation. Blue area indicates the period of blue light stimulation. Triangles indicate timepoints represented in (B). (D) Schematic representation of iLID-SspB reaction with local light stimulation. (E) Representative images of mCherry-SspB. Scale bar, 10 µm. Yellow box indicates the area of blue light illumination. (F) Membrane/lumen ratio of mCherry-SspB for the representative image shown. The distance is measured from the center of blue light illumination along the perimeter of the GUV. (G) Representative image and kymograph of repetitive and reversible SspB translocation. Kymograph shows membrane signal of mCherry-SspB.

Fig. 2. Reversible light control of actin cytoskeleton within GUVs. (A) Bulk pyrene actin polymerization assay with 1 µM actin (5% pyrene labeled), 10 nM Arp2/3, and 100 nM NPFs. (-NPF) represents actin and Arp2/3 only condition. (B) Schematic representation of light inducible actin polymerization. Translocation of pVCA-SspB-mCherry increases local concentration of

808 pVCA on the membrane and enhances actin polymerization. (C) Representative images of
809 pVCA-SspB-mCherry and Alexa 647 actin. Blue bar indicates the period of blue light illumination.
810 (D), (E) Time course of membrane/lumen ratio of mCherry and Alexa 647 actin. +: full set of
811 components (n=4). -Light: no blue light stimulation (n=3). -pVCA: pVCA-SspB-mCherry was
812 replaced with mCherry-SspB (n=4). -Arp2/3: Arp2/3 was omitted (n=4). Error bars indicate 95%
813 CI. Triangles indicate timepoints represented in (C). (F) Representative images of reversible
814 actin polymerization. Blue bars indicate the period of blue light illumination. (G) Time course of
815 membrane/lumen ratio of pVCA-SspB-mCherry and Alexa 647-labeled actin in (F). Triangles
816 indicate timepoints represented in (F).
817
818 **Fig. 3. Asymmetric light control of actin cytoskeleton within GUVs.** (A) Schematic
819 representation of iLID-SspB reaction with local light stimulation. (B, D) Representative images of
820 light inducible asymmetric actin polymerization. Yellow boxes indicate the area of blue light
821 illumination. (C, E) Kymograph of membrane pVCA-SspB and actin signals. Blue bars indicate the
822 period of blue light illumination. Triangles indicate timepoints represented in (B, D).
823
824 **Fig. 4. mDia1-mediated actin polymerization drives protrusive motility of GUVs.** (A) Schematic
825 representation of light inducible membrane protrusion driven by pVCA and mDia1-mediated
826 actin polymerization. (B) Representative images of pVCA-mDia1-mediated movement of GUVs.
827 Yellow boxes indicate the area of blue light stimulation. Dotted line shows the initial position of
828 the GUV. (C) Representative images of iLID-EYFP-SNAP showing the increase in adhesive area
829 and vesicle deformation into dome-like shape. Bottom plane indicates the confocal plane right
830 above the bottom substrate. Side view is reconstituted from z-stack. Dotted line shows the
831 adhesive area of the previous images. (D) Color-coded boundaries of GUVs. The data
832 correspond as follows. Left: Fig. 4B. Middle: Fig. S16A. Right: Fig. S16B. (E, F) Kymographs of
833 membrane signal of mCherry and actin Alexa-647 and membrane protrusions. Triangles in (E)
834 indicate the timepoints represented in (B, C). Data of (E) and (F) corresponds to Fig. 4 (B) and
835 Fig. S16A, respectively. (G) Distance the front (illuminated) side of GUV membrane moved
836 forward. pVCA+mDia1 (1 μM GST-pVCA-SspB-mCherry + 1 μM mCherry-SspB-mDia1, n=14
837 vesicles), mDia1 (1 μM mCherry-SspB-mDia1, n=12 vesicles), pVCA (1 μM GST-pVCA-SspB-
838 mCherry, n=12 vesicles). Error bars indicate standard error of the mean (SEM). (H) DMSO (n=9
839 vesicles), 30 μM LatA (Latrunculin A) (n=10 vesicles). DMSO, ΔDAD: mCherry-SspB-mDia1 (FH1-
840 FH2-DAD) was replaced with mCherry-SspB-mDia1(FH1-FH2) (n=13 vesicles). 30 μM SMIFH2
841 (n=6 vesicles). Error bars indicate standard error of the mean (SEM). (I) A GUV deformed into
842 dome-like shape after movement. Upper images: before light stimulation. Lower images: after
843 light stimulation. The data corresponds to Fig. S16C.
844

845 **Fig. S1. Proteins purified in this study.** (A) SDS-PAGE results of purified proteins. Blue:
846 Coomassie brilliant blue staining. Gray: SYPRO Ruby staining. Most mCherry-tagged proteins
847 show two extra bands due to a known chromophore cleavage reaction during the boiling
848 process (*131*, *132*). (B) Domain structures of NPFs used in this study.
849
850 **Fig. S2. Optimization of membrane anchoring of iLID.** (A),(D),(G),(I): Schematic representations
851 of membrane anchoring of iLID. (B),(C),(E),(F),(H),(J): Confocal images of iLID variants and
852 mCherry-SspB. (B) His-tag Ni-NTA pair caused non-specific membrane recruitment of SspB. This
853 is possibly caused by the presence of 2×Strep-iLID-YFP-6×His because mCherry-SspB itself did
854 not show non-specific binding to the membrane of 5%Ni-NTA DGS/95%POPC (C). (E),(F)
855 MARCKS-ED peptide requires high percentage of PS and PEGylated-lipids to reduce non-specific
856 binding of SspB. (H) Biotin-StrepTactin-Streptag also caused non-specific membrane binding of
857 SspB. (J) The data correspond with Fig. 1B.
858
859 **Fig. S3. Asymmetric control of protein localization with iLID-SspB within GUVs.** (A) Time
860 course of membrane/lumen ratio of mCherry-SspB signal in the illuminated area (n=5). Error
861 bars indicate 95% CI. Blue area indicates the time window of blue light stimulation. The data
862 corresponds to Fig. 1E and F. (B, C) Confocal images and time course of membrane/lumen ratio
863 of mCherry-SspB signal responding to repetitive local light illuminations. The data corresponds
864 to Fig. 1G.
865
866 **Fig. S4. Optimization of ActA-SspB.** (A) Pyrene actin polymerization assay. The reaction was
867 performed with 1 μM actin (5% pyrene labeled), 10 nM Arp2/3, and 100 nM ActA variants or
868 GST-VCA. (B) Fluorescence intensity/time in 0–6 min of (A) was plotted as bar chart. (C–E) Light
869 inducible local membrane recruitment of ActA (C) Confocal images of ActA translocation. Yellow
870 boxes indicate the area of blue light illumination. (D) Time course of membrane/lumen ratio of
871 ActA-SspB variants (n≥5 for each variant). Error bars indicate SEM. Blue bar indicates the time
872 window of blue light stimulation. (E) Average membrane/lumen ratio of mCherry signal. In each
873 condition, left and right bars indicate before and after light stimulation, respectively. The
874 numbers on the bar chart indicate the fold change after stimulation.
875
876 **Fig. S5. Light inducible actin polymerization with global ActA membrane recruitment.** iLID-
877 EYFP-MARCKS (5 μM), ActA-SspBnano-mCherry (2 μM), actin (1.5 μM, 10% Alexa-647 labeled),
878 and Arp2/3 (150 nM) were encapsulated in GUVs containing 60 mol% POPC/40 mol% POPS.
879 Blue light was applied to the entire GUV. (A) Representative images of ActA(1–183)-SspB(nano)-
880 mCherry and actin Alexa-647. All components (n=4): w/o ActA: ActA(1–183)-SspB(nano)-
881 mCherry was replaced with mCherry-SspB(micro) (n=3), w/o Arp2/3: Arp2/3 was omitted (n=3).
882 No Light: no blue light stimulation (n=3). (B, C) Time course of membrane/lumen ratio of

883 mCherry and actin Alexa 647. (D) Bar chart of membrane/lumen ratio of actin Alexa 647 before
884 (0 min) and after (40 min) light stimulation. Error bars indicate SEM.
885
886 **Fig. S6. Asymmetric ActA membrane recruitment fails to induce directed actin polarization**
887 **toward local light illumination.** iLID-EYFP-MARCKS (5 µM), ActA-SspBnano-mCherry (2 µM),
888 actin (1.5 µM, 10% Alexa-647 labeled), and Arp2/3 (150 nM), 1 mM ATP were encapsulated in
889 GUVs containing 60 mol% POPC/40 mol% POPS. Yellow boxes indicate the area of blue light
890 illumination. Although ActA creates asymmetric distribution, actin patches randomly
891 distributed due to the diffusion on the membrane.
892
893 **Fig. S7. Global ActA membrane recruitment fails to induce actin polymerization on the**
894 **membrane in the presence of profilin, cofilin, and capping protein.** 15 µM iLID-YFP-MARCKS, 5
895 µM ActA(1-183)-SspB(nano)-mCherry, 7.5 µM actin (10% Alexa 647 labeled), 150 nM Arp2/3, 3
896 µM profilin, cofilin, and capping protein were encapsulated in GUVs containing 60 mol%
897 POPC/40 mol% POPS. Blue bars indicate the period of blue light illumination.
898
899 **Fig. S8. Pyrene actin polymerization assay.** (A, B) The reactions were performed with 2 µM
900 actin (5% pyrene labeled), 10 nM Arp2/3, and 100 nM NPFs at RT. (-) represents actin and
901 Arp2/3 only condition. (C) The reactions were performed with 2 µM actin (5% pyrene labeled)
902 with the indicated factors.
903
904 **Fig. S9. Light control of actin cytoskeleton with pVCA-SspB-mCherry.** The data correspond to
905 Fig. 2C–E. (+) condition contains 15 µM iLID-YFP-MARCKS, 4.2 µM pVCA-SspB(nano)-mCherry,
906 7.5 µM actin (10% Alexa 647 labelled), 150 nM Arp2/3, 100 nM capping protein, 3 µM profilin, 4
907 µM cofilin, and 1 mM ATP. In (-light) and (-Arp2/3) conditions, blue light illumination or Arp2/3
908 was omitted from (+) condition, respectively. In (-pVCA) condition, pVCA-SspB(nano)-mCherry
909 was replaced with mCherry-SspB(micro).
910
911
912 **Fig. S10. Representative images of reversible actin polymerization.** Confocal images and time
913 course of membrane/lumen ratio of pVCA-SspB-mCherry and Alexa 647-labeld actin. Blue bars
914 on images and blue regions in graphs indicate timepoints with blue light illumination. This
915 figure corresponds with Fig. 2F, G.
916
917 **Fig. S11. Asymmetric actin polymerization induced by pVCA.** (A, B) Confocal images of local
918 pVCA recruitment and actin polymerization. Yellow boxes indicate areas of blue light
919 illumination. (A) The data corresponds to Fig. 3B and C. In (B), Vesicle movement toward light

920 stimulation was observed. Gray scaled images were created by averaging pVCA and actin
921 images. Dotted circles indicate positions of vesicles in the images of one above.
922
923 **Fig. S12. Quantitative analysis of mDia1-induced filopodia formation in Cos7 cells.** (A)
924 Schematic representation of chemically-inducible mDia1 translocation and membrane
925 protrusions. (B, C) Confocal images of plasma membrane recruitment of mDia1 and subsequent
926 filopodia formation. Cos7 cells were transfected with Lyn-ECFP-FRB, Lifeact-mCherry, and either
927 of YFP-FKBP or YFP-FKBP-mDia1. At time 0, 100 nM rapamycin was added. Green: YFP-FKBP or
928 YFP-FKBP-mDia1. Magenta: Lifeact-mCherry. (B) YFP-FKBP control. (C) YFP-FKBP-mDia1. (D)
929 Zoomed-up view of filopodia extension. Images were acquired every 1.5 minutes. The bottom is
930 merged image. (E) Quantification of mDia1-induced filopodia. Number of filopodia whose
931 length is longer than 15 µm was counted. P-values: ****: < 0.0001. Wilcoxon rank sum test. YF
932 (YFP-FKBP): n=36 cells. YF-mDia1 (YFP-FKBP-mDia1): n=33 cells. (F–H) Quantification of the
933 phenotypes observed after plasma membrane translocation of mDia1, pVCA, Tiam1 (Rac1 GEF),
934 and control protein YFP-FKBP.
935
936 **Fig. S13. mDia1-mediated GUV movement and the comparison between mDia1 and pVCA +**
937 **mDia1 system.** (A) Representative images of mDia1-mediated GUV movement. Yellow boxes
938 indicate the area of blue light stimulation. Dotted lines indicate the initial position of the GUV.
939 (B, C) Time course of the distance the front (illuminated) side of GUV membrane moved
940 forward. Each line represents each GUVs. Insets show the initial response. (D, E) Quantification
941 of the initial velocity and the distance the front side of GUV membrane moved forward. P
942 values of Steel-Dwass test (two sided) are indicated. pVCA + mDia1: n=22 vesicles. mDia1: n=11
943 vesicles. pVCA: n=12 vesicles. Box whisker plots represent median, 1st, 3rd quartiles and
944 1.5×inter-quartile range.
945
946 **Fig. S14. Local protrusions in pVCA + mDia1 GUVs.** Representative images of local protrusions
947 seen in pVCA + mDia1 GUVs. Yellow boxes indicate the area of blue light stimulation. Dotted
948 lines indicate the initial position of the GUV. White arrows indicate where local protrusions
949 arose.
950
951 **Fig. S15. Lack of vesicle movement and shape change with mCherry-SspB.** With pVCA-SspB-
952 mCherry and mCherry-SspB-mDia1 being replaced with mCherry-SspB, GUVs neither moved nor
953 changed their shape after blue light illumination. (A) Time course of the distance the front
954 (illuminated) side of GUV membrane moved forward. pVCA + mDia1 GUVs: n=6 vesicle. SspB
955 GUVs: n=4 vesicles. Error bars indicate SEM. (B) 3D reconstitution of iLID-YFP-SNAP images
956 before and after blue light illumination.
957

958 **Fig. S16. Representative images of pVCA-mDia1-mediated movement of GUVs.** (A, B)
959 Representative images of pVCA-mDia1-mediated movement of GUVs. Yellow boxes indicate the
960 area of blue light stimulation. Dotted lines indicate the initial position of the GUV. White arrows
961 indicate where local protrusions arose. (C) Distance the front side of GUV membrane moved
962 forward. Data was quantified from the images of (B). Blue areas indicate the periods of blue
963 light stimulation.
964
965

References

1. M. Miyata, R. C. Robinson, T. Q. P. Uyeda, Y. Fukumori, S. ichi Fukushima, S. Haruta, M. Homma, K. Inaba, M. Ito, C. Kaito, K. Kato, T. Kenri, Y. Kinosita, S. Kojima, T. Minamino, H. Mori, S. Nakamura, D. Nakane, K. Nakayama, M. Nishiyama, S. Shibata, K. Shimabukuro, M. Tamakoshi, A. Taoka, Y. Tashiro, I. Tulum, H. Wada, K. ichi Wakabayashi, Tree of motility – A proposed history of motility systems in the tree of life. *Genes to Cells* **25**, 6–21 (2020).

2. K. Y. Wan, G. Jékely, Origins of eukaryotic excitability. *Phil. Trans. R. Soc. B* **376**, 20190758 (2021).

3. T. Froese, N. Virgo, T. Ikegami, Motility at the Origin of Life: Its Characterization and a Model. *Artificial Life* **20**, 55–76 (2014).

4. P. N. Devreotes, S. Bhattacharya, M. Edwards, P. A. Iglesias, T. Lampert, Y. Miao, Excitable Signal Transduction Networks in Directed Cell Migration. *Annu. Rev. Cell Dev. Biol.* **33**, 103–125 (2017).

5. L. K. Fritz-Laylin, The evolution of animal cell motility. *Current Biology* **30**, R477–R482 (2020).

6. S. SenGupta, C. A. Parent, J. E. Bear, The principles of directed cell migration. *Nat Rev Mol Cell Biol* **22**, 529–547 (2021).

7. S. B. Carter., Effects of Cytochalasins on Mammalian Cells. Nature 213, 261-264 (1967).

8. T. D. Pollard, S. Ito, CYTOPLASMIC FILAMENTS OF *AMOEBA PROTEUS*. *The Journal of Cell Biology* **46**, 267–289 (1970).

9. J. V. Small, G. Isenberg, J. E. Celis, Polarity of actin at the leading edge of cultured cells. *Nature* **272**, 638–639 (1978).

10. L. G. Tilney, S. Inoué, Acrosomal reaction of Thyone sperm. II. The kinetics and possible mechanism of acrosomal process elongation. *J Cell Biol* **93**, 820–827 (1982).

11. J. A. Theriot, The Polymerization Motor. *Traffic* **1**, 19–28 (2000).

12. T. D. Pollard, Landmarks in the discovery of a role for actin in cell locomotion. *Molecular Biology of the Cell*, 4 (2022).

13. P. Lappalainen, T. Kotila, A. Jégou, G. Romet-Lemonne, Biochemical and mechanical regulation of actin dynamics. *Nat Rev Mol Cell Biol*, doi: 10.1038/s41580-022-00508-4 (2022).

14. P. Friedl, K. Wolf, Plasticity of cell migration: a multiscale tuning model. *Journal of Cell Biology* **188**, 11–19 (2010).

997 15. T. Lämmermann, M. Sixt, Mechanical modes of 'amoeboid' cell migration. *Current Opinion*
998 *in Cell Biology* **21**, 636–644 (2009).

999 16. M. Garrido-Casado, G. Asensio-Juárez, M. Vicente-Manzanares, Nonmuscle Myosin II
1000 Regulation Directs Its Multiple Roles in Cell Migration and Division. *Annu Rev Cell Dev Biol*
1001 **37**, 285–310 (2021).

1002 17. D. Knecht, W. Loomis, Antisense RNA inactivation of myosin heavy chain gene expression in
1003 Dictyostelium discoideum. *Science* **236**, 1081–1086 (1987).

1004 18. A. De Lozanne, J. A. Spudich, Disruption of the Dictyostelium myosin heavy chain gene by
1005 homologous recombination. *Science* **236**, 1086–1091 (1987).

1006 19. A. B. Verkhovsky, T. M. Svitkina, G. G. Borisy, Self-polarization and directional motility of
1007 cytoplasm. *Current Biology* **9**, 11-S1 (1999).

1008 20. R. J. Eddy, L. M. Pierini, F. Matsumura, F. R. Maxfield, Ca2+-dependent myosin II activation
1009 is required for uropod retraction during neutrophil migration. *J Cell Sci* **113 (Pt 7)**, 1287–
1010 1298 (2000).

1011 21. T. Lämmermann, B. L. Bader, S. J. Monkley, T. Worbs, R. Wedlich-Söldner, K. Hirsch, M.
1012 Keller, R. Förster, D. R. Critchley, R. Fässler, M. Sixt, Rapid leukocyte migration by integrin-
1013 independent flowing and squeezing. *Nature* **453**, 51–55 (2008).

1014 22. A. Reversat, F. Gaertner, J. Merrin, J. Stopp, S. Tasciyan, J. Aguilera, I. de Vries, R. Hauschild,
1015 M. Hons, M. Piel, A. Callan-Jones, R. Voituriez, M. Sixt, Cellular locomotion using
1016 environmental topography. *Nature* **582**, 582–585 (2020).

1017 23. Y. I. Wu, D. Frey, O. I. Lungu, A. Jaehrig, I. Schlichting, B. Kuhlman, K. M. Hahn, A genetically
1018 encoded photoactivatable Rac controls the motility of living cells. *Nature* **461**, 104–108
1019 (2009).

1020 24. B. Lin, W. R. Holmes, C. J. Wang, T. Ueno, A. Harwell, L. Edelstein-Keshet, T. Inoue, A.
1021 Levchenko, Synthetic spatially graded Rac activation drives cell polarization and movement.
1022 *Proceedings of the National Academy of Sciences of the United States of America* **109** (2012).

1023 25. S. Nanda, A. Calderon, A. Sachan, T.-T. Duong, J. Koch, X. Xin, D. Solouk-Stahlberg, Y.-W. Wu,
1024 P. Nalbant, L. Dehmelt, Rho GTPase activity crosstalk mediated by Arhgef11 and Arhgef12
1025 coordinates cell protrusion-retraction cycles. *Nat Commun* **14**, 8356 (2023).

1026 26. L. A. Cameron, M. J. Footer, A. Van Oudenaarden, J. A. Theriot, Motility of ActA protein-
1027 coated microspheres driven by actin polymerization. *Proceedings of the National Academy*
1028 *of Sciences of the United States of America* **96**, 4908–4913 (1999).

1029 27. T. P. Loisel, R. Boujemaa, D. Pantaloni, M. Carlier, Reconstitution of actin-based motility of
1030 Listeria and Shigella using pure proteins. **401**, 613–616 (1999).

1031 28. A. Bernheim-Groswasser, S. Wiesner, R. M. Golsteyn, M.-F. Carlier, C. Sykes, The dynamics
1032 of actin-based motility depend on surface parameters. *Nature* **417**, 308–311 (2002).

1033 29. A. Mogilner, G. Oster, Force generation by actin polymerization II: The elastic ratchet and
1034 tethered filaments. *Biophysical Journal* **84**, 1591–1605 (2003).

1035 30. S. Wiesner, E. Helfer, D. Didry, G. Ducouret, F. Lafuma, M. F. Carlier, D. Pantaloni, A
1036 biomimetic motility assay provides insight into the mechanism of actin-based motility.
1037 *Journal of Cell Biology* **160**, 387–398 (2003).

1038 31. S. Romero, C. Le Clainche, D. Didry, C. Egile, D. Pantaloni, M. F. Carlier, Formin is a
1039 processive motor that requires profilin to accelerate actin assembly and associated ATP
1040 hydrolysis. *Cell* **119**, 419–429 (2004).

1041 32. C. Co, D. T. Wong, S. Gierke, V. Chang, J. Taunton, Mechanism of Actin Network Attachment
1042 to Moving Membranes: Barbed End Capture by N-WASP WH2 Domains. *Cell* **128**, 901–913
1043 (2007).

1044 33. O. Akin, R. D. Mullins, Capping Protein Increases the Rate of Actin-BasedMotility by
1045 Promoting Filament Nucleation by the Arp2/3 Complex. *Cell* **133**, 841–851 (2008).

1046 34. J. Prost, J.-F. Joanny, P. Lenz, C. Sykes, "The Physics Of Listeria Propulsion" in *Cell Motility*
1047 (Springer New York, New York, NY, 2008; https://doi.org/10.1007/978-0-387-73050-9_1),
1048 pp. 1–30.

1049 35. P. Bieling, S. D. Hansen, O. Akin, T.-D. Li, C. C. Hayden, D. A. Fletcher, R. D. Mullins, WH2 and
1050 proline-rich domains of WASP-family proteins collaborate to accelerate actin filament
1051 elongation. *EMBO J* **37**, 102–121 (2018).

1052 36. S. Razavi, T. Inoue, "Chapter 22 - Reconstitution of membrane symmetry breaking" in
1053 *Plasma Membrane Shaping*, S. Suetsugu, Ed. (Academic Press, 2023;
1054 https://www.sciencedirect.com/science/article/pii/B9780323899116000273), pp. 333–353.

1055 37. R. Lopes Dos Santos, C. Campillo, Studying actin-induced cell shape changes using Giant
1056 Unilamellar Vesicles and reconstituted actin networks. *Biochemical Society Transactions* **50**,
1057 1527–1539 (2022).

1058 38. F. C. Keber, E. Loiseau, T. Sanchez, S. J. DeCamp, L. Giomi, M. J. Bowick, M. C. Marchetti, Z.
1059 Dogic, A. R. Bausch, Topology and dynamics of active nematic vesicles. *Science* **345**, 1135–
1060 1139 (2014).

1061 39. Y. Sato, Y. Hiratsuka, I. Kawamata, S. Murata, S. M. Nomura, Micrometer-sized molecular
1062 robot changes its shape in response to signal molecules. *Science Robotics* **2**, eaal3735
1063 (2017).

1064 40. K. Gavriljuk, B. Scocozza, F. Ghasemalizadeh, H. Seidel, A. P. Nandan, M. Campos-Medina, M.
1065 Schmick, A. Koseska, P. I. H. Bastiaens, A self-organized synthetic morphogenic liposome
1066 responds with shape changes to local light cues. *Nature Communications* **12**, 1548 (2021).

1067 41. J. D. Cortese, B. Schwab, C. Frieden, E. L. Elson, Actin polymerization induces a shape
1068 change in actin-containing vesicles. *Proceedings of the National Academy of Sciences of the*
1069 *United States of America* **86**, 5773–5777 (1989).

1070 42. H. Miyata, H. Hotani, Morphological changes in liposomes caused by polymerization of
1071 encapsulated actin and spontaneous formation of actin bundles. *Proceedings of the*
1072 *National Academy of Sciences of the United States of America* **89**, 11547–11551 (1992).

1073 43. H. Miyata, S. Nishiyama, K. -i. Akashi, K. Kinosita, Protrusive growth from giant liposomes
1074 driven by actin polymerization. *Proceedings of the National Academy of Sciences* **96**, 2048–
1075 2053 (1999).

1076 44. M. Honda, K. Takiguchi, S. Ishikawa, H. Hotani, Morphogenesis of liposomes encapsulating
1077 actin depends on the type of actin-crosslinking. *Journal of Molecular Biology* **287**, 293–300
1078 (1999).

1079 45. L. L. Pontani, J. Van Der Gucht, G. Salbreux, J. Heuvingh, J. F. Joanny, C. Sykes,
1080 Reconstitution of an actin cortex inside a liposome. *Biophysical Journal* **96**, 192–198 (2009).

1081 46. K. Dürre, F. C. Keber, P. Bleicher, F. Brauns, C. J. Cyron, J. Faix, A. R. Bausch, Capping protein-
1082 controlled actin polymerization shapes lipid membranes. *Nature Communications*, doi:
1083 10.1038/s41467-018-03918-1 (2018).

1084 47. Y. Bashirzadeh, S. A. Redford, C. Lorpaiboon, A. Groaz, H. Moghimianavval, T. Litschel, P.
1085 Schwille, G. M. Hocky, A. R. Dinner, A. P. Liu, Actin crosslinker competition and sorting drive
1086 emergent GUV size-dependent actin network architecture. *Commun Biol* **4**, 1136 (2021).

1087 48. N. H. Wubshet, Y. Bashirzadeh, A. P. Liu, Fascin-induced actin protrusions are suppressed by
1088 dendritic networks in giant unilamellar vesicles. *MBoC* **32**, 1634–1640 (2021).

1089 49. T. Litschel, C. F. Kelley, D. Holz, M. Adeli Koudehi, S. K. Vogel, L. Burbaum, N. Mizuno, D.
1090 Vavylonis, P. Schwille, Reconstitution of contractile actomyosin rings in vesicles. *Nature*
1091 *Communications* **12**, 2254 (2021).

1092 50. R. Sakamoto, M. P. Murrell, Composite branched and linear F-actin maximize myosin-
1093 induced membrane shape changes in a biomimetic cell model. *Commun Biol* **7**, 1–12 (2024).

1094 51. R. Sakamoto, D. S. Banerjee, V. Yadav, S. Chen, M. L. Gardel, C. Sykes, S. Banerjee, M. P.
1095 Murrell, Membrane tension induces F-actin reorganization and flow in a biomimetic model
1096 cortex. *Commun Biol* **6**, 325 (2023).

1097 52. K. Y. Lee, S. J. Park, K. A. Lee, S. H. Kim, H. Kim, Y. Meroz, L. Mahadevan, K. H. Jung, T. K. Ahn,
1098 K. K. Parker, K. Shin, Photosynthetic artificial organelles sustain and control ATP-dependent
1099 reactions in a protocellular system. *Nature Biotechnology* **36**, 530–535 (2018).

1100 53. S. Tanaka, K. Takiguchi, M. Hayashi, Repetitive stretching of giant liposomes utilizing the
1101 nematic alignment of confined actin. *Communications Physics* **1** (2018).

1102 54. A. Fink, C. R. Doll, A. Yagüe Relimpio, Y. Dreher, J. P. Spatz, K. Göpfrich, E. A. Cavalcanti-
1103 Adam, Extracellular Cues Govern Shape and Cytoskeletal Organization in Giant Unilamellar
1104 Lipid Vesicles. *ACS Synth. Biol.*, acssynbio.2c00516 (2023).

1105 55. S. Razavi, F. Wong, B. Abubaker-Sharif, H. T. Matsubayashi, H. Nakamura, N. T. H. Nguyen, D.
1106 N. Robinson, B. Chen, P. A. Iglesias, T. Inoue, Synthetic control of actin polymerization and
1107 symmetry breaking in active protocells. *Sci Adv* **10**, eadk9731 (2024).

1108 56. K. Zhang, B. Cui, Optogenetic control of intracellular signaling pathways. *Trends in*
1109 *Biotechnology* **33**, 92–100 (2015).

1110 57. A. Pudasaini, K. K. El-Arab, B. D. Zoltowski, LOV-based optogenetic devices: Light-driven
1111 modules to impart photoregulated control of cellular signaling. *Frontiers in Molecular*
1112 *Biosciences* **2**, 1–15 (2015).

1113 58. J. Niu, M. Ben Johny, I. E. Dick, T. Inoue, Following Optogenetic Dimerizers and Quantitative
1114 Prospects. *Biophysical Journal* **111**, 1132–1140 (2016).

1115 59. G. Guntas, R. A. Hallett, S. P. Zimmerman, T. Williams, H. Yumerefendi, J. E. Bear, B.
1116 Kuhlman, Engineering an improved light-induced dimer (iLID) for controlling the localization
1117 and activity of signaling proteins. *Proceedings of the National Academy of Sciences of the*
1118 *United States of America* **112**, 112–117 (2015).

1119 60. A. Uyeda, T. Watanabe, T. Hohsaka, T. Matsuura, Different protein localizations on the inner
1120 and outer leaflet of cell-sized liposomes using cell-free protein synthesis. *Synthetic Biology* **3**,
1121 ysy007 (2018).

1122 61. A. K. Rudd, J. M. Valls Cuevas, N. K. Devaraj, SNAP-Tag-Reactive Lipid Anchors Enable
1123 Targeted and Spatiotemporally Controlled Localization of Proteins to Phospholipid
1124 Membranes. *J. Am. Chem. Soc.* **137**, 4884–4887 (2015).

1125 62. D. Scherfeld, N. Kahya, P. Schwille, Lipid dynamics and domain formation in model
1126 membranes composed of ternary mixtures of unsaturated and saturated
1127 phosphatidylcholines and cholesterol. *Biophysical journal* **85**, 3758–3768 (2003).

1128 63. F. A. Thomas, I. Visco, Z. Petrášek, F. Heinemann, P. Schwille, Diffusion coefficients and
1129 dissociation constants of enhanced green fluorescent protein binding to free standing
1130 membranes. *Data in Brief* **5**, 537–541 (2015).

1131 64. M. Frick, K. Schmidt, B. J. Nichols, Modulation of Lateral Diffusion in the Plasma Membrane
1132 by Protein Density. *Current Biology* **17**, 462–467 (2007).

1133 65. R. D. Mullins, P. Bieling, D. A. Fletcher, From solution to surface to filament: actin flux into
1134 branched networks. *Biophys Rev* **10**, 1537–1551 (2018).

1135 66. L. B. Case, X. Zhang, J. A. Ditlev, M. K. Rosen, Stoichiometry controls activity of phase-
1136 separated clusters of actin signaling proteins. *Science* **363**, 1093–1097 (2019).

1137 67. H. Miki, K. Miura, T. Takenawa, N-WASP, a novel actin-depolymerizing protein, regulates
1138 the cortical cytoskeletal rearrangement in a PIP2-dependent manner downstream of
1139 tyrosine kinases. *The EMBO Journal* **15**, 5326–5335 (1996).

1140 68. R. Rohatgi, L. Ma, H. Miki, M. Lopez, T. Kirchhausen, T. Takenawa, M. W. Kirschner, The
1141 Interaction between N-WASP and the Arp2/3 Complex Links Cdc42-Dependent Signals to
1142 Actin Assembly. *Cell* **97**, 221–231 (1999).

1143 69. O. D. Weiner, G. Servant, M. D. Welch, T. J. Mitchison, J. W. Sedat, H. R. Bourne, Spatial
1144 control of actin polymerization during neutrophil chemotaxis. *Nature Cell Biology* **1**, 75–81
1145 (1999).

1146 70. O. D. Weiner, M. C. Rentel, A. Ott, G. E. Brown, M. Jedrychowski, M. B. Yaffe, S. P. Gygi, L. C.
1147 Cantley, H. R. Bourne, M. W. Kirschner, Hem-1 Complexes Are Essential for Rac Activation,
1148 Actin Polymerization, and Myosin Regulation during Neutrophil Chemotaxis. *PLoS Biol* **4**,
1149 e38 (2006).

1150 71. A. Kawska, K. Carvalho, J. Manzi, R. Boujemaa-Paterski, L. Blanchoin, J.-L. Martiel, C. Sykes,
1151 How actin network dynamics control the onset of actin-based motility. *Proceedings of the*
1152 *National Academy of Sciences* **109**, 14440–14445 (2012).

1153 72. K. B. Velle, L. K. Fritz-Laylin, Diversity and evolution of actin-dependent phenotypes. *Current*
1154 *Opinion in Genetics and Development* **58–59**, 40–48 (2019).

1155 73. E. D. Goley, M. D. Welch, The ARP2/3 complex: An actin nucleator comes of age. *Nature*
1156 *Reviews Molecular Cell Biology* **7**, 713–726 (2006).

1157 74. D. A. Valencia, M. E. Quinlan, Formins. *Current Biology* **31**, R517–R522 (2021).

1158 75. D. R. Kovar, E. S. Harris, R. Mahaffy, H. N. Higgs, T. D. Pollard, Control of the Assembly of
1159 ATP- and ADP-Actin by Formins and Profilin. *Cell* **124**, 423–435 (2006).

1160 76. J. Funk, F. Merino, L. Venkova, L. Heydenreich, J. Kierfeld, P. Vargas, S. Raunser, M. Piel, P.
1161 Bieling, Profilin and formin constitute a pacemaker system for robust actin filament growth.
1162 *eLife* **8**, e50963 (2019).

1163 77. S. Dmitrieff, F. Nédélec, Amplification of actin polymerization forces. *Journal of Cell Biology*
1164 **212**, 763–766 (2016).

1165 78. H. Nakamura, E. Rho, C. T. Lee, K. Itoh, D. Deng, S. Watanabe, S. Razavi, H. T. Matsubayashi,
1166 C. Zhu, E. Jung, P. Rangamani, S. Watanabe, T. Inoue, ActuAtor, a Listeria-inspired molecular
1167 tool for physical manipulation of intracellular organizations through de novo actin
1168 polymerization. *Cell Reports* **42**, 113089 (2023).

1169 79. R. DeRose, T. Miyamoto, T. Inoue, Manipulating signaling at will: chemically-inducible
1170 dimerization (CID) techniques resolve problems in cell biology. *Pflugers Archiv : European*
1171 *journal of physiology* **465**, 409–417 (2013).

1172 80. W. Luo, Z. Z. Lieu, E. Manser, A. D. Bershadsky, M. P. Sheetz, Formin DAAM1 organizes actin
1173 filaments in the cytoplasmic nodal actin network. *PLoS ONE* **11**, 1–22 (2016).

1174 81. K. M. C. Chan, A. L. Arthur, J. Morstein, M. Jin, A. Bhat, D. Schlesinger, S. Son, D. A. Stevens,
1175 D. G. Drubin, D. A. Fletcher, Evolutionarily related small viral fusogens hijack distinct but
1176 modular actin nucleation pathways to drive cell-cell fusion. *Proc Natl Acad Sci USA* **118**,
1177 e2007526118 (2021).

1178 82. A. Drazic, H. Aksnes, M. Marie, M. Boczkowska, S. Varland, E. Timmerman, H. Foyn, N.
1179 Glomnes, G. Rebowski, F. Impens, K. Gevaert, R. Dominguez, T. Arnesen, NAA80 is actin's N-
1180 terminal acetyltransferase and regulates cytoskeleton assembly and cell motility.
1181 *Proceedings of the National Academy of Sciences* **115**, 4399–4404 (2018).

1182 83. J. Block, D. Breitsprecher, S. Kühn, M. Winterhoff, F. Kage, R. Geffers, P. Duwe, J. L. Rohn, B.
1183 Baum, C. Brakebusch, M. Geyer, T. E. B. Stradal, J. Faix, K. Rottner, FMNL2 Drives Actin-
1184 Based Protrusion and Migration Downstream of Cdc42. *Current Biology* **22**, 1005–1012
1185 (2012).

1186 84. A. Schirenbeck, R. Arasada, T. Bretschneider, M. Schleicher, J. Faix, Formins and VASPs may
1187 co-operate in the formation of filopodia. *Biochemical Society Transactions* **33**, 4 (2005).

1188 85. H. Mizuno, C. Higashida, Y. Yuan, T. Ishizaki, S. Narumiya, N. Watanabe, Rotational
1189 movement of the formin mDia1 along the double helical strand of an actin filament. *Science*
1190 **331**, 80–83 (2011).

1191 86. X. Naj, A. K. Hoffmann, M. Himmel, S. Linder, The formins FMNL1 and mDia1 regulate
1192 coiling phagocytosis of borrelia burgdorferi by primary human macrophages. *Infection and*
1193 *Immunity* **81**, 1683–1695 (2013).

1194 87. C. J. Gould, S. Maiti, A. Michelot, B. R. Graziano, L. Blanchoin, B. L. Goode, The formin DAD
1195 domain plays dual roles in autoinhibition and actin nucleation. *Current Biology* **21**, 384–390
1196 (2011).

1197 88. M. P. Murrell, R. Voituriez, J.-F. Joanny, P. Nassoy, C. Sykes, M. L. Gardel, Liposome
1198 adhesion generates traction stress. *Nature Phys* **10**, 163–169 (2014).

1199 89. A. Colin, T. Kotila, C. Guérin, M. Orhant-Prioux, B. Vianay, A. Mogilner, P. Lappalainen, M.
1200 Théry, L. Blanchoin, Recycling of the actin monomer pool limits the lifetime of network
1201 turnover. *The EMBO Journal* **42**, e112717 (2023).

1202 90. D. Sakata, H. Taniguchi, S. Yasuda, A. Adachi-Morishima, Y. Hamazaki, R. Nakayama, T. Miki,
1203 N. Minato, S. Narumiya, Impaired T lymphocyte trafficking in mice deficient in an actin-
1204 nucleating protein, mDia1. *Journal of Experimental Medicine* **204**, 2031–2038 (2007).

1205 91. C. Yang, L. Czech, S. Gerboth, S. Kojima, G. Scita, T. Svitkina, Novel Roles of Formin mDia2 in
1206 Lamellipodia and Filopodia Formation in Motile Cells. *PLoS Biol* **5**, e317 (2007).

1207 92. Y. Shi, J. Zhang, M. Mullin, B. Dong, A. S. Alberts, K. A. Siminovitch, The mDial Formin Is
1208 Required for Neutrophil Polarization, Migration, and Activation of the LARG/RhoA/ROCK
1209 Signaling Axis during Chemotaxis. *The Journal of Immunology* **182**, 3837–3845 (2009).

1210 93. T. Isogai, R. van der Kammen, D. Leyton-Puig, K. M. Kedziora, K. Jalink, M. Innocenti,
1211 Initiation of lamellipodia and ruffles involves cooperation between mDia1 and the Arp2/3
1212 complex. *Journal of Cell Science*, jcs.176768 (2015).

1213 94. P. Monzo, Y. K. Chong, C. Guetta-Terrier, A. Krishnasamy, S. R. Sathe, E. K. F. Yim, W. H. Ng,
1214 B. T. Ang, C. Tang, B. Ladoux, N. C. Gauthier, M. P. Sheetz, Mechanical confinement triggers
1215 glioma linear migration dependent on formin FHOD3. *MBoC* **27**, 1246–1261 (2016).

1216 95. F. Kage, M. Winterhoff, V. Dimchev, J. Mueller, T. Thalheim, A. Freise, S. Brühmann, J.
1217 Kollasser, J. Block, G. Dimchev, M. Geyer, H.-J. Schnittler, C. Brakebusch, T. E. B. Stradal, M.-
1218 F. Carlier, M. Sixt, J. Käs, J. Faix, K. Rottner, FMNL formins boost lamellipodial force
1219 generation. *Nat Commun* **8**, 14832 (2017).

1220 96. Y. Yamazaki, Y. Miyata, K. Morigaki, M. Miyazaki, Controlling Physical and Biochemical
1221 Parameters of Actin Nucleation Using a Patterned Model Lipid Membrane. *Nano Lett.* **24**,
1222 1825–1834 (2024).

1223 97. M. Abercrombie, J. E. M. Heaysman, S. M. Pegrum, The locomotion of fibroblasts in culture I.
1224 Movements of the leading edge. *Experimental Cell Research* **59**, 393–398 (1970).

1225 98. P. Maiuri, E. Terriac, P. Paul-Gilloteaux, T. Vignaud, K. McNally, J. Onuffer, K. Thorn, P. A.
1226 Nguyen, N. Georgoulia, D. Soong, A. Jayo, N. Beil, J. Beneke, J. C. Hong Lim, C. Pei-Ying Sim,
1227 Y.-S. Chu, A. Jiménez-Dalmaroni, J.-F. Joanny, J.-P. Thiery, H. Erfle, M. Parsons, T. J.
1228 Mitchison, W. A. Lim, A.-M. Lennon-Duménil, M. Piel, M. Théry, The first World Cell Race.
1229 *Current Biology* **22**, R673–R675 (2012).

1230 99. S. A. Koestler, K. Rottner, F. Lai, J. Block, M. Vinzenz, J. V. Small, F- and G-Actin
1231 Concentrations in Lamellipodia of Moving Cells. *PLoS ONE* **4**, e4810 (2009).

1232 100. S. Samarin, S. Romero, C. Kocks, D. Didry, D. Pantaloni, M. F. Carlier, How VASP
1233 enhances actin-based motility. *Journal of Cell Biology* **163**, 131–142 (2003).

1234 101. W. M. Brieher, M. Coughlin, T. J. Mitchison, Fascin-mediated propulsion of Listeria
1235 monocytogenes independent of frequent nucleation by the Arp2/3 complex. *Journal of Cell*
1236 *Biology* **165**, 233–242 (2004).

1237 102. P. Li, S. Banjade, H. C. Cheng, S. Kim, B. Chen, L. Guo, M. Llaguno, J. V. Hollingsworth, D.
1238 S. King, S. F. Banani, P. S. Russo, Q. X. Jiang, B. T. Nixon, M. K. Rosen, Phase transitions in the
1239 assembly of multivalent signalling proteins. *Nature* **483**, 336–340 (2012).

1240 103. C. Simon, R. Kusters, V. Caorsi, A. Allard, M. Abou-Ghali, J. Manzi, A. Di Cicco, D. Lévy, M.
1241 Lenz, J.-F. Joanny, C. Campillo, J. Plastino, P. Sens, C. Sykes, Actin dynamics drive cell-like
1242 membrane deformation. *Nature Physics* **15**, 602–609 (2019).

1243 104. P. DiMilla, J. Stone, J. Quinn, S. Albelda, D. Lauffenburger, Maximal migration of human
1244 smooth muscle cells on fibronectin and type IV collagen occurs at an intermediate
1245 attachment strength. *Journal of Cell Biology* **122**, 729–737 (1993).

1246 105. C. Schreiber, B. Amiri, J. C. J. Heyn, J. O. Rädler, M. Falcke, On the adhesion–velocity
1247 relation and length adaptation of motile cells on stepped fibronectin lanes. *Proc. Natl. Acad.*
1248 *Sci. U.S.A.* **118**, e2009959118 (2021).

1249 106. V. Caorsi, J. Lemière, C. Campillo, M. Bussonnier, J. Manzi, T. Betz, J. Plastino, K. Carvalho,
1250 C. Sykes, Cell-sized liposome doublets reveal active tension build-up driven by acto-myosin
1251 dynamics. *Soft Matter* **12**, 6223–6231 (2016).

1252 107. W. I. Goh, K. B. Lim, T. Sudhaharan, K. P. Sem, W. Bu, A. M. Chou, S. Ahmed, mDia1 and
1253 WAVE2 Proteins Interact Directly with IRSp53 in Filopodia and Are Involved in Filopodium
1254 Formation. *Journal of Biological Chemistry* **287**, 4702–4714 (2012).

1255 108. A. Bisaria, A. Hayer, D. Garbett, D. Cohen, T. Meyer, Membrane-proximal F-actin
1256 restricts local membrane protrusions and directs cell migration. *Science* **368**, 1205–1210
1257 (2020).

1258 109. Z. Shi, Z. T. Graber, T. Baumgart, H. A. Stone, A. E. Cohen, Cell Membranes Resist Flow.
1259 *Cell* **175**, 1769-1779.e13 (2018).

1260 110. S. Gat, C. Simon, C. Campillo, A. Bernheim-Groswasser, C. Sykes, Finger-like membrane
1261 protrusions are favored by heterogeneities in the actin network. *Soft Matter* **16**, 7222–7230
1262 (2020).

1263 111. S. M. Bartelt, J. Steinkühler, R. Dimova, S. V. Wegner, Light-Guided Motility of a Minimal
1264 Synthetic Cell. *Nano Lett.* **18**, 7268–7274 (2018).

1265 112. L. A. Banaszynski, C. W. Liu, T. J. Wandless, Characterization of the FKBP·Rapamycin·FRB
1266 Ternary Complex. *J. Am. Chem. Soc.* **127**, 4715–4721 (2005).

1267 113. E. Rihtar, T. Lebar, D. Lainšček, K. Kores, S. Lešnik, U. Bren, R. Jerala, Chemically inducible
1268 split protein regulators for mammalian cells. *Nat Chem Biol*, doi: 10.1038/s41589-022-
1269 01136-x (2022).

1270 114. K. Yoshida, K. Abe, Y. Sato, I. Kawamata, R. J. Archer, H. T. Matsubayashi, S. Hamada, S.
1271 Murata, S. Nomura, Transmembrane DNA Sequence Signaling via Hybridization. ChemRxiv
1272 [Preprint] (2024). https://doi.org/10.26434/chemrxiv-2024-571kp.

1273 115. S. L. Veatch, S. L. Keller, Separation of Liquid Phases in Giant Vesicles of Ternary
1274 Mixtures of Phospholipids and Cholesterol. *Biophysical Journal* **85**, 3074–3083 (2003).

1275 116. T. Litschel, B. Ramm, R. Maas, M. Heymann, P. Schwille, Beating Vesicles: Encapsulated
1276 Protein Oscillations Cause Dynamic Membrane Deformations. *Angewandte Chemie*
1277 *International Edition* **57**, 16286–16290 (2018).

1278 117. S. Takada, N. Yoshinaga, N. Doi, K. Fujiwara, Controlling the Periodicity of a Reaction–
1279 Diffusion Wave in Artificial Cells by a Two-Way Energy Supplier. *ACS Nano* **16**, 16853–16861
1280 (2022).

1281 118. S. D. Hansen, W. Y. C. Huang, Y. K. Lee, P. Bieling, S. M. Christensen, J. T. Groves,
1282 Stochastic geometry sensing and polarization in a lipid kinase–phosphatase competitive
1283 reaction. *Proceedings of the National Academy of Sciences of the United States of America*
1284 **116**, 15013–15022 (2019).

1285 119. Y. Sato, M. Takinoue, Capsule-like DNA Hydrogels with Patterns Formed by Lateral Phase
1286 Separation of DNA Nanostructures. *JACS Au* **2**, 159–168 (2022).

1287 120. B. Haller, K. Jahnke, M. Weiss, K. Göpfrich, I. Platzman, J. P. Spatz, Autonomous
1288 Directional Motion of Actin-Containing Cell-Sized Droplets. *Advanced Intelligent Systems* **3**,
1289 2000190 (2021).

1290 121. R. Sakamoto, Z. Izri, Y. Shimamoto, M. Miyazaki, Y. T. Maeda, Geometric trade-off
1291 between contractile force and viscous drag determines the actomyosin-based motility of a
1292 cell-sized droplet. *Proc. Natl. Acad. Sci. U.S.A.* **119**, e2121147119 (2022).

1293 122. S. Brühmann, D. S. Ushakov, M. Winterhoff, R. B. Dickinson, U. Curth, J. Faix, Distinct
1294 VASP tetramers synergize in the processive elongation of individual actin filaments from
1295 clustered arrays. *Proc Natl Acad Sci USA* **114**, E5815–E5824 (2017).

1296 123. J. E. Tropea, S. Cherry, D. S. Waugh, "Expression and Purification of Soluble His6-Tagged
1297 TEV Protease" in *High Throughput Protein Expression and Purification: Methods and*
1298 *Protocols*, S. A. Doyle, Ed. (Humana Press, Totowa, NJ, 2009; https://doi.org/10.1007/978-1-
1299 59745-196-3_19)*Methods in Molecular Biology*, pp. 297–307.

1300 124. T. Inoue, W. D. Heo, J. S. Grimley, T. J. Wandless, T. Meyer, An inducible translocation
1301 strategy to rapidly activate and inhibit small GTPase signaling pathways. *Nature Methods* **2**,
1302 415–418 (2005).

1303 125. H. Onuma, T. Komatsu, M. Arita, K. Hanaoka, T. Ueno, T. Terai, T. Nagano, T. Inoue,
1304 Rapidly rendering cells phagocytic through a cell surface display technique and concurrent
1305 Rac activation. *Science Signaling* **7**, 1–8 (2014).

1306 126. Cytoplasmic Actin: Purification and Single Molecule Assembly Assays | SpringerLink.
1307 https://link.springer.com/protocol/10.1007/978-1-62703-538-5_9.

1308 127. L. K. Doolittle, M. K. Rosen, S. B. Padrick, Measurement and analysis of in vitro actin
1309 polymerization. *Methods in Molecular Biology*, doi: 10.1007/978-1-62703-538-5_16 (2013).

1310 128. S. Razavi, T. Inoue, T. LUO, D. Robinson, Methods for making giant vesicles and their use
1311 (2024). https://patents.google.com/patent/US11951210B2/en.

1312 129. J. Schindelin, I. Arganda-Carreras, E. Frise, V. Kaynig, M. Longair, T. Pietzsch, S. Preibisch,
1313 C. Rueden, S. Saalfeld, B. Schmid, J.-Y. Tinevez, D. J. White, V. Hartenstein, K. Eliceiri, P.
1314 Tomancak, A. Cardona, Fiji: an open-source platform for biological-image analysis. *Nature*
1315 *methods* **9**, 676–682 (2012).

1316 130. H. T. Matsubayashi, J. Mountain, N. Takahashi, A. Deb Roy, T. Yao, A. F. Peterson, C. Saez
1317 Gonzalez, I. Kawamata, T. Inoue, Non-catalytic role of phosphoinositide 3-kinase in
1318 mesenchymal cell migration through non-canonical induction of p85β/AP2-mediated
1319 endocytosis. *Nat Commun* **15**, 2612 (2024).

1320 131. L. A. Gross, G. S. Baird, R. C. Hoffman, K. K. Baldridge, R. Y. Tsien, The structure of the
1321 chromophore within DsRed, a red fluorescent protein from coral. *Proc Natl Acad Sci U S A*
1322 **97**, 11990–11995 (2000).

1323 132. V. I. Martynov, A. P. Savitsky, N. Y. Martynova, P. A. Savitsky, K. A. Lukyanov, S. A.
1324 Lukyanov, Alternative Cyclization in GFP-like Proteins Family. *Journal of Biological Chemistry*
1325 **276**, 21012–21016 (2001).

1326

Figure 1

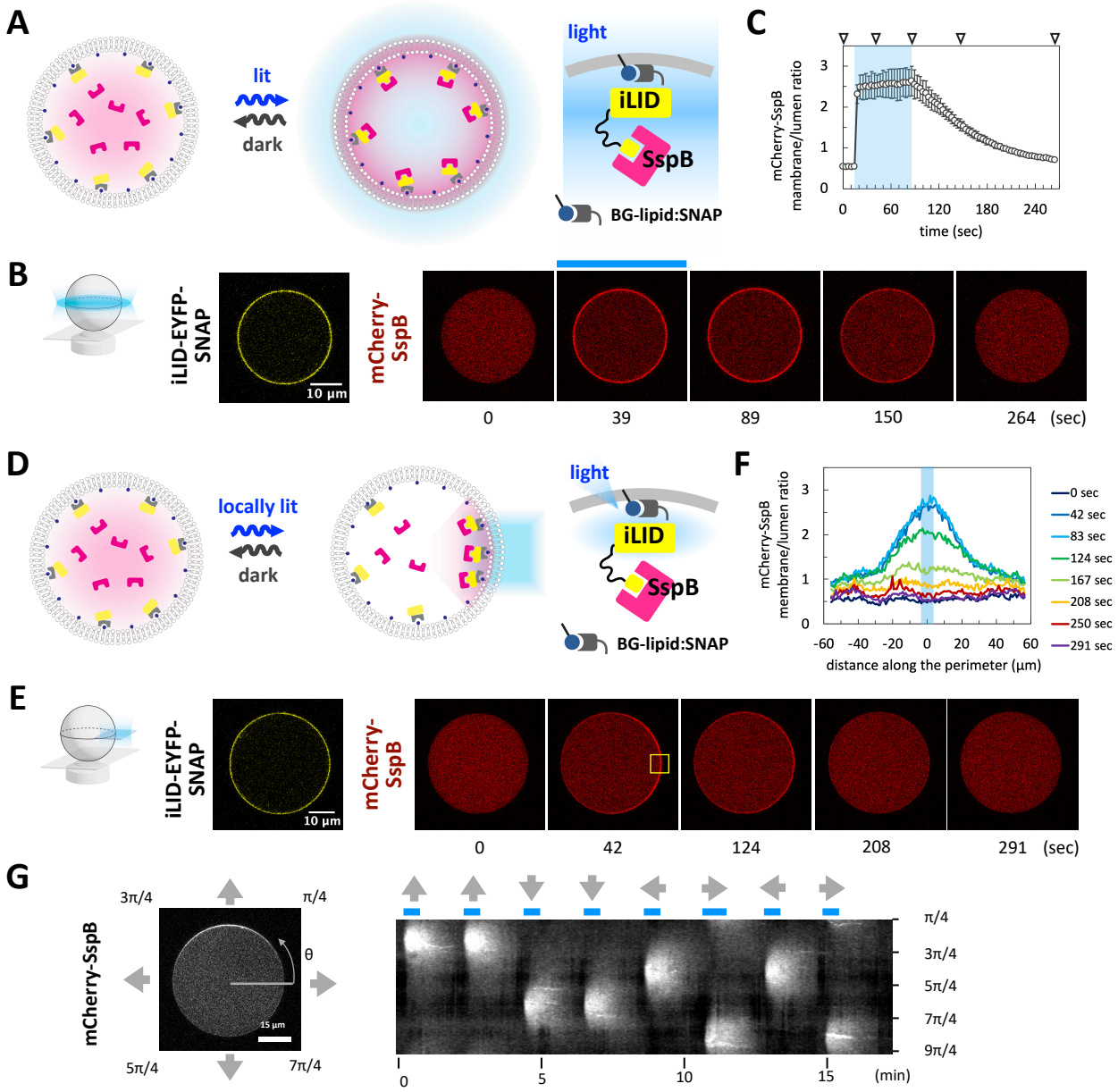

Fig. 1. Reversible and asymmetric control of protein localization with iLID-SspB within GUVs. (A) Schematic representation of iLID-SspB reaction with global light stimulation. iLID was tethered on the membrane via the interaction between SNAP-tag and bendylguanine-conjugated lipids. Upon blue light illumination, Jα helix of iLID extends to expose the binding site for SspB, whereas in the dark, iLID reverses to its closed state and releases SspB. (B) Representative images of iLID-YFP-SNAP and mCherry-SspB. Scale bar, 10 µm. Blue bar indicates the period of blue light illumination. (C) Time course of membrane/lumen ratio of mCherry-SspB signal (n=5). Error bars indicate standard deviation. Blue area indicates the period of blue light stimulation. Triangles indicate timepoints represented in (B). (D) Schematic representation of iLID-SspB reaction with local light stimulation. (E) Representative images of mCherry-SspB. Scale bar, 10 µm. Yellow box indicates the area of blue light illumination. (F) Membrane/lumen ratio of mCherry-SspB for the representative image shown. The distance is measured from the center of blue light illumination along the perimeter of the GUV. (G) Representative image and kymograph of repetitive and reversible SspB translocation. Kymograph shows membrane signal of mCherry-SspB.

Figure 2

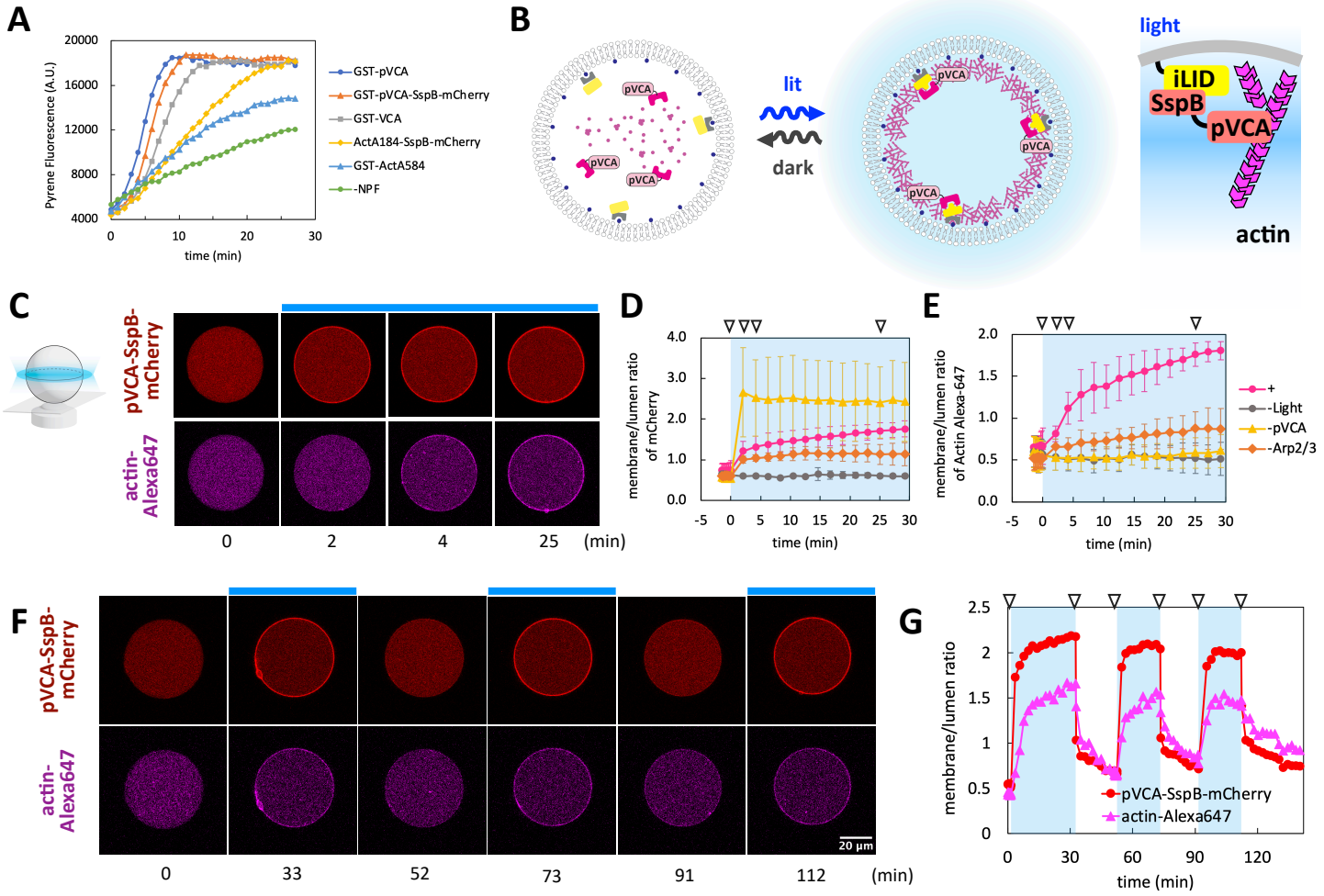

Fig. 2. Reversible light control of actin cytoskeleton within GUVs. (A) Bulk pyrene actin polymerization assay with 1 µM actin (5% pyrene labeled), 10 nM Arp2/3, and 100 nM NPFs. (-NPF) represents actin and Arp2/3 only condition. (B) Schematic representation of light inducible actin polymerization. Translocation of pVCA-SspB-mCherry increases local concentration of pVCA on the membrane and enhances actin polymerization. (C) Representative images of pVCA-SspB-mCherry and Alexa 647 actin. Blue bar indicates the period of blue light illumination. (D), (E) Time course of membrane/lumen ratio of mCherry and Alexa 647 actin. +: full set of components (n=4). -Light: no blue light stimulation (n=3). -pVCA: pVCA-SspB-mCherry was replaced with mCherry-SspB (n=4). -Arp2/3: Arp2/3 was omitted (n=4). Error bars indicate 95% CI. Triangles indicate timepoints represented in (C). (F) Representative images of reversible actin polymerization. Blue bars indicate the period of blue light illumination. (G) Time course of membrane/lumen ratio of pVCA-SspB-mCherry and Alexa 647-labeled actin in (F). Triangles indicate timepoints represented in (F).

Figure 3

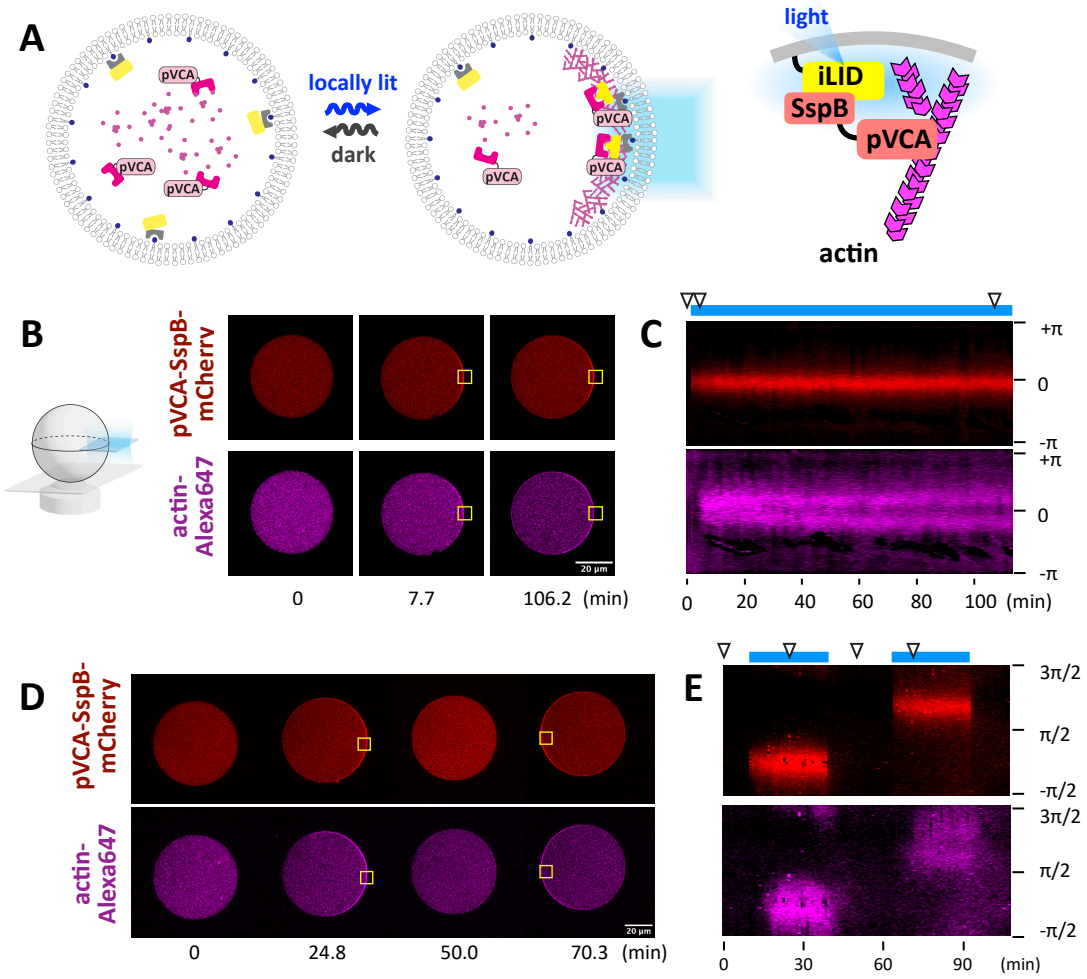

Fig. 3. Asymmetric light control of actin cytoskeleton within GUVs. (A) Schematic representation of iLID-SspB reaction with local light stimulation. (B, D) Representative images of light inducible asymmetric actin polymerization. Yellow boxes indicate the area of blue light illumination. (C, E) Kymograph of membrane pVCA-SspB and actin signals. Blue bars indicate the period of blue light illumination. Triangles indicate timepoints represented in (B, D).

Figure 4

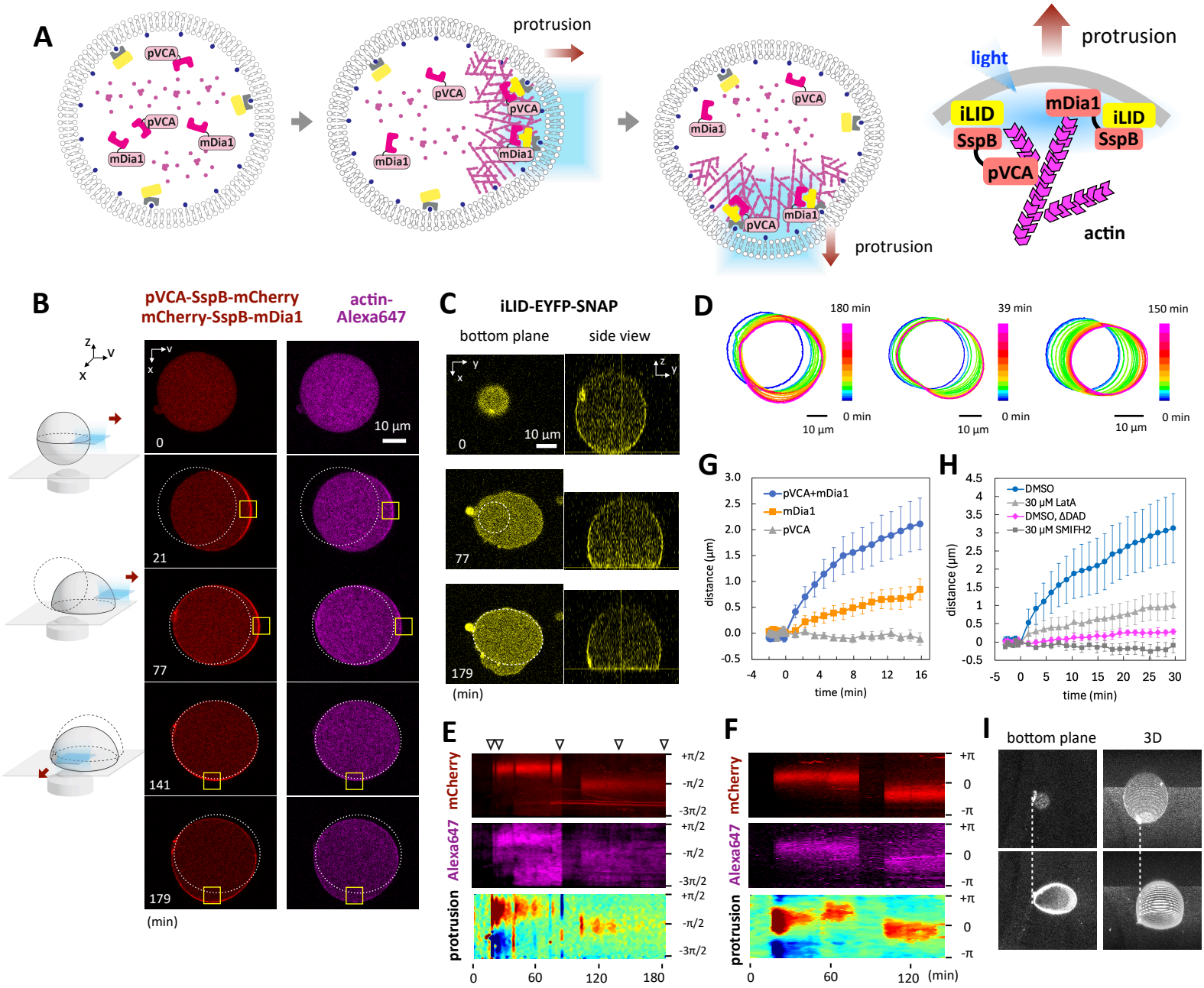

Fig. 4. mDia1-mediated actin polymerization drives protrusive motility of GUVs. (A) Schematic representation of light inducible membrane protrusion driven by pVCA and mDia1-mediated actin polymerization. (B) Representative images of pVCA-mDia1-mediated movement of GUVs. Yellow boxes indicate the area of blue light stimulation. Dotted line shows the initial position of the GUV. (C) Representative images of iLID-EYFP-SNAP showing the increase in adhesive area and vesicle deformation into dome-like shape. Bottom plane indicates the confocal plane right above the bottom substrate. Side view is reconstituted from z-stack. Dotted line shows the adhesive area of the previous images. (D) Color-coded boundaries of GUVs. The data correspond as follows. Left: Fig. 4B. Middle: Fig. S16A. Right: Fig. S16B. (E, F) Kymographs of membrane signal of mCherry and actin Alexa-647 and membrane protrusions. Triangles in (E) indicate the timepoints represented in (B, C). Data of (E) and (F) corresponds to Fig. 4 (B) and Fig. S16A, respectively. (G) Distance the front (illuminated) side of GUV membrane moved forward. pVCA+mDia1 (1 µM GST-pVCA-SspB-mCherry + 1 µM mCherry-SspB-mDia1, n=14 vesicles), mDia1 (1 µM mCherry-SspB-mDia1, n=12 vesicles), pVCA (1 µM GST-pVCA-SspB-mCherry, n=12 vesicles). Error bars indicate standard error of the mean (SEM). (H) DMSO (n=9 vesicles), 30 µM LatA (Latrunculin A) (n=10 vesicles). DMSO, ΔDAD: mCherry-SspB-mDia1 (FH1-FH2-DAD) was replaced with mCherry-SspB-mDia1(FH1-FH2) (n=13 vesicles). 30 µM SMIFH2 (n=6 vesicles). Error bars indicate standard error of the mean (SEM). (I) A GUV deformed into dome-like shape after movement. Upper images: before light stimulation. Lower images: after light stimulation. The data corresponds to Fig. S16C.

Figure S1

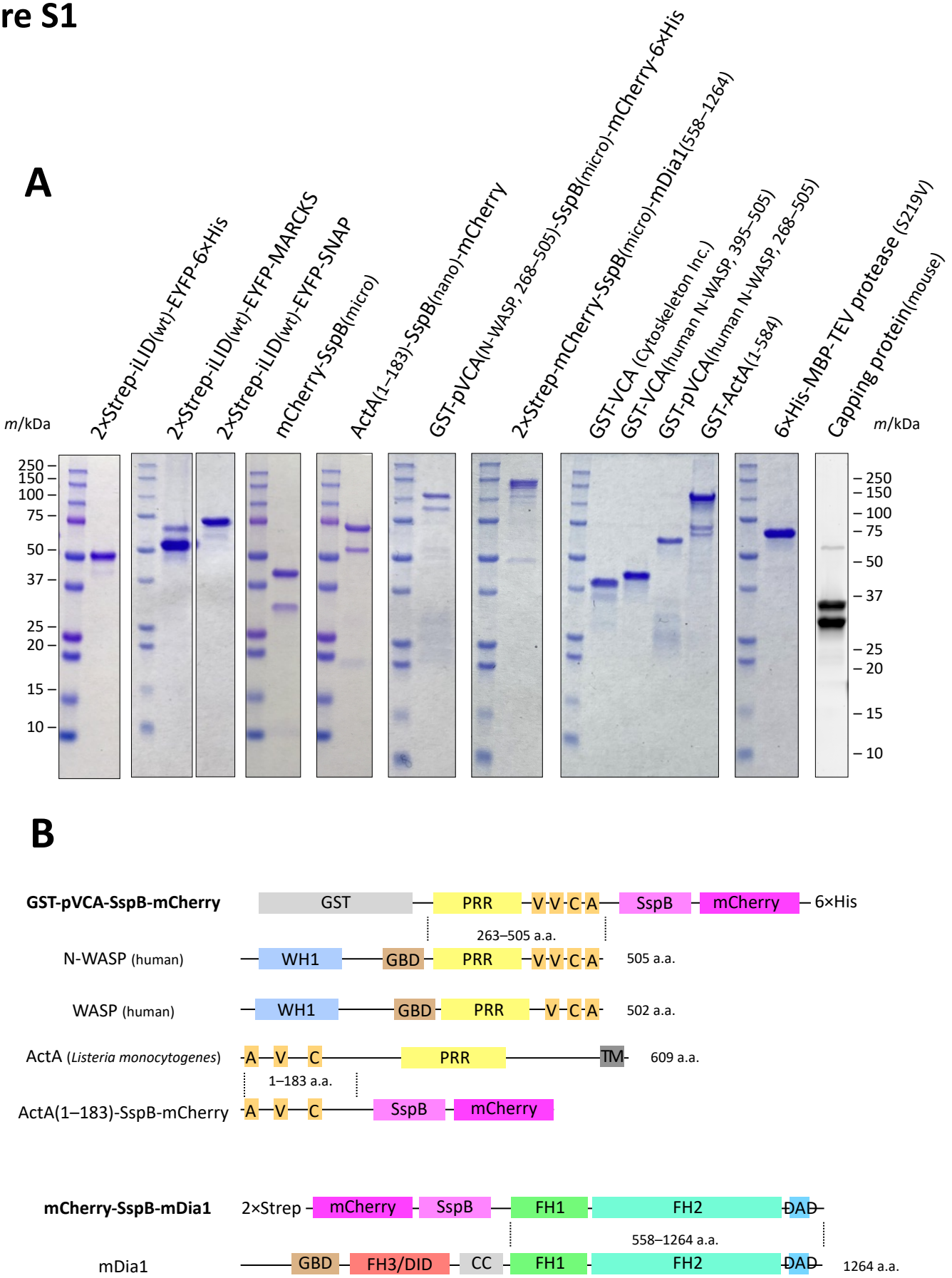

Fig. S1. Proteins purified in this study. (A) SDS-PAGE results of purified proteins. Blue: Coomassie brilliant blue staining. Gray: SYPRO Ruby staining. Most mCherry-tagged proteins show two extra bands due to a known chromophore cleavage reaction during the boiling process (131, 132). (B) Domain structures of NPFs used in this study.

Figure S2

A

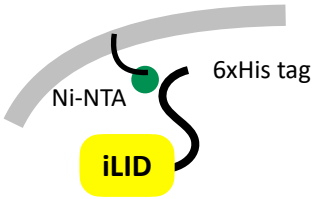

B

5 mol% NI-NTA-DGS/0–2 mol% PEG2000-PE/
93-95 mol% POPC

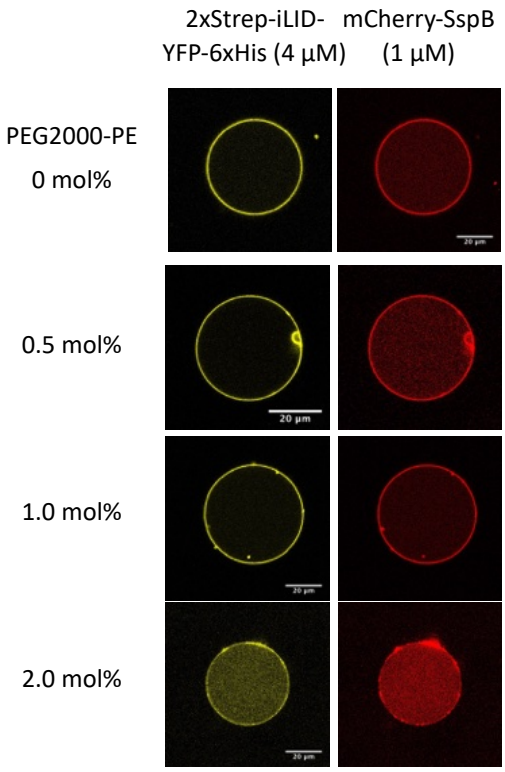

C

5 mol% Ni-NTA-DGS/95 mol% POPC

mCherry-SspB (1 µM)

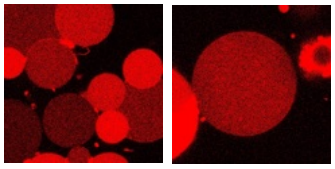

D

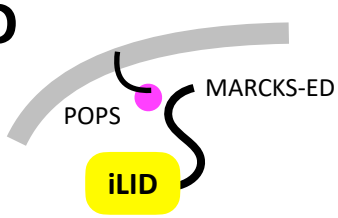

E

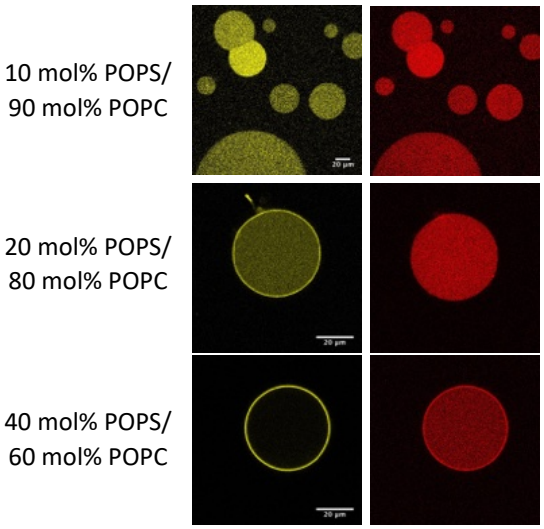

F

40 mol% POPS/58–60 mol% POPC

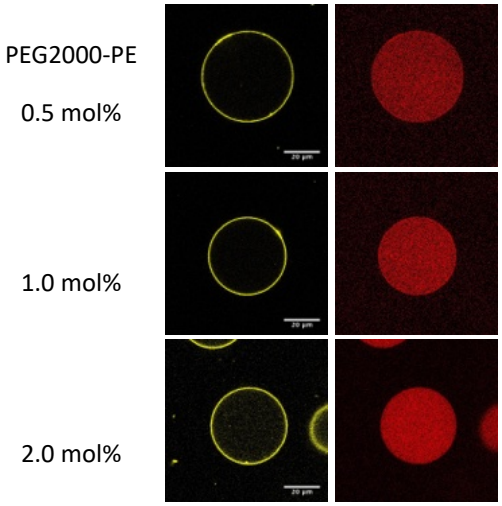

Figure S2

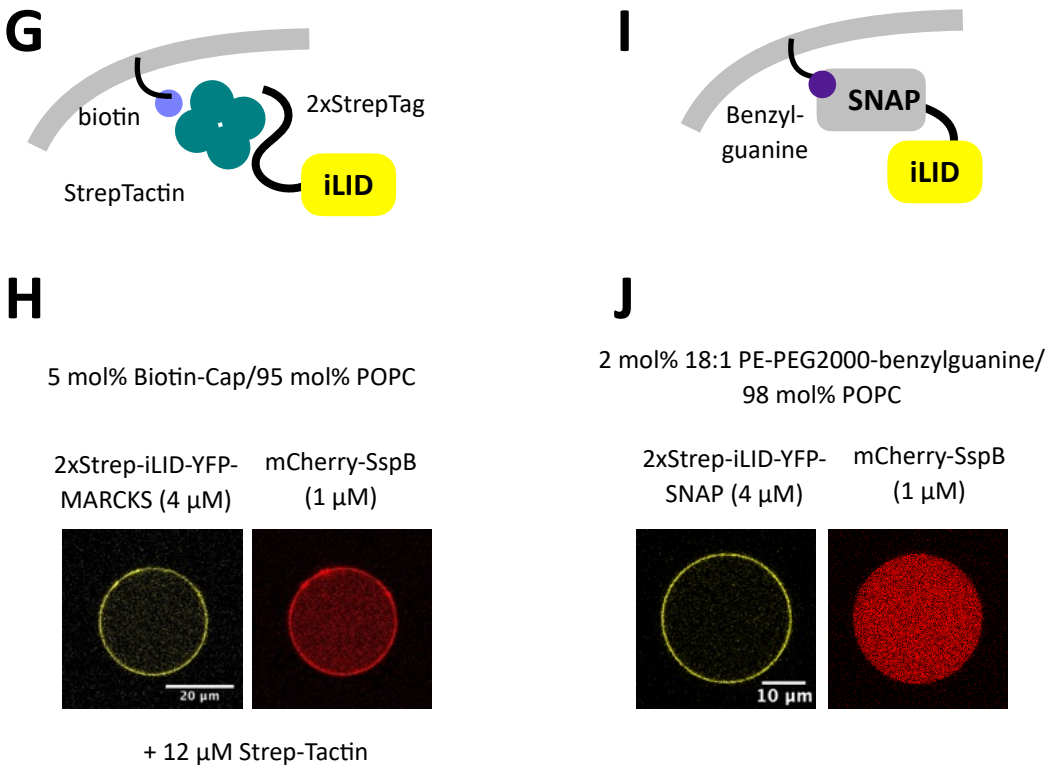

Fig. S2. Optimization of membrane anchoring of iLID. (A),(D),(G),(I): Schematic representations of membrane anchoring of iLID. (B),(C),(E),(F),(H),(J): Confocal images of iLID variants and mCherry-SspB. (B) His-tag Ni-NTA pair caused non-specific membrane recruitment of SspB. This is possibly caused by the presence of 2×Strep-iLID-YFP-6×His because mCherry-SspB itself did not show non-specific binding to the membrane of 5%Ni-NTA DGS/95%POPC (C). (E),(F) MARCKS-ED peptide requires high percentage of PS and PEGylated-lipids to reduce non-specific binding of SspB. (H) Biotin-StrepTactin-Streptag also caused non-specific membrane binding of SspB. (J) The data correspond with Fig. 1B.

Figure S3

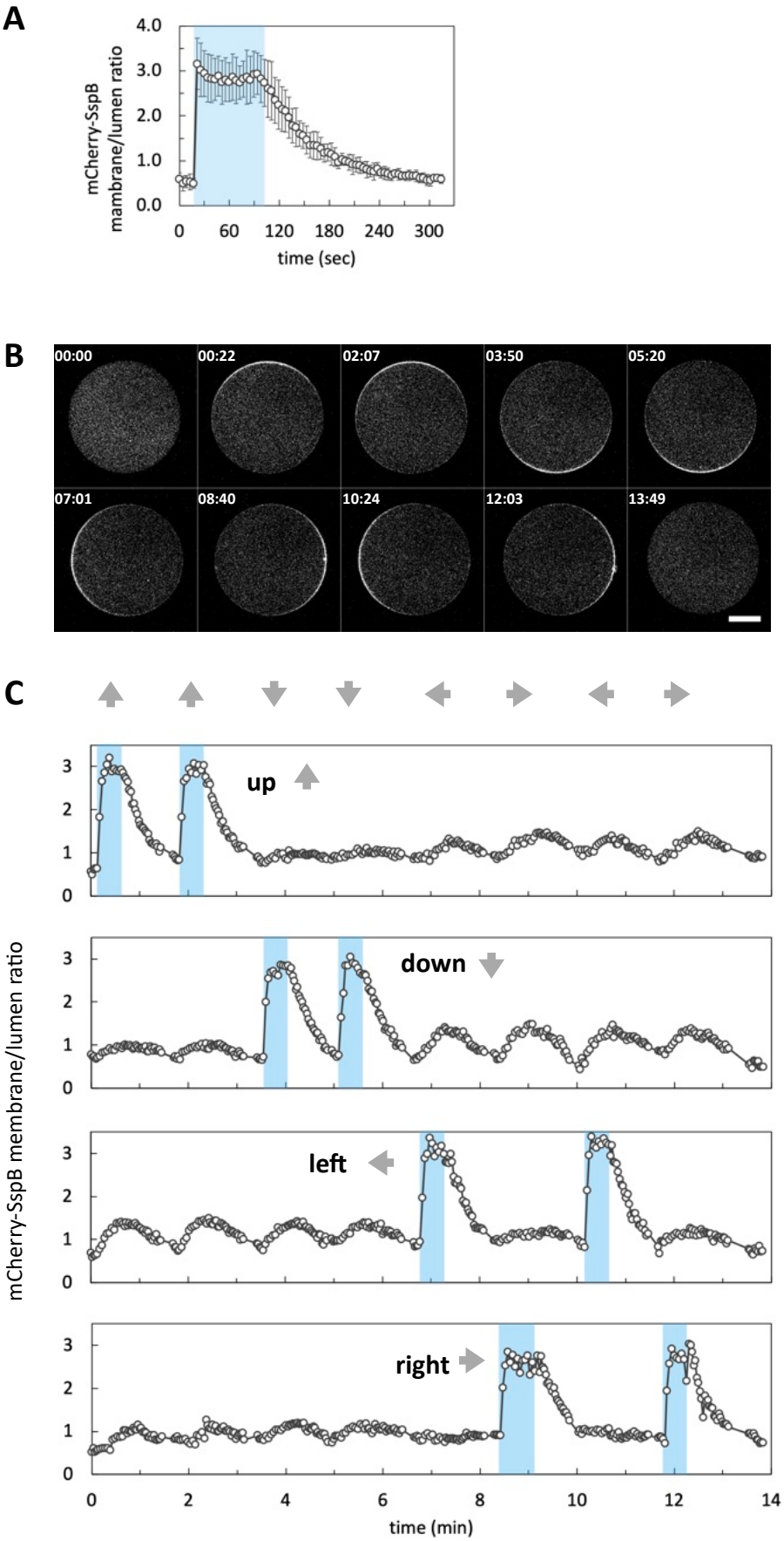

Fig. S3. Asymmetric control of protein localization with iLID-SspB within GUVs. (A) Time course of membrane/lumen ratio of mCherry-SspB signal in the illuminated area (n=5). Error bars indicate 95% CI. Blue area indicates the time window of blue light stimulation. The data corresponds to Fig. 1E and F. (B, C) Confocal images and time course of membrane/lumen ratio of mCherry-SspB signal responding to repetitive local light illuminations. The data corresponds to Fig. 1G.

Figure S4

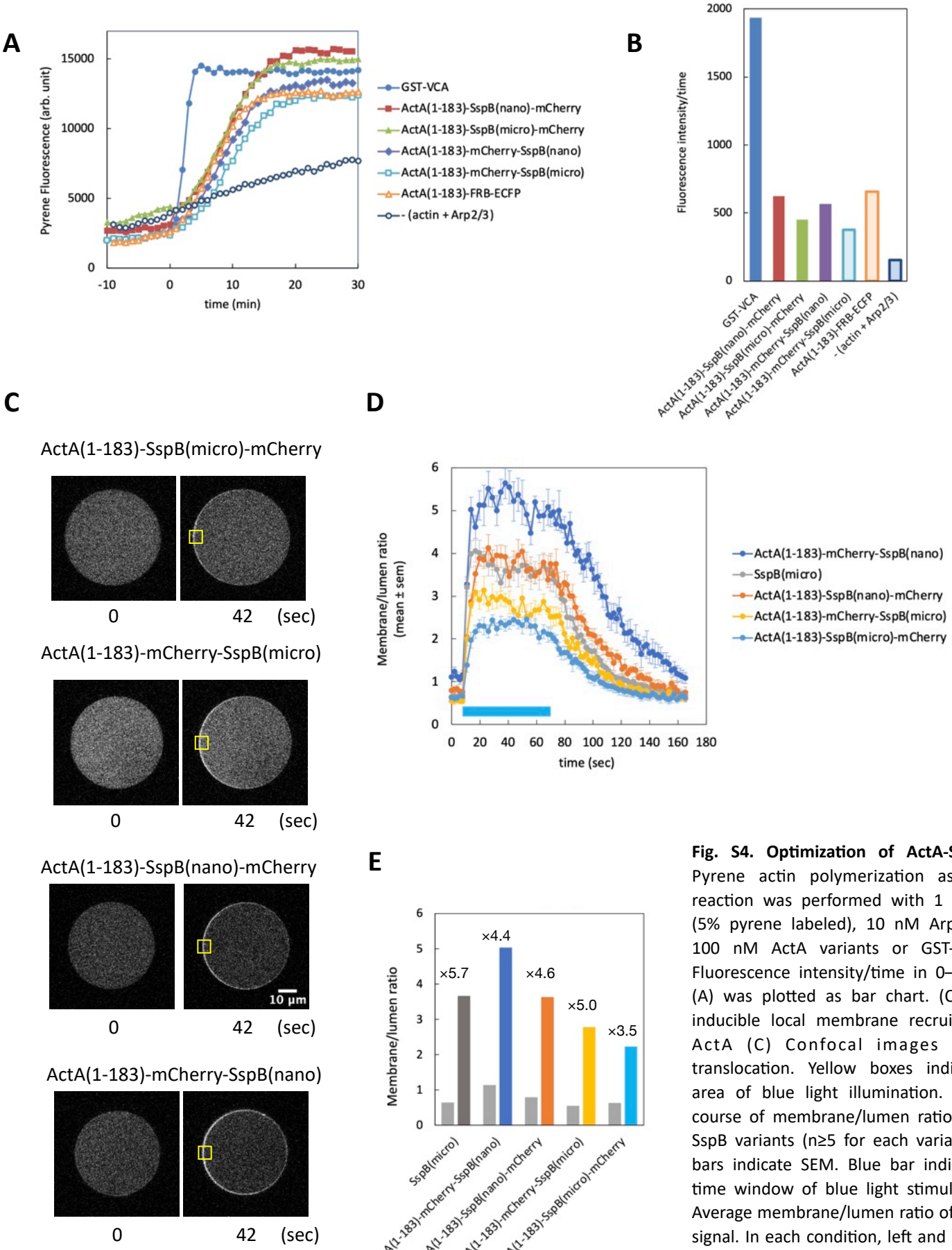

Fig. S4. Optimization of ActA-SspB. (A) Pyrene actin polymerization assay. The reaction was performed with 1 µM actin (5% pyrene labeled), 10 nM Arp2/3, and 100 nM ActA variants or GST-VCA. (B) Fluorescence intensity/time in 0–6 min of (A) was plotted as bar chart. (C–E) Light inducible local membrane recruitment of ActA (C) Confocal images of ActA translocation. Yellow boxes indicate the area of blue light illumination. (D) Time course of membrane/lumen ratio of ActA-SspB variants (n≥5 for each variant). Error bars indicate SEM. Blue bar indicates the time window of blue light stimulation. (E) Average membrane/lumen ratio of mCherry signal. In each condition, left and right bars indicate before and after light stimulation, respectively. The numbers on the bar chart indicate the fold change after stimulation.

Figure S5

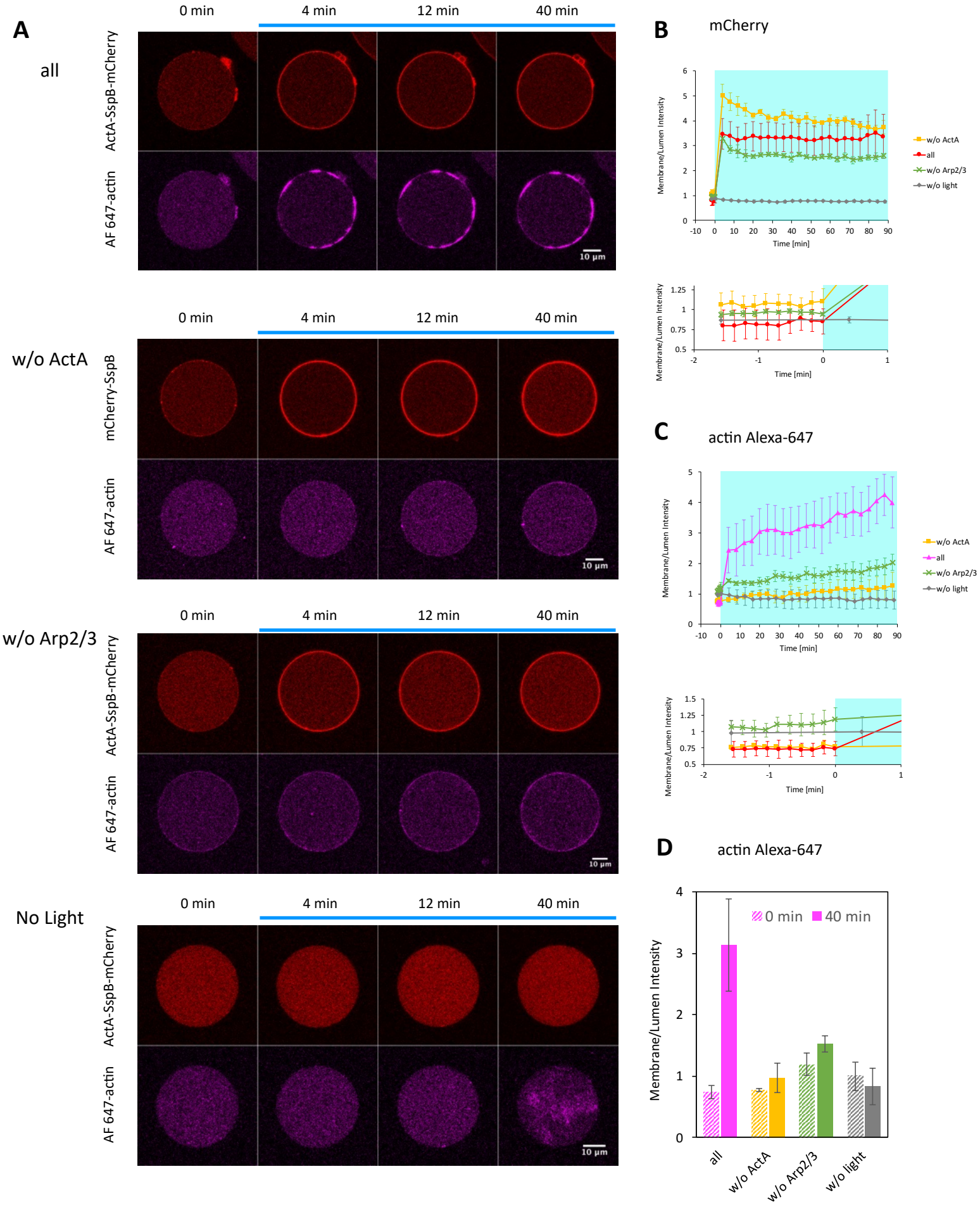
A
all
0 min
4 min
12 min
40 min
ActA-SspB-mCherry
AF 647-actin
10 µm
w/o ActA
mCherry-SspB
w/o Arp2/3
No Light
B
mCherry
Membrane/Lumen Intensity
Time [min]
w/o ActA
all
w/o Arp2/3
w/o light
C
actin Alexa-647
D
actin Alexa-647
0 min
40 min
all
w/o ActA
w/o Arp2/3
w/o light

Figure S5

Fig S5. Light inducible actin polymerization with global ActA membrane recruitment. iLID-EYFP-MARCKS (5 µM), ActA-SspBnano-mCherry (2 µM), actin (1.5 µM, 10% Alexa-647 labeled), and Arp2/3 (150 nM) were encapsulated in GUVs containing 60 mol% POPC/40 mol% POPS. Blue light was applied to the entire GUV. (A) Representative images of ActA(1–183)-SspB(nano)-mCherry and actin Alexa-647. All components (n=4): w/o ActA: ActA(1–183)-SspB(nano)-mCherry was replaced with mCherry-SspB(micro) (n=3), w/o Arp2/3: Arp2/3 was omitted (n=3). No Light: no blue light stimulation (n=3). (B, C) Time course of membrane/lumen ratio of mCherry and actin Alexa 647. (D) Bar chart of membrane/lumen ratio of actin Alexa 647 before (0 min) and after (40 min) light stimulation. Error bars indicate SEM.

Figure S6

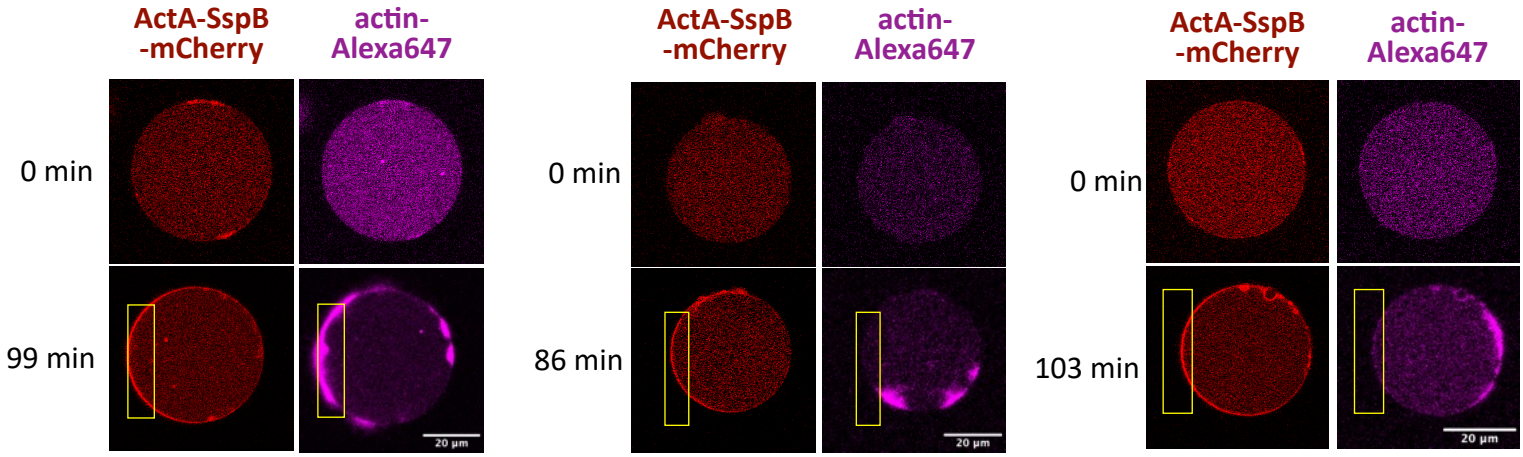

Fig S6. Asymmetric ActA membrane recruitment fails to induce directed actin polarization toward local light illumination. iLID-EYFP-MARCKS (5 µM), ActA-SspBnano-mCherry (2 µM), actin (1.5 µM, 10% Alexa-647 labeled), and Arp2/3 (150 nM), 1 mM ATP were encapsulated in GUVs containing 60 mol% POPC/40 mol% POPS. Yellow boxes indicate the area of blue light illumination. Although ActA creates asymmetric distribution, actin patches randomly distributed due to the diffusion on the membrane.

Figure S7

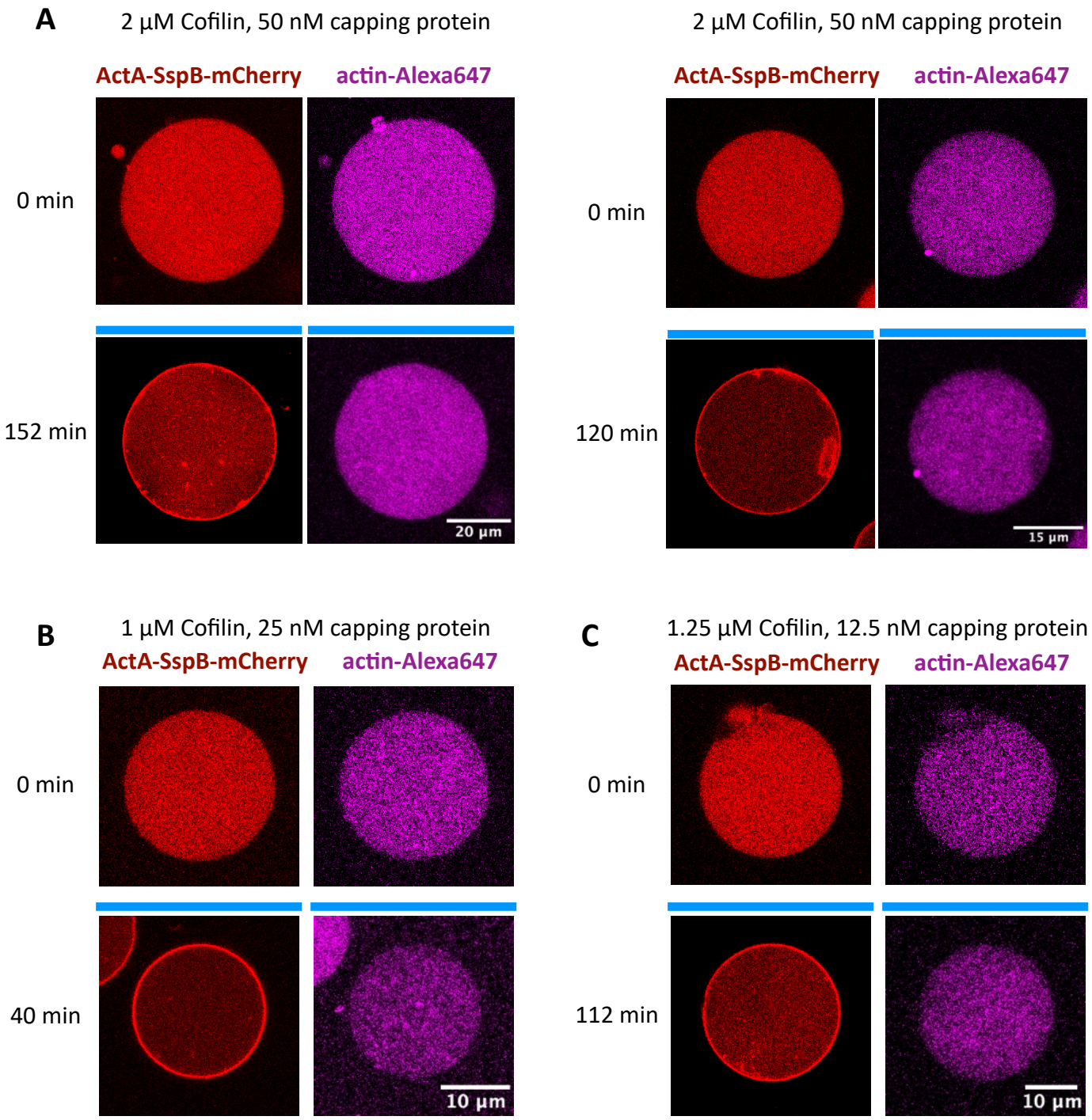

Fig. S7. Global ActA membrane recruitment fails to induce actin polymerization on the membrane in the presence of profilin, cofilin, and capping protein. 15 µM iLID-YFP-MARCKS, 5 µM ActA(1-183)-SspB(nano)-mCherry, 7.5 µM actin (10% Alexa 647 labeled), 150 nM Arp2/3, 3 µM profilin, cofilin, and capping protein were encapsulated in GUVs containing 60 mol% POPC/40 mol% POPS. Blue bars indicate the period of blue light illumination.

Figure S8

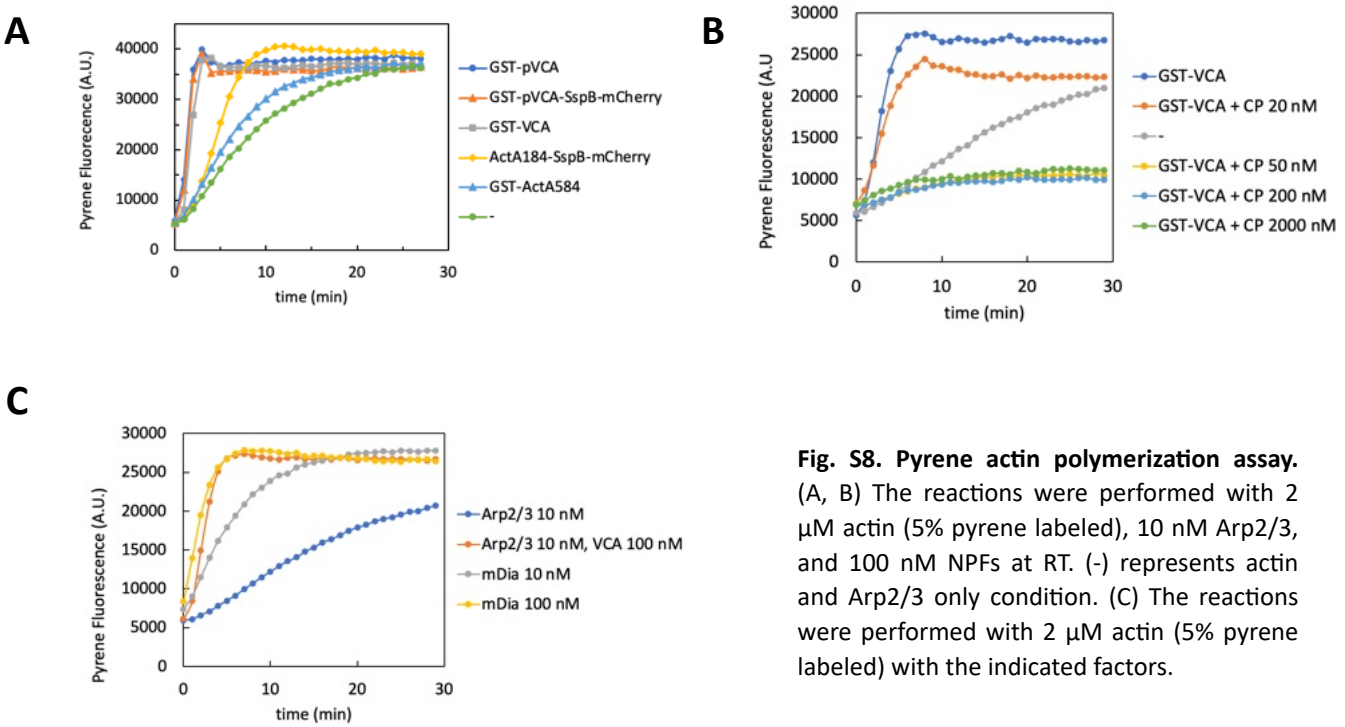

Fig. S8. Pyrene actin polymerization assay. (A, B) The reactions were performed with 2 µM actin (5% pyrene labeled), 10 nM Arp2/3, and 100 nM NPFs at RT. (-) represents actin and Arp2/3 only condition. (C) The reactions were performed with 2 µM actin (5% pyrene labeled) with the indicated factors.

Figure S9

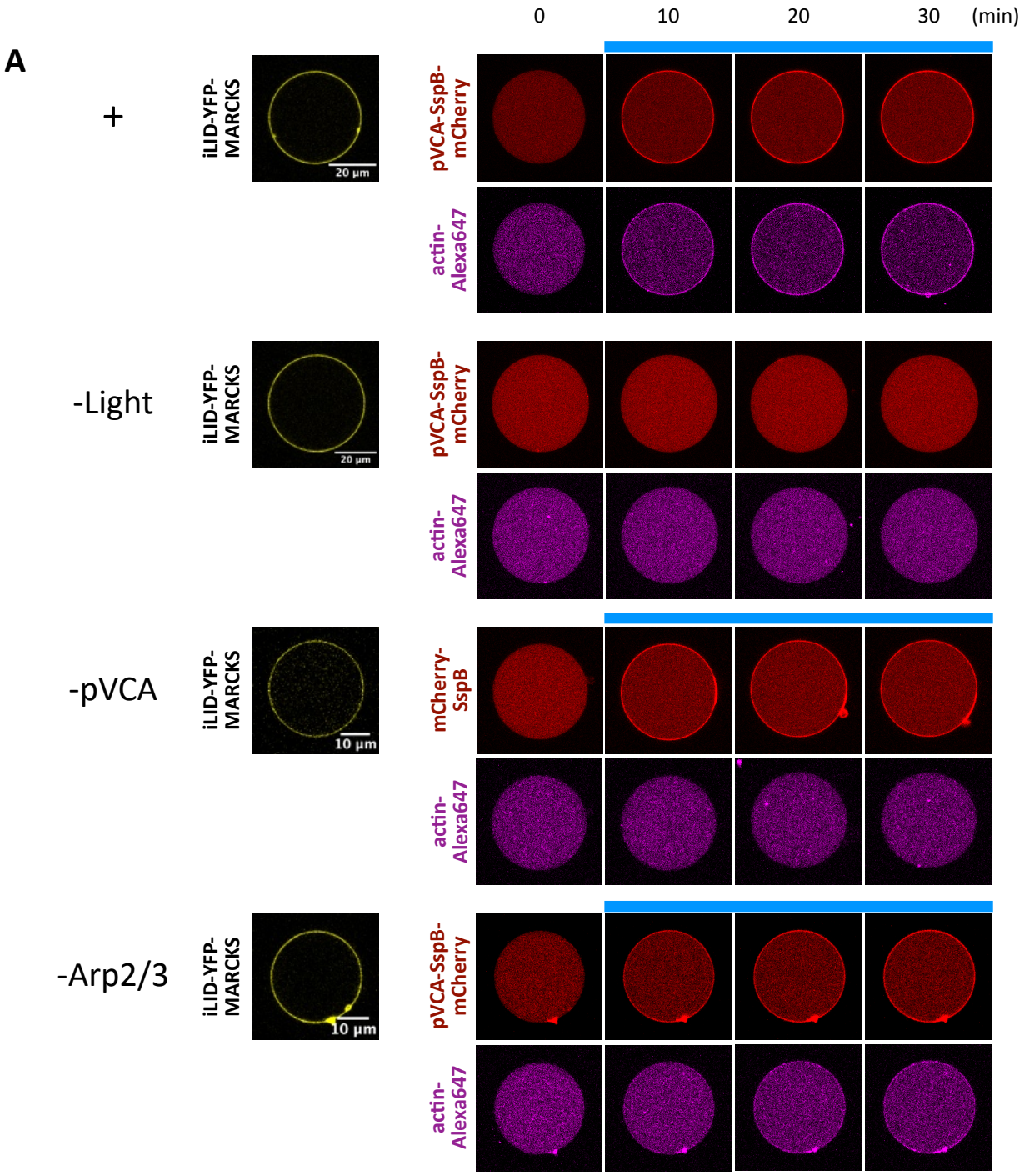

Fig. S9. Light control of actin cytoskeleton with pVCA-SspB-mCherry. The **d**ata correspond to Fig. 2C–E. (+) condition contains 15 µM iLID-YFP-MARCKS, 4.2 µM pVCA-SspB(nano)-mCherry, 7.5 µM actin (10% Alexa 647 labelled), 150 nM Arp2/3, 100 nM capping protein, 3 µM profilin, 4 µM cofilin, and 1 mM ATP. In (-light) and (-Arp2/3) conditions, blue light illumination or Arp2/3 was omitted from (+) condition, respectively. In (-pVCA) condition, pVCA-SspB(nano)-mCherry was replaced with mCherry-SspB(micro).

Figure S10

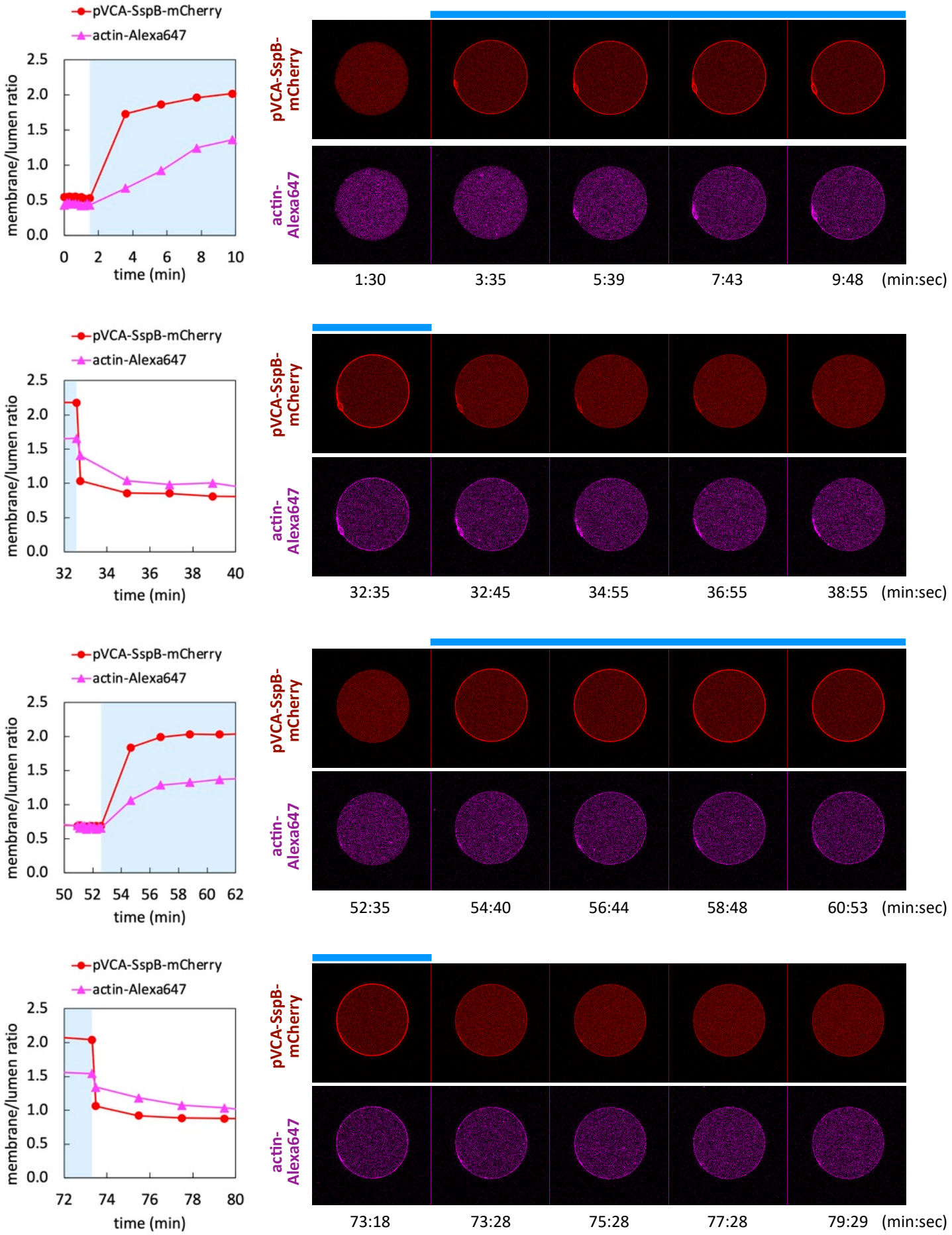
pVCA-SspB-mCherry
actin-Alexa647
membrane/lumen ratio
time (min)
pVCA-SspB-mCherry
actin-Alexa647
1:30
3:35
5:39
7:43
9:48
(min:sec)
32:35
32:45
34:55
36:55
38:55
52:35
54:40
56:44
58:48
60:53
73:18
73:28
75:28
77:28
79:29

Figure S10

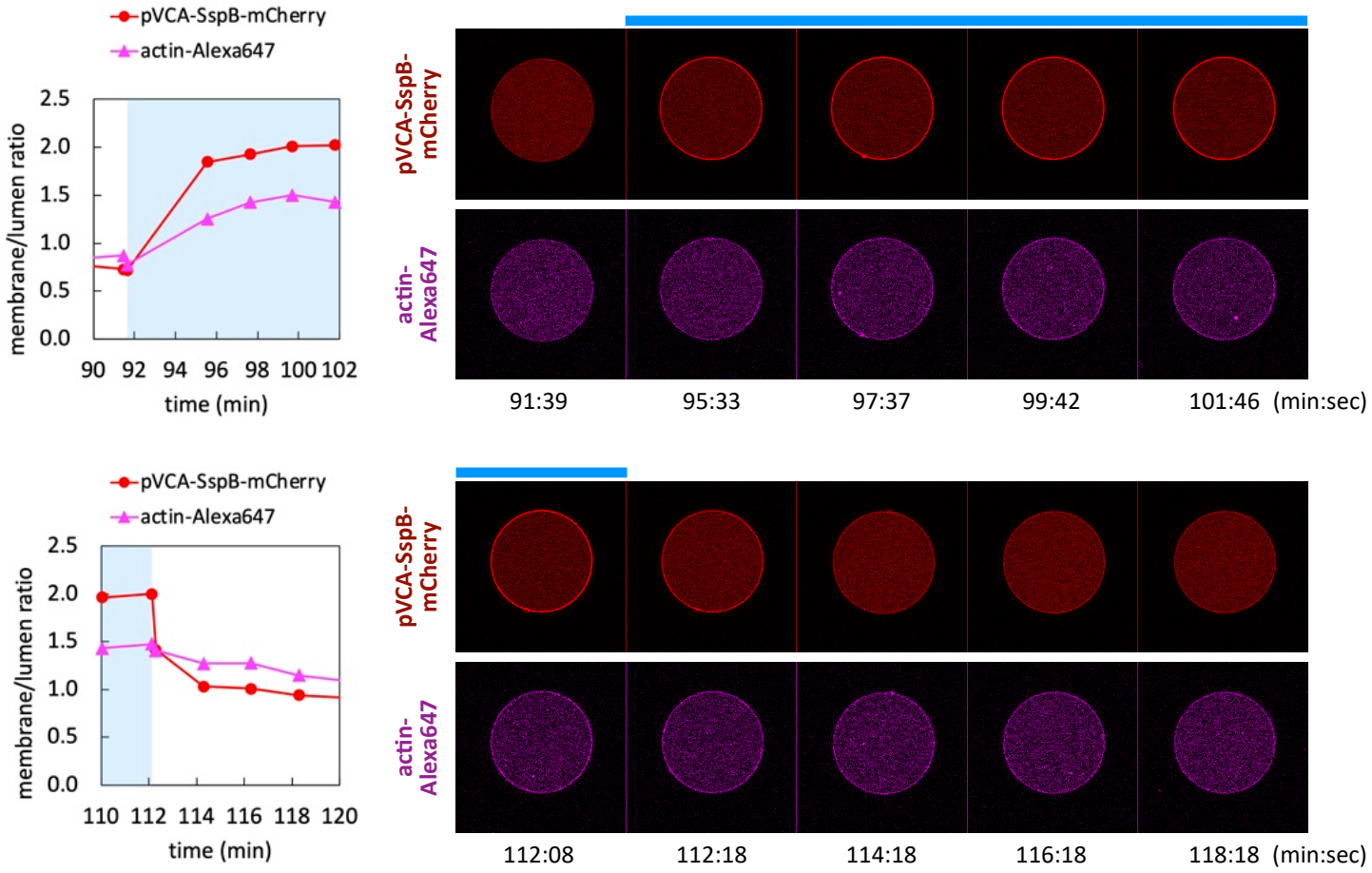

Fig. S10. Representative images of reversible actin polymerization. Confocal images and time course of membrane/lumen ratio of pVCA-SspB-mCherry and Alexa 647-labeld actin. Blue bars on images and blue regions in graphs indicate timepoints with blue light illumination. This figure corresponds with Fig. 2F, G.

Figure S11

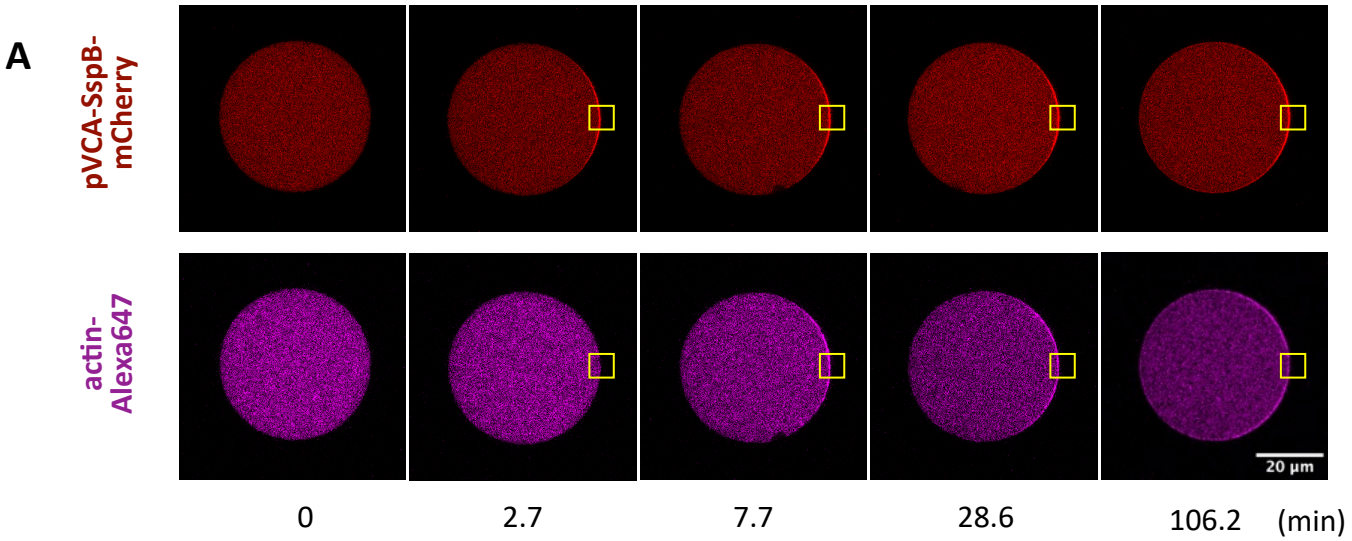

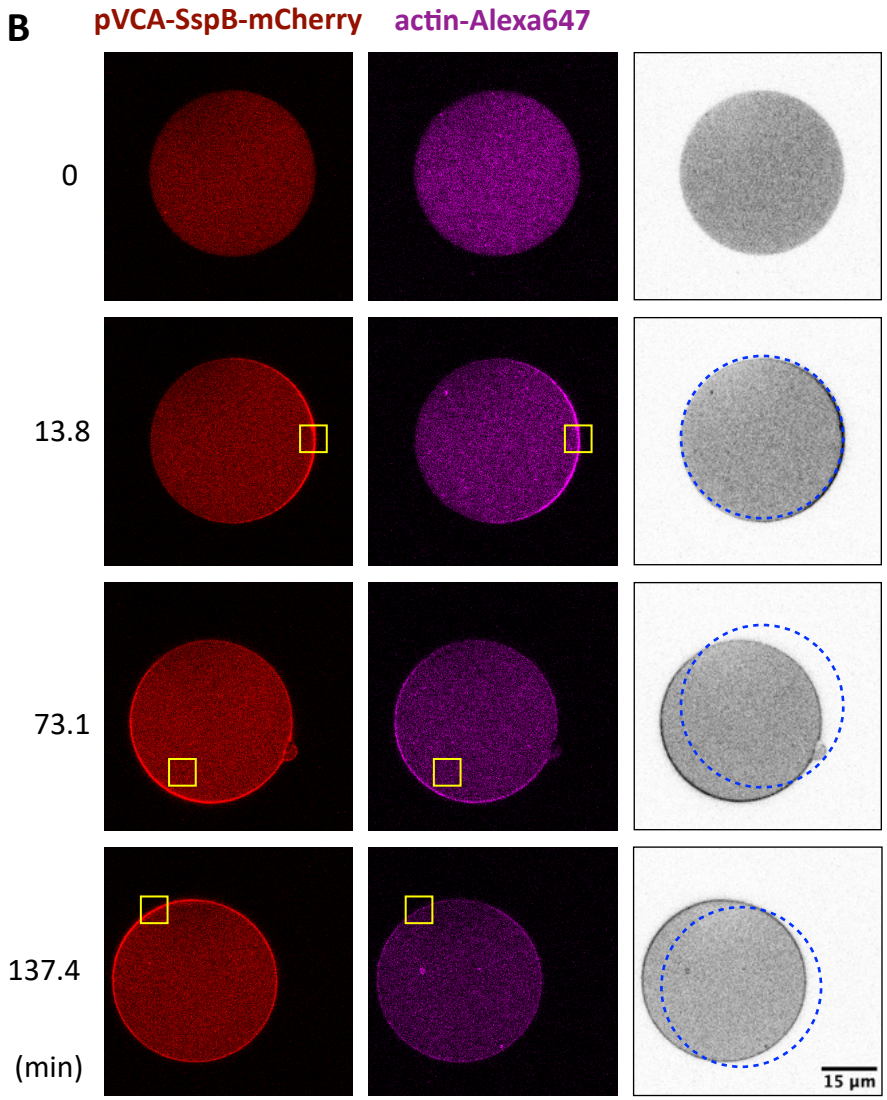

Fig. S11. Asymmetric actin polymerization induced by pVCA. (A, B) Confocal images of local pVCA recruitment and actin polymerization. Yellow boxes indicate areas of blue light illumination. (A) The data corresponds to Fig. 3B and C. In (B), Vesicle movement toward light stimulation was observed. Gray scaled images were created by averaging pVCA and actin images. Dotted circles indicate positions of vesicles in the images of one above.

Figure S12

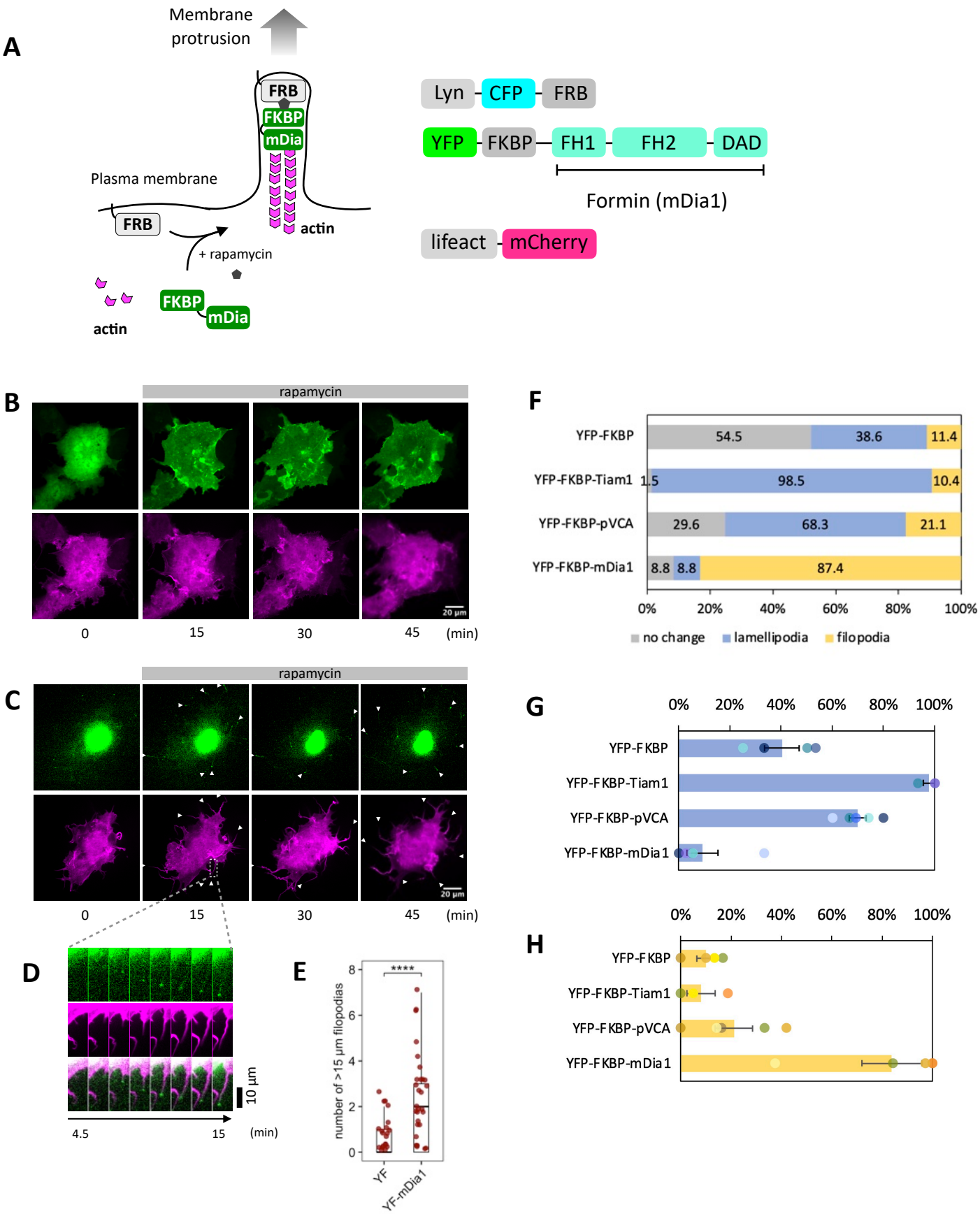
A
Membrane protrusion
FRB
FKBP
mDia
Plasma membrane
FRB
actin
+ rapamycin
FKBP
mDia
actin
Lyn
CFP
FRB
YFP
FKBP
FH1
FH2
DAD
Formin (mDia1)
lifeat
mCherry
B
rapamycin
20 µm
0
15
30
45
(min)
C
rapamycin
20 µm
0
15
30
45
(min)
D
10 µm
4.5
15
(min)
E
****
number of >15 µm filopodias
YF
YF-mDia1
F
YFP-FKBP
54.5
38.6
11.4
YFP-FKBP-Tiam1
1.5
98.5
10.4
YFP-FKBP-pVCA
29.6
68.3
21.1
YFP-FKBP-mDia1
8.8
8.8
87.4
0%
20%
40%
60%
80%
100%
no change
lamellipodia
filopodia
G
0%
20%
40%
60%
80%
100%
YFP-FKBP
YFP-FKBP-Tiam1
YFP-FKBP-pVCA
YFP-FKBP-mDia1
H
0%
20%
40%
60%
80%
100%
YFP-FKBP
YFP-FKBP-Tiam1
YFP-FKBP-pVCA
YFP-FKBP-mDia1

Figure S12

Fig. S12. Quantitative analysis of mDia1-induced filopodia formation in Cos7 cells. (A) Schematic representation of chemically-inducible mDia1 translocation and membrane protrusions. (B, C) Confocal images of plasma membrane recruitment of mDia1 and subsequent filopodia formation. Cos7 cells were transfected with Lyn-ECFP-FRB, Lifeact-mCherry, and either of YFP-FKBP or YFP-FKBP-mDia1. At time 0, 100 nM rapamycin was added. Green: YFP-FKBP or YFP-FKBP-mDia1. Magenta: Lifeact-mCherry. (B) YFP-FKBP control. (C) YFP-FKBP-mDia1. (D) Zoomed-up view of filopodia extension. Images were acquired every 1.5 minutes. The bottom is merged image. (E) Quantification of mDia1-induced filopodia. Number of filopodia whose length is longer than 15 µm was counted. P-values: ****: < 0.0001. Wilcoxon rank sum test. YF (YFP-FKBP): n=36 cells. YF-mDia1 (YFP-FKBP-mDia1): n=33 cells. (F–H) Quantification of the phenotypes observed after plasma membrane translocation of mDia1, pVCA, Tiam1 (Rac1 GEF), and control protein YFP-FKBP.

Figure S13

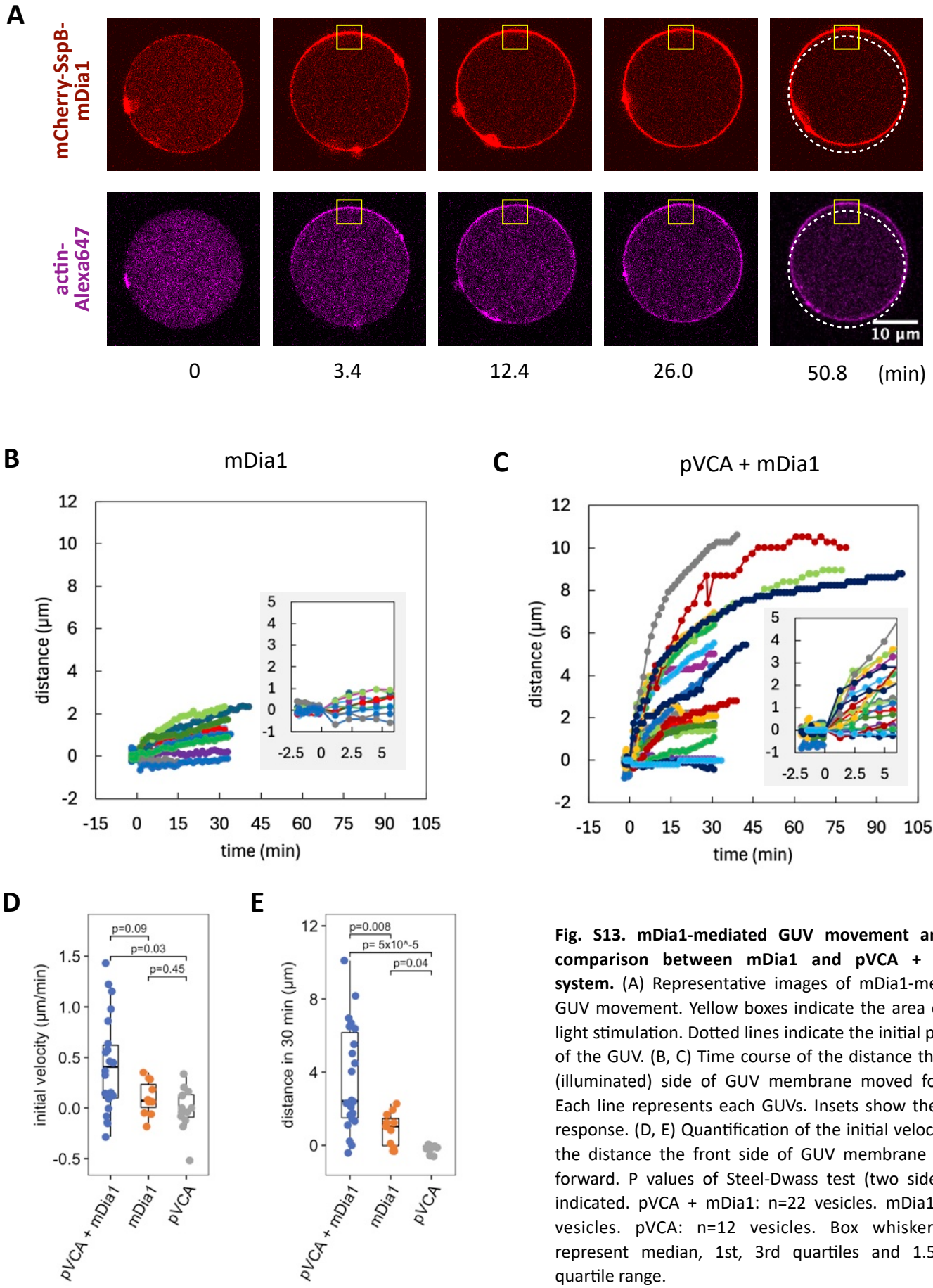

Fig. S13. mDia1-mediated GUV movement and the comparison between mDia1 and pVCA + mDia1 system. (A) Representative images of mDia1-mediated GUV movement. Yellow boxes indicate the area of blue light stimulation. Dotted lines indicate the initial position of the GUV. (B, C) Time course of the distance the front (illuminated) side of GUV membrane moved forward. Each line represents each GUVs. Insets show the initial response. (D, E) Quantification of the initial velocity and the distance the front side of GUV membrane moved forward. P values of Steel-Dwass test (two sided) are indicated. pVCA + mDia1: n=22 vesicles. mDia1: n=11 vesicles. pVCA: n=12 vesicles. Box whisker plots represent median, 1st, 3rd quartiles and 1.5×inter-quartile range.

Figure S14

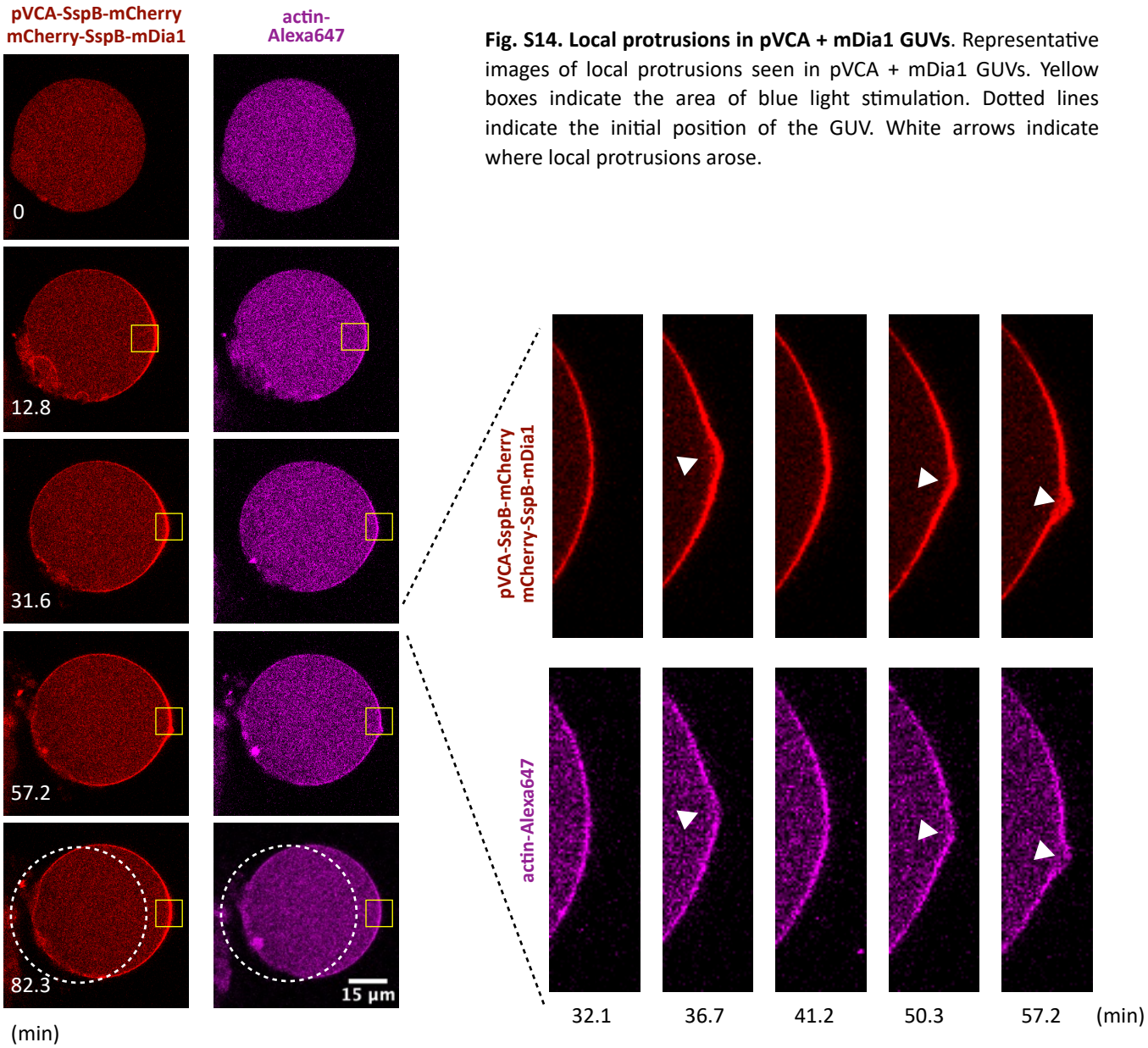

Fig. S14. Local protrusions in pVCA + mDia1 GUVs. Representative images of local protrusions seen in pVCA + mDia1 GUVs. Yellow boxes indicate the area of blue light stimulation. Dotted lines indicate the initial position of the GUV. White arrows indicate where local protrusions arose.

Figure S15

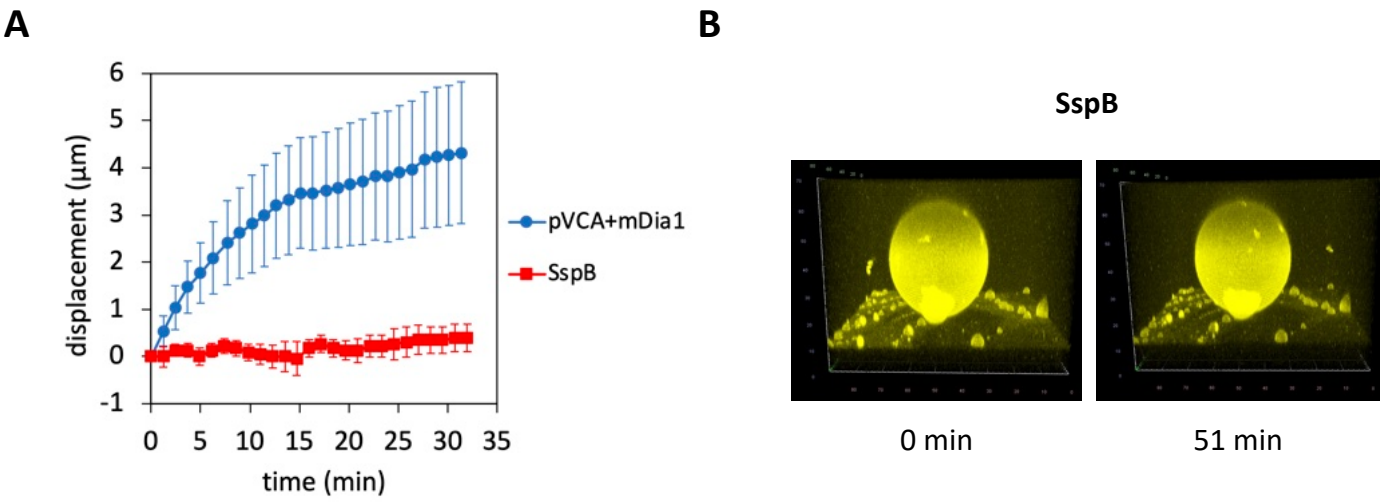

Fig. S15. Lack of vesicle movement and shape change with mCherry-SspB. With pVCA-SspB-mCherry and mCherry-SspB-mDia1 being replaced with mCherry-SspB, GUVs neither moved nor changed their shape after blue light illumination. (A) Time course of the distance the front (illuminated) side of GUV membrane moved forward. pVCA + mDia1 GUVs: n=6 vesicle. SspB GUVs: n=4 vesicles. Error bars indicate SEM. (B) 3D reconstitution of iLID-YFP-SNAP images before and after blue light illumination.

Figure S16

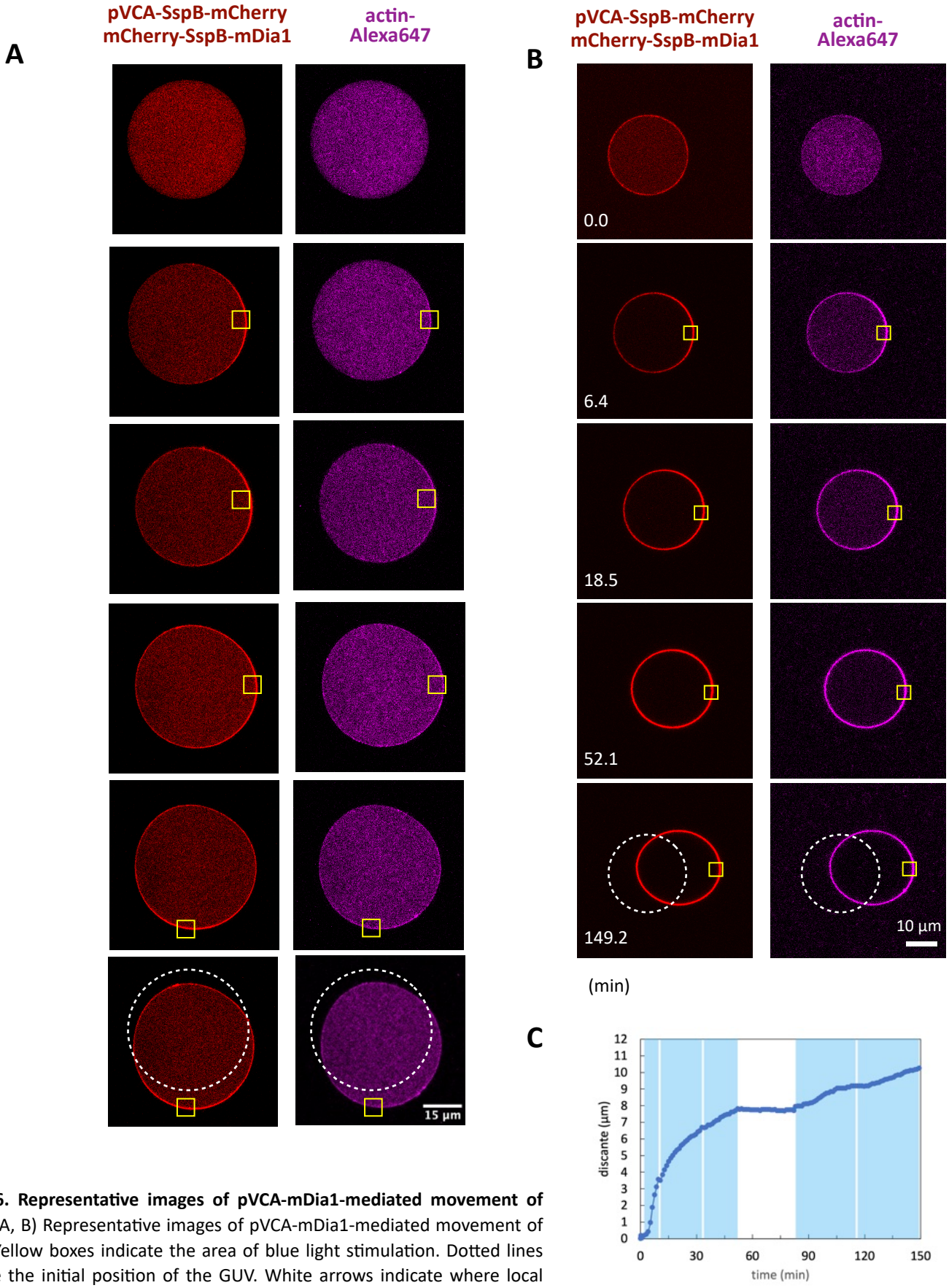

Fig. S16. Representative images of pVCA-mDia1-mediated movement of GUVs. (A, B) Representative images of pVCA-mDia1-mediated movement of GUVs. Yellow boxes indicate the area of blue light stimulation. Dotted lines indicate the initial position of the GUV. White arrows indicate where local protrusions arose. (C) Distance the front side of GUV membrane moved forward. Data was quantified from the images of (B). Blue areas indicate the periods of blue light stimulation.